THE FLORIDA STATE UNIVERSITY

COLLEGE OF ARTS AND SCIENCES

MEASUREMENT OF THE MUON CHARGE ASYMMETRY IN $P\overline{P} \rightarrow W + X \rightarrow \mu\nu + X$ EVENTS USING THE DØ DETECTOR

By

TRANG THI KIEU HOANG

A Dissertation submitted to the
Department of Physics
in partial fulfillment of the
requirements for the degree of
Doctor of Philosophy

Degree Awarded:
Fall Semester, 2012

Trang Thi Kieu Hoang defended this dissertation on October 31, 2012.

The members of the supervisory committee were:

Susan K. Blessing
Professor Directing Dissertation

Ettore Aldrovandi
University Representative

Andrew Askew
Committee Member

Joseph Owens III
Committee Member

Jorge Piekarewicz
Committee Member

The Graduate School has verified and approved the above-named committee members, and certifies that the dissertation has been approved in accordance with the university requirements.

ACKNOWLEDGMENTS

This dissertation was done with endless help and support from many people. First, I would like to thank my advisor Susan Blessing for her patient guidance, understanding, and enthusiastic encouragement. I deeply appreciate her taking time to edit my writings. I also want to thank Andrew Askew for his contribution to this analysis and for providing many fruitful discussions and advice. I also thank my committee members for giving valuable critique and helping to improve the manuscript.

I wish to thank all the High Energy Group members at Florida State University, Todd Adams, Horst Wahl, Harrison Prosper, Vasken Hagopian, Sharon Hagopian, Laura Reina, and Joseph Owens for their interesting talks, lectures, and advice.

I would like to thank all DØ Collaboration members for taking data and developing the sophisticated software used in this analysis. I thank people in the electroweak physics group, especially Heidi, Junjie, Rafael, Alex, Jadranka, Hang, and Breese for their valuable help. My grateful thanks are also extended to people in the calorimeter group, especially Dean and Walter for their patient explanations and interesting discussions.

My time at Fermilab would be difficult without support from many fellows and friends. I thank Dan, Edgar, Haryo, Trung, Duong, Huong, Weigang, Ruchika, and Abhinav for their willingness to lend a hand whenever I needed help.

I would like to thank my classmates at Florida State, Hanna, Naureen, Mukesh, and Ben who went with me through a long journey to pursue my career. I also need to thank the Physics graduate office staff, Sherry, Melissa, Nellie, and Kathy, for their generous assistance.

Most of all, I thank my parents, my sisters, and my brothers for their love and support, especially during difficult and stressful times.

TABLE OF CONTENTS

LIST OF TABLES

LIST OF FIGURES

LIST OF ABBREVIATIONS

AA	Alternative Algorithm
ATLAS	A Toroidal LHC Apparatus
CDF	Collider Detector at Fermilab
CC	central calorimeter
CERN	European laboratory for particle physics
CFT	central fiber tracker
CKM	Cabibbo-Kobayashi-Maskawa
CMS	Compact Muon Solenoid
dca	distance of closest approach
DGLAP	Dokshitzer-Gribov-Lipatov-Altarelli-Parisi
DIS	deep-inelastic scattering
EC	end calorimeter
EM	electromagnetic
EW	electroweak
GEANT	detector description and simulation tool
HERA	Hadron Elektron Ring Anlage
HTF	Histogram Track Finder
ICD	inner cryostat detector
L1Cal	level 1 calorimeter trigger
L1CTT	level 1 central track trigger
L1Muon	level 1 muon trigger
LHC	large hadron collider
LM	luminosity monitor
MC	Monte Carlo
MDT	mini drift tube
MSTW	Martin-Stirling-Thorne-Watt
NLO	next-to-leading order
NNLO	next-to-next-to-leading order
PDF	parton distribution function
PDT	proportional drift tube
PMT	photo multiplier tube
PV	primary vertex
QCD	quantum chromodynamics
SLAC	SLAC National Laboratory
SMT	silicon microstrip tracker
VLPC	visible light photon counter

ABSTRACT

This dissertation describes a measurement of the muon charge asymmetry from $W \to \mu\nu$ decay using 7.3 fb^{-1} of data collected from April 2002 to July 2010 using the DØ detector at Fermi National Accelerator Laboratory. The measurement for muons with pseudorapidity $|\eta| < 2$ probes the charge asymmetry for momentum fraction x from 0.005 to 0.3. The charge asymmetry is compared with the theory predictions generated from RESBOS with CTEQ6.6 parton distribution functions and from POWHEG with CT10 and MSTW2008 PDFs. The results show good agreement with the electron charge asymmetry measurement from DØ. So far, our measurement is the most precise lepton charge asymmetry measurement done at the Tevatron.

CHAPTER 1

INTRODUCTION

For over two decades, the Tevatron Collider played an important role in the amazing race of physicists and researchers to answer the most fundamental questions about the Universe: what the ultimate particles of matter are and how they interact with each other. During its 26-year lifetime, experimenters at the Tevatron achieved many remarkable discoveries, including finding the top quark in 1995 [1, 2], the B_c meson in 1998 [3], the tau neutrino in 2000 [4], and single top quark production in 2009 [5]. Many notable experimental measurements done at the facility have supported the standard model, a theory that describes the material of the Universe as made up of elementary spin-1/2 particles interacting through fields.

This dissertation describes a precision measurement of the charge asymmetry of muons from W boson decays. This measurement provides information to constrain the parton distribution functions (PDFs) of the quarks inside protons. In turn, the PDFs are very important inputs for measuring other standard model processes and for searching for new physics at hadron colliders. Many experiments at the Tevatron and the Large Hardon Collider rely on the precision of the PDFs. For example, the PDFs can influence cross section measurements via Monte Carlo estimates of signals and backgrounds. As another example, the precision of the W boson mass measurement depends on the Monte Carlo prediction of the W boson production which is sensitive to the uncertainty of the PDFs [6]. In turn, knowledge of the W boson and Z boson masses is very important for Higgs boson physics.

The organization of the dissertation is as follow. Chapter 1 presents brief descriptions of the standard model, parton distribution functions, W boson production, and the muon

charge asymmetry. Chapter 2 describes the Tevatron apparatus and the relevant components of the DØ detector. Event reconstruction is presented in Chapter 3. Details of the experimental techniques are described in Chapter 4, followed by the results and conclusions in Chapter 5.

1.1 The standard model of particle physics

The standard model was developed beginning in the middle of the 20th century and finalized in the 1970s. According to this model, matter is made up of six quarks (u, d, c, s, t, b) and six leptons (e, ν_e, μ, ν_μ, τ, ν_τ). They are spin-1/2 particles, called fermions. The quarks carry fractional electric charges, $+2/3$ or $-1/3$ of the proton charge, while the leptons carry integral electric charges, -1, $+1$, or 0. Each fermion has an associated antiparticle with the same mass and spin but opposite sign in the electric charge and other charges (see Table 1.1).

Table 1.1: Spin 1/2 fermions

Generation I	Generation II	Generation III	Electric charge	Baryon number	Lepton number
Quarks and antiquarks					
u (up)	c (charm)	t (top)	$+2/3$	$+1/3$	0
d (down)	s (strange)	b (bottom)	$-1/3$	$+1/3$	0
$\overline{u}$	$\overline{c}$	$\overline{t}$	$-2/3$	$-1/3$	0
$\overline{d}$	$\overline{s}$	$\overline{b}$	$+1/3$	$-1/3$	0
Leptons and antileptons					
e^- (electron)	μ^- (muon)	τ^- (tau)	-1	0	1
e^+ (positron)	μ^+	τ^+	1	0	-1
ν_e (neutrino)	ν_μ	ν_τ	0	0	1
$\overline{\nu}_e$	$\overline{\nu}_\mu$	$\overline{\nu}_\tau$	0	0	-1

The fermions are grouped in three generations. The first generation has the smallest masses. As the generation number increases, the heavier the particles are. The second and third generation particles have very short lifetimes and are only observed in very high energy environments.

Unlike the leptons, the quarks cannot exist as free particles. They are only found in color-neutral composite particles, called hadrons, such as uud in a proton. The quarks which

determine the quantum properties of the hadrons are called valence quarks. In addition, the hadrons contain virtual (or sea) quarks, antiquarks, and gluons. The virtual particles do not influence the quantum numbers of the hadrons.

The fermions interact by exchanging force mediators with spin 1, called gauge bosons. There are four types of fundamental interaction: strong, electromagnetic, weak, and gravitational interactions (see Table 1.2). The strong interaction binds the quarks in nucleons (neutrons and protons), and nucleons in nuclei. The strong interaction is mediated by massless bosons called gluons. The electromagnetic interaction is responsible for the interaction between electrically charged particles with photons as the electromagnetic force carriers.

The weak interaction, mediated by the exchange of $W^{\pm}$ and Z bosons, acts between quarks and leptons. The weak interactions involving the $W^{\pm}$ bosons happen between left-handed particles and right-handed antiparticles only. The $W^{\pm}$ bosons carry electric charge, therefore they also couple to the electromagnetic interaction.

The gravitational interaction is a long range force and acts between all particles with mass. It is the weakest interaction on the scale of particle physics experiments and supposed to be mediated by a spin 2 gauge boson, called the graviton. The gravitational interaction is not included in the standard model. Building an integrated theory of everything that unites of all these forces and associated theories is a major goal of physics.

Table 1.2: Interaction mediators [7]

Force	Relative strength	Mediator
Strong	1	g (gluon)
Electromagnetic	10^{-2}	γ (photon)
Weak	10^{-7}	$W^{\pm}$, Z^0
Gravity	10^{-39}	G (graviton)

1.2 Parton distribution functions

In $p\overline{p}$ collisions, interactions actually happen between the partons (quarks and gluons) inside the protons and antiprotons. For example, the W boson is produced by the collision of a quark a inside the proton and a quark b inside the antiproton (see Figure 1.1). According

to the parton model, the cross section for W boson production is

$$\sigma(p+\overline{p}\rightarrow W+X)=\sum_{a,b}\int_0^1 dx_a\int_0^1 dx_b a_p(x_a,Q^2)b_{\overline{p}}(x_b,Q^2)\hat{\sigma}_{a+b\rightarrow W+X}(x_a,x_b,Q^2) \quad (1.1)$$

where x_a is the proton momentum fraction carried by the quark a, x_b is the antiproton momentum fraction carried by the quark b, and Q is the momentum transfer in the collision. $a_p(x_a,Q^2)$ $\left(b_{\overline{p}}(x_b,Q^2)\right)$, called parton distribution functions, are the probabilities to find the parton a (b) inside the proton (antiproton). $\hat{\sigma}_{a+b\rightarrow W+X}$ is the partonic cross section of W boson production from the collision of the quarks a and b, and X is the accompanying final state.

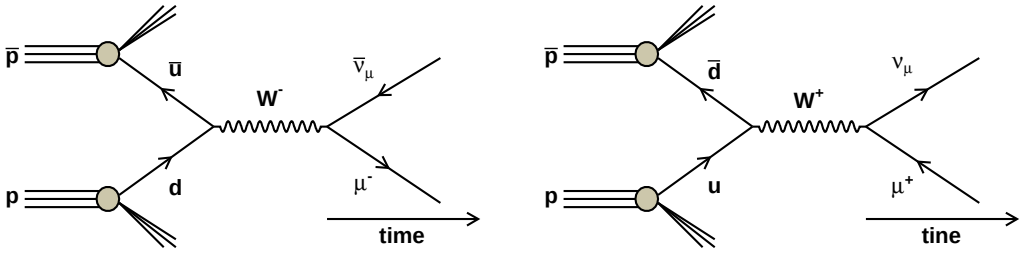

Figure 1.1: The dominant processes for $W^{\pm}$ boson production at the Tevatron.

There are two valence u quarks and one valence d quark in the proton. Therefore, the total number of the valence quarks in a proton can be determined using the following sum rule:

$$\int_0^1 [u_v(x)+d_v(x)]dx=3 \quad (1.2)$$

where $u_v(x)=[u(x)-\overline{u}(x)]$ and $d_v(x)=[d(x)-\overline{d}(x)]$ are the numbers of valence u and d quarks. Figure 1.2 shows the parton distributions from HERAPDF1.5 in next-to-next-to-leading order (NNLO) at $Q^2=10000$ GeV^2 [8]. This is the Q^2 region relevant for the Tevatron and the Large Hardon Collider (LHC).

The parton content of the proton is not predicted in QCD, so it must be probed experimentally. Knowledge of the PDFs in the proton primarily comes from deep-inelastic scattering (DIS), W boson production, and inclusive single jet production. The DIS experiments measure functions of x and Q^2 describing the structure of hadrons (structure functions). The experiments involving W boson production probe the ratio $d(x)/u(x)$. And the jet data contributes to the gluon PDFs at high x range.

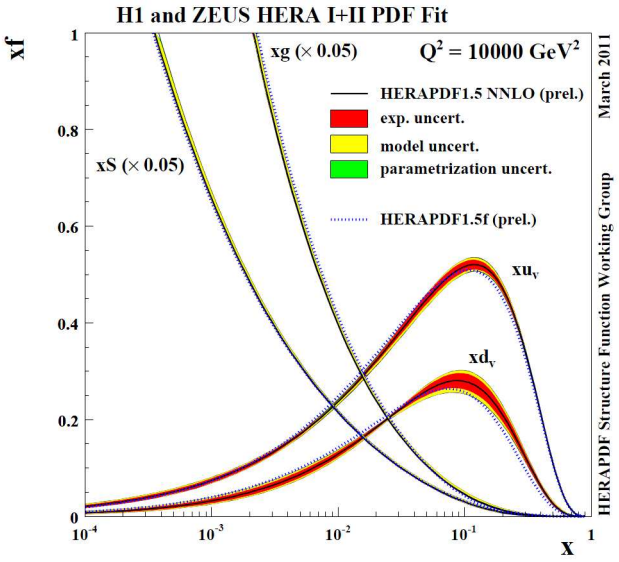

Figure 1.2: The parton distribution functions from HERAPDF1.5 NNLO $Q^2 = 10000$ GeV^2. The gluon and sea distributions are scaled down by a factor of 20. xf is the probability density of the momentum fraction x [8].

The experiments giving information contributing to the PDFs' determination do not directly measure the parton distributions. The general procedure to determine PDFs starts from a parameterization of the non-perturbative PDFs at a low scale. Then fits to various sets of experimental data (mainly to DIS data) are performed within the DGLAP (Dokshitzer-Gribov-Lipatov-Altarelli-Parisi) evolution scheme [9].

The experimental data mainly come from the H1 and ZEUS experiments at the electron-proton collider HERA, the DØ and CDF experiments at the Tevatron, and the ATLAS and CMS experiments at the LHC. The determination of PDFs is done by several groups including MSTW [10], CTEQ [11], NNPDF [12], HERAPDF [13], AB(K)M [14], and GJR [15]. Figure 1.3 shows the Q^2 and x ranges from several experiments [16].

1.3 W boson production and decay

1.3.1 $W^{\pm}$ production cross sections

At the Tevatron, $W^+(W^-)$ bosons are primarily produced by interactions between valence u (d) quarks in the proton and valence $\overline{d}$ ($\overline{u}$) antiquarks in the antiproton. The

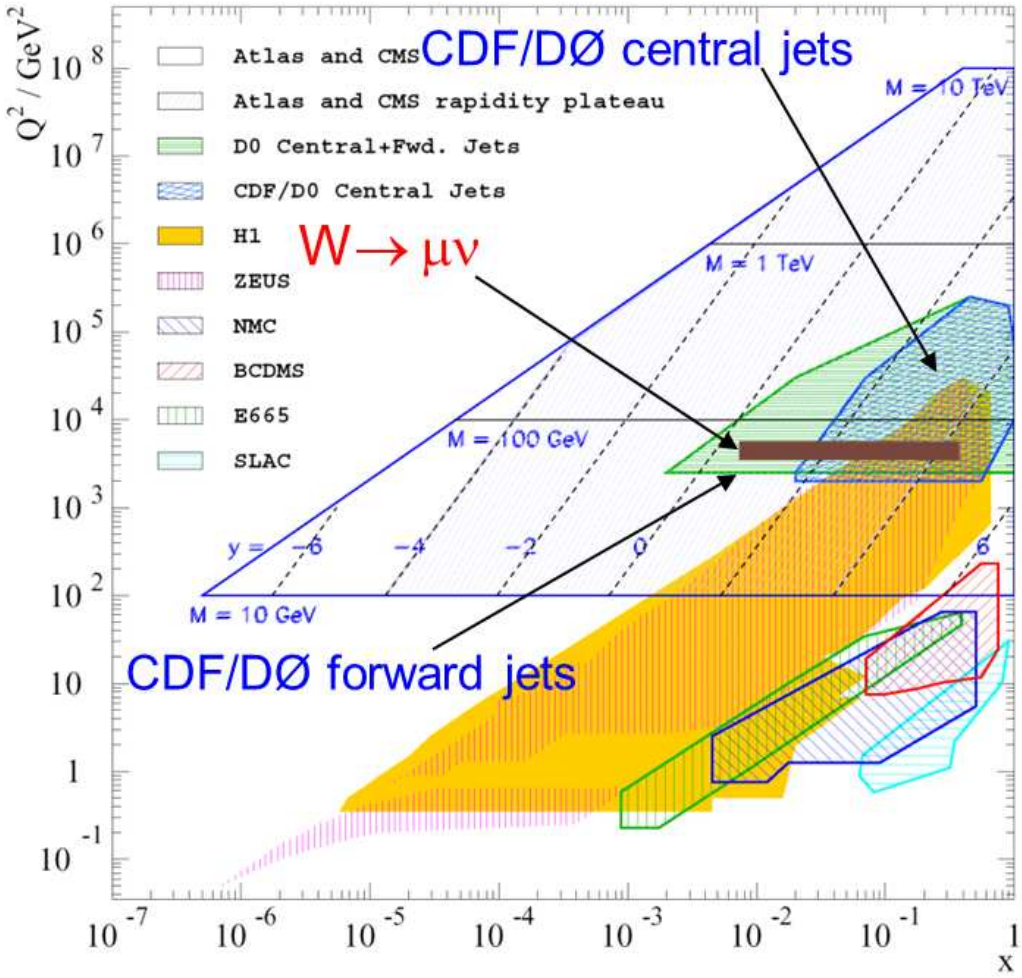

Figure 1.3: Range of x and Q^2 probed by various experiments. ATLAS and CMS are detectors at the LHC. DØ and CDF are at the Tevatron. H1 and ZEUS were at the HERA. NMC and BCDMS were muon scattering experiments at CERN. E665 was a muon-proton collider experiment at Fermilab. SLAC is the linear accelerator at Stanford, California. The $W \to \mu\nu$ process is from the analysis described in this dissertation [16].

contribution from sea quarks is small.

In the limit of a very narrow width, the partonic cross section for W^+ boson production can be written as [17]

$$\hat{\sigma}(a+b \to W^+) = 2\pi |V_{ab}|^2 \frac{G_F}{\sqrt{2}} M_W^2 \delta(\hat{s} - M_W^2) \tag{1.3}$$

where a denotes the quark in the proton, b denotes the antiquark in the antiproton, V_{ab} is the CKM matrix element, G_F is the Fermi coupling constant, $\hat{s}$ is the quark-antiquark center of mass energy, and M_W is the W boson mass.

In the center of mass frame of the proton and the antiproton, the W boson rapidity is defined as $y = \frac{1}{2}\ln[(E-p_z)/(E+p_z)]$, where E and p_z are the energy and the momentum in the z direction of the W boson. The z direction is chosen to be the direction of the proton momentum. The momentum fraction of a (b) in the proton (antiproton) can be calculated as

$$x_{a,b} = \frac{M_W}{\sqrt{s}} e^{\pm y} \tag{1.4}$$

Assuming that $Q^2 = \hat{s} = M_W^2$, the W^+ total cross section becomes

$$\sigma(p+\overline{p} \to W^+) = \frac{K}{3} \int_0^1 dx_a \int_0^1 dx_b \sum_{a,b} a(x_a, M_W^2) b(x_b, M_W^2) \hat{\sigma}_{a+b\to W^+}(x_a, x_b, M_W^2) \tag{1.5}$$

where $K = 1$ in the leading order, and $K \simeq 1 + \frac{8\pi}{9}\alpha_s(M_W^2)$ in the first order QCD correction.

Transforming the integration to the $\hat{s}$ and y variables using the relation $dx_a dx_b = \frac{d\hat{s}dy}{s}$, and integrating over $d\hat{s}$, we find

$$\frac{d\sigma}{dy}(W^+) = K \frac{2\pi G_F}{3\sqrt{2}} \sum_{a,b} |V_{ab}|^2 x_a x_b a(x_a, M_W^2) b(x_b, M_W^2) \tag{1.6}$$

From the fact that W boson production involves the valence quarks in the $p\overline{p}$ collision, and assuming that $u(x) = \overline{u}_{\overline{p}}(x)$ etc., the W^+ differential cross section roughly becomes

$$\frac{d\sigma}{dy}(W^+) \approx K \frac{2\pi G_F}{3\sqrt{2}} x_a x_b u(x_a) d(x_b) \tag{1.7}$$

Here $u(x_a)$ denotes the parton distribution function of the u quark, and $d(x_b)$ denotes the parton distribution function of the d quark.

Similarly, the differential cross section for W^- production can be obtained by interchanging x_a with x_b in Eq. 1.7

$$\frac{d\sigma}{dy}(W^-) \approx K\frac{2\pi G_F}{3\sqrt{2}}x_a x_b d(x_a)u(x_b) \tag{1.8}$$

d quarks are slightly more massive than u quarks [18]. On average, u quarks carry more of the proton's momentum than d quarks do (see Fig 1.2). Therefore, W^+ bosons tend to be produced with momentum along the direction of the proton. Likewise, W^- bosons tend to be produced with momentum along the direction of the antiproton. The W boson production asymmetry is defined as

$$A_W(y) = \frac{d\sigma(W^+)/dy - d\sigma(W^-)/dy}{d\sigma(W^+)/dy + d\sigma(W^-)/dy} \tag{1.9}$$

From Eqs. 1.7 and 1.8, we have

$$A_W(y) \approx \frac{u(x_a)d(x_b) - d(x_a)u(x_b)}{u(x_a)d(x_b) + d(x_a)u(x_b)} \tag{1.10}$$

$$= \frac{d(x_b)/u(x_b) - d(x_a)/u(x_a)}{d(x_b)/u(x_b) + d(x_a)/u(x_a)} \tag{1.11}$$

This equation shows that the W production asymmetry is strongly sensitive to the ratio of $d(x)/u(x)$. Figure 1.4 shows the $d(x)/u(x)$ ratios at $Q^2 = 10$ GeV^2 for various choices of nuclear corrections in the global fits for PDFs [20]. The $d(x)/u(x)$ results for $x > 0.8$ are extrapolations of the fitted PDFs.

1.3.2 Muon charge asymmetry

The W rapidity cannot be measured directly because the neutrino from the leptonic decay $W \to \ell\nu_\ell$ passes through detector materials without interacting. Instead, we measure the closely-related lepton charge asymmetry. In this dissertation, we consider the process $W \to \mu\nu$ and the muon charge asymmetry.

Due to the $V - A$ structure of the weak charged current, the muon is produced with its momentum direction constrained by the helicities of the particles involved. The helicity of a particle is the projection of the particle's spin vector $\mathbf{s}$ in the direction of its momentum vector $\mathbf{p}$, $H = \frac{\mathbf{s}\cdot\mathbf{p}}{|\mathbf{s}\cdot\mathbf{p}|}$. $H = 1$ if the spin vector points in the same direction as the momentum vector (right-handed), and $H = -1$ if they point in opposite directions (left-handed). In

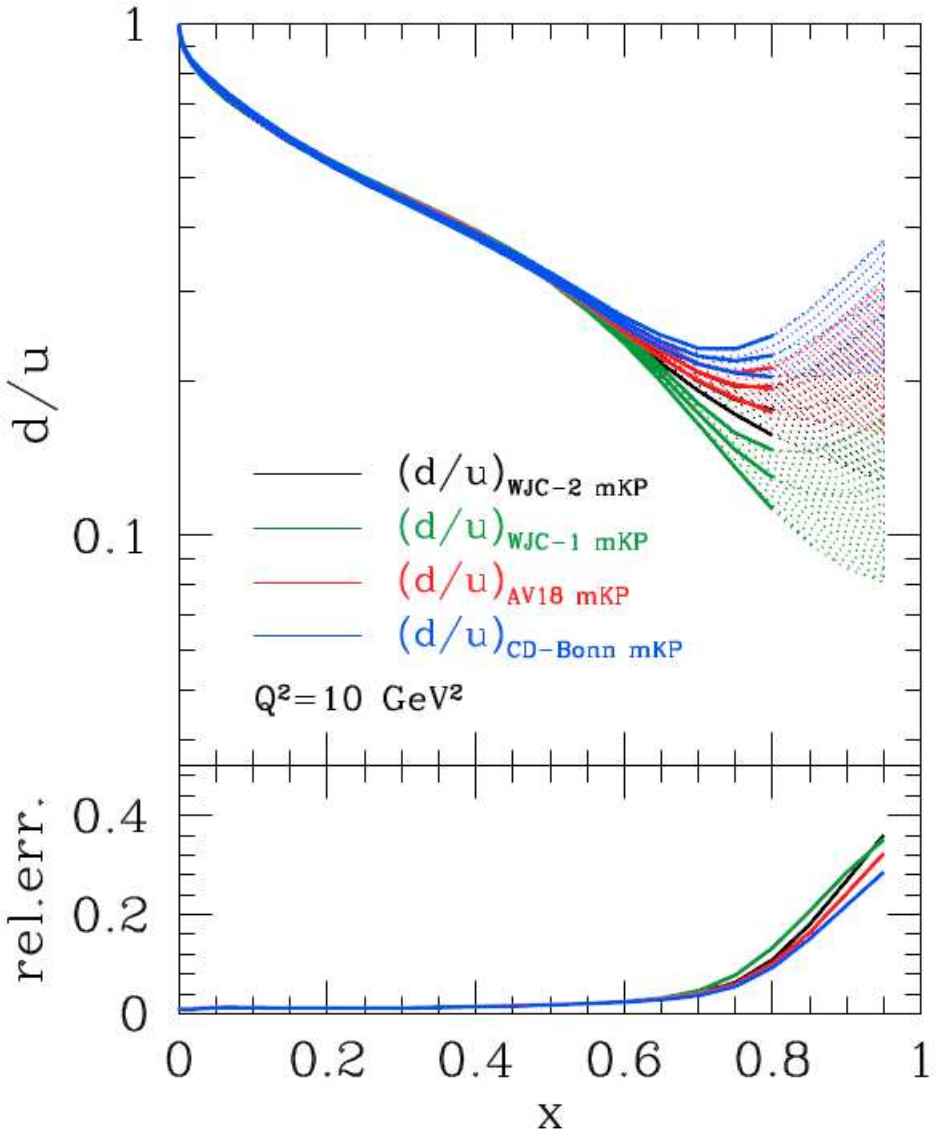

Figure 1.4: The $d(x)/u(x)$ ratio at $Q^2 = 10$ GeV^2 [20].

standard model, the W boson exclusively couples to left-handed fermions and right-handed antifermions. In W^+ boson production, the incoming u quark is left-handed and the $\overline{d}$ quark is right-handed. Angular momentum conservation requires that the right-handed μ^+ from W^+ boson decay preferentially moves along the direction of the incoming antiproton (see Figure 1.5). Likewise, the left-handed μ^- from a W^- boson preferentially moves along the direction of the proton. This is the opposite phenomenon to the W boson production asymmetry.

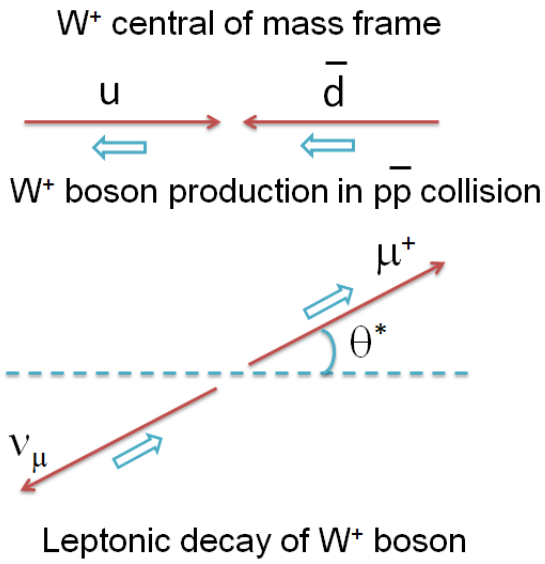

Figure 1.5: The momentum (solid arrows) and spin (open arrows) of particles in W^+ boson production and leptonic decay.

Therefore, in the $p+\overline{p} \to W \to \mu\nu$ process, the muon charge asymmetry is a convolution of the W boson production asymmetry with the asymmetry from the $V-A$ coupling. The rapidities of the W boson and the muon are related by [19]

$$y_\mu = y_W + \frac{1}{2}\ln\frac{1+\cos\theta^*}{1-\cos\theta^*} \tag{1.12}$$

where θ^* is the muon scattering angle with respect to the direction of the d quark (or $\overline{d}$ quark). In the narrow-width approximation and at leading order in perturbative QCD, the muon transverse momentum p_T and the W boson mass M_W fulfill the relation $1-\cos^2\theta^* =$

$4p_T^2/M_W^2$ for $p_T \lesssim M_W/2$. The W and muon rapidities are related as

$$|y_W - y_\mu| \simeq \ln\left[\frac{M_W}{2p_T} + \sqrt{\left(\frac{M_W}{2p_T}\right)^2 - 1}\right] \tag{1.13}$$

This relation shows that with increasing p_T, y_μ gets closer to y_W, and the lepton charge asymmetry tends to follow the W boson production asymmetry.

Figure 1.6 shows the theory prediction generated using RESBOS [50] with CTEQ6.6 parton distribution functions [52] for the W boson production asymmetry and the muon charge asymmetry in different muon p_T bins. The muon charge asymmetry is dominated by the $V - A$ decay asymmetry at high rapidity. At high p_T, the asymmetry from W boson production becomes more important.

The muon charge asymmetry is also sensitive to the momentum of the W boson. As shown in Figure 1.7(b,c), the lepton asymmetries for different W boson momentum bins are shifted in opposite directions for low and high muon p_T. The dependence of the asymmetry on the Wp_T is smaller for the inclusive muon p_T bin, Figure 1.7(a).

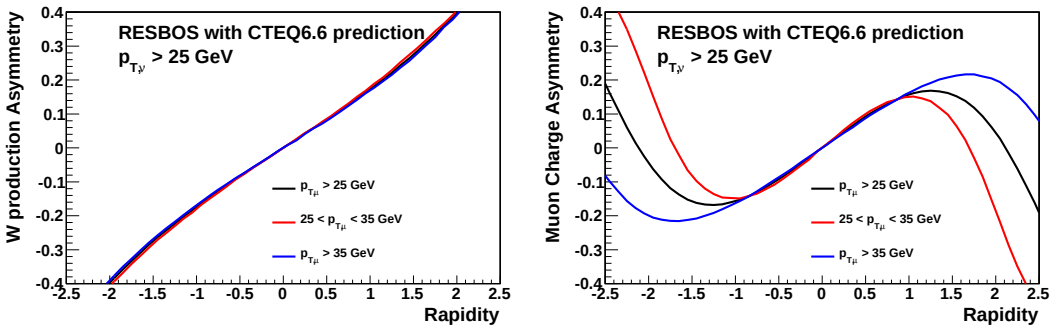

(a) W production asymmetry

(b) Muon charge asymmetry

Figure 1.6: Theory prediction for the (a) W boson production asymmetry and (b) muon charge asymmetry in different muon p_T bins: above 25 GeV (black), 25–35 GeV (red), above 35 GeV (blue).

The lepton charge asymmetry in W boson decay from $p\overline{p}$ collisions has been measured by both the CDF [21, 22, 23] and DØ [24, 25] Collaborations. The most recent lepton charge asymmetry measurement published by the DØ Collaboration was done in the electron channel using 0.75 fb^{-1} of data. A measurement of the W boson production asymmetry

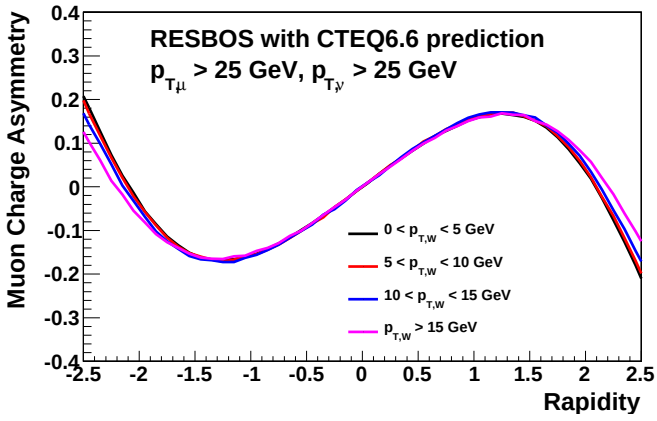

(a) $p_{T,\mu} > 25$ GeV

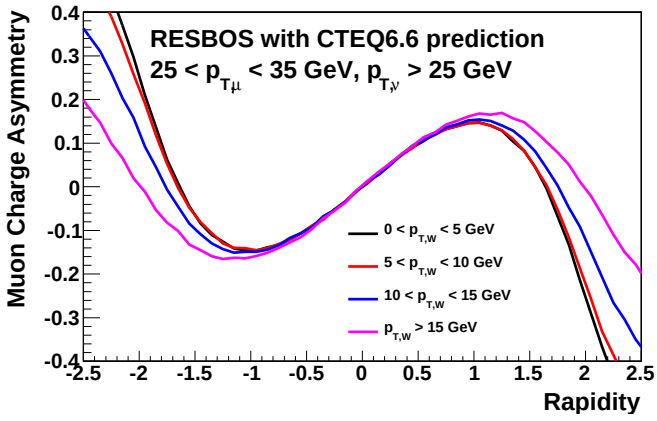

(b) $25 < p_{T,\mu} < 35$ GeV

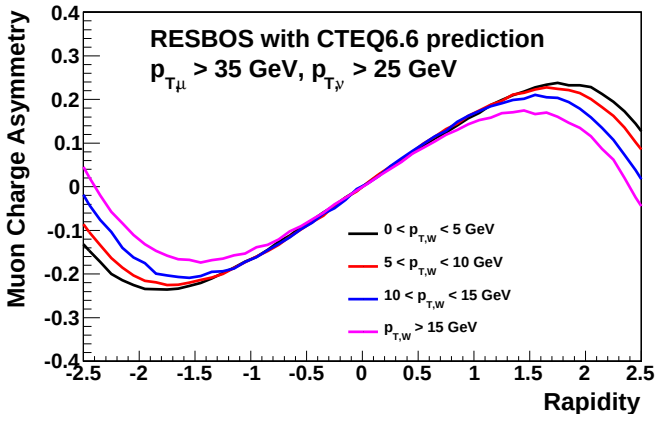

(c) $p_{T,\mu} > 35$ GeV

Figure 1.7: Muon charge asymmetry in different W p_T bins: 0–5 GeV (black), 5–10 GeV (red), 10–15 GeV (blue), and above 15 GeV (pink).

was performed using 1 fb^{-1} of data by the CDF Collaboration [26]. At the LHC, the lepton charge asymmetry in pp collisions, where W bosons have a different primary production channel, was measured by the ATLAS [27] and CMS [28] Collaborations using integrated luminosities of 31 pb^{-1} and 36 pb^{-1}, respectively.

In this dissertation, the muon charge asymmetry is measured using 7.3 fb^{-1} of $p\overline{p}$ data. This measurement provides constraints on the ratio of the u and d quark PDFs in the region $0.005 \lesssim x \lesssim 0.3$ at $Q^2 \approx M_W^2$.

CHAPTER 2

EXPERIMENTAL APPARATUS

The Tevatron is a superconducting synchrotron with a circumference of 6.3 kilometers located in Batavia, Illinois. For many years, it was the highest energy collider. In March 2010, the the Large Hadron Collider (LHC) in Switzerland started to collect data and became the world's highest energy collider. At the Tevatron, protons and antiprotons are accelerated through a chain of accelerators and steered toward each other so that they collide in the center of two detectors, DØ and CDF (Collider Detector at Fermilab) at a center-of-mass energy $\sqrt{s} = 1.96$ TeV. The measurement described in this dissertation is done with data collected with the DØ detector.

2.1 The Tevatron accelerator complex

The Tevatron accelerator chain produces and guides protons and antiprotons through a series of accelerators including the Cockcroft-Walton preaccelerator, the Linac (a linear accelerator), the Booster (a synchrotron), the Main Injector, the antiproton source, and the Tevatron (see Figure 2.1). A detailed description of the accelerator complex is in Ref. [29].

Starting with the Cockcroft-Walton preaccelerator, negative hydrogen ions are produced and accelerated to 750 keV. They are then sent to the Linac, a 150 m linear accelerator, and accelerated to 400 MeV. At the end of the Linac, the hydrogen ions go through a carbon foil where protons are created by stripping electrons from the negative hydrogen ions. Next, the protons are sent to the Booster, a fast synchrotron that increases the protons' energies to 8 GeV. The Booster then sends protons to the main injector in pulses, separated by ≈ 1.5 s.

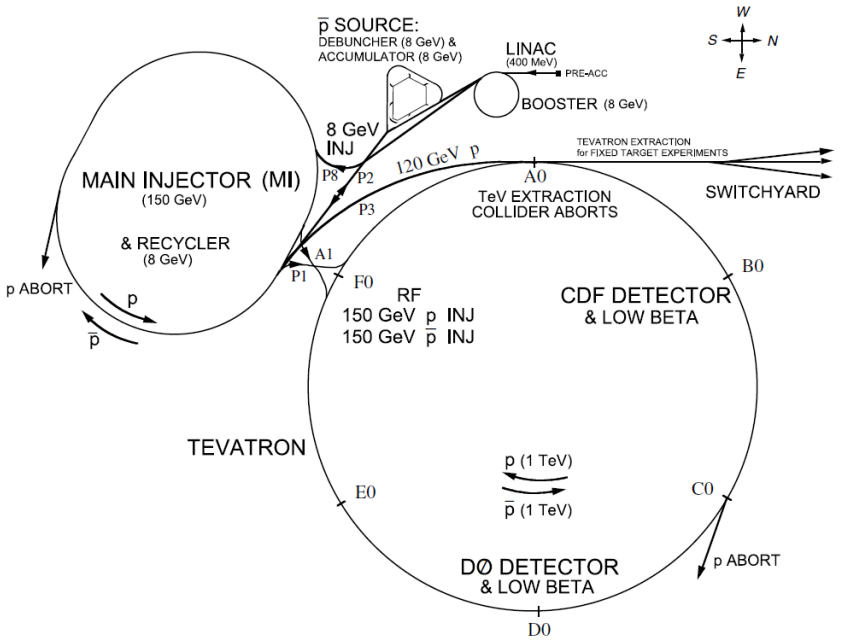

Figure 2.1: The Tevatron accelerator chain [30].

The next stage is the main injector. It provides protons for the antiproton source and accelerates protons and antiprotons to 150 GeV to inject into the Tevatron. In the antiproton source, protons extracted from the Main Injector at 120 GeV collides with a nickel target. The collisions produce antiprotons and many other secondary particles. Then 8 GeV negatively charged particles, of which only $\approx 1\%$ are antiprotons, are selected and sent to a triangular accelerator, called the Debuncher. The Debuncher is used to select antiprotons and reduce their momentum spread and transverse profile. The antiprotons are stored in an accumulator until sufficient antiprotons have been produced. They are then sent to the Recycler, a further storage ring located on top of the Main Injector. Here, the antiprotons are kept at a constant energy of 8 GeV until they are needed by the Tevatron.

Before being injected to the Tevatron, protons' and antiprotons' energies are ramped up to 150 GeV in the Main Injector. The Tevatron, the final accelerator stage, is a synchrotron with a radius of 1 km. It increases the particles' energies to 980 GeV. The Tevatron uses dipole magnets to guide the protons and antiprotons moving in opposite directions around the synchrotron ring. At the two collision points, where the DØ and CDF detectors are

located, the beams are focused to collide at the centers of the detectors.

There are 36 bunches of protons and 36 bunches of antiprotons. The proton and antiproton bunches cross each other every 396 ns. The rate of the collisions, called luminosity ($\mathcal{L}$), is determined as

$$\mathcal{L} = \frac{f N_p N_{\overline{p}}}{4\pi\sigma_p\sigma_{\overline{p}}} \tag{2.1}$$

where f is the crossing frequency of the bunches, N_p ($N_{\overline{p}}$) is the number of protons (antiprotons) per bunch, σ_p ($\sigma_{\overline{p}}$) is the transverse width of the proton (antiproton) beam.

Integrated luminosity, the amount of luminosity over a time period, is frequently used to represent the amount of data collected from the detector.

2.2 The DØ detector

After being upgraded in 2001, the DØ detector was expected to record 4 fb^{-1} of data. In 2011, 10.7 fb^{-1} of data were recorded with a peak luminosity of 3–4$\times10^{32}$ cm^{-2}s^{-1}. The DØ detector was designed to provide information about particles created from the collisions.

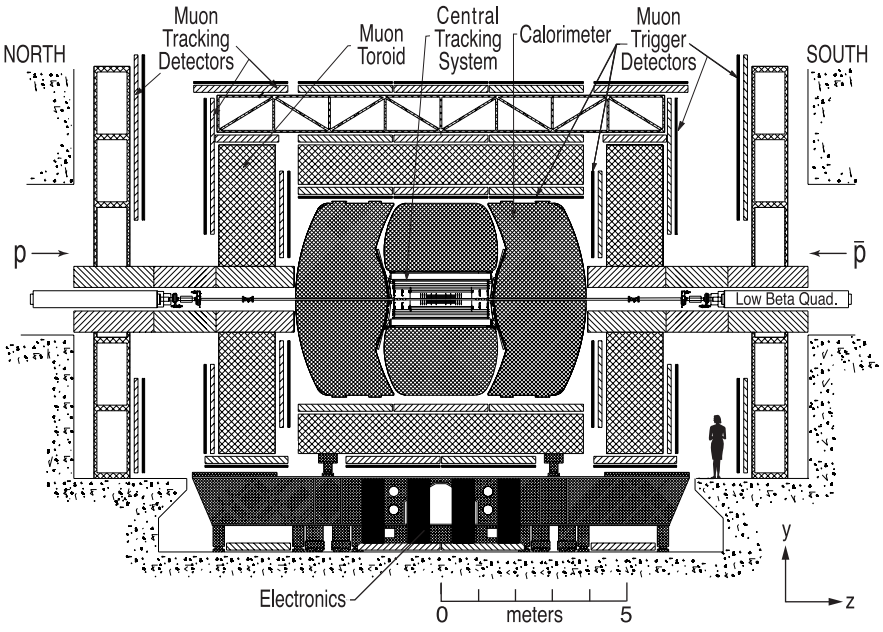

Figure 2.2: A side view of the DØ detector [31].

Figure 2.2 shows the structure of the detector. The DØ detector consists of a central tracking system, a calorimeter, and a muon system. The central tracking system consists of a silicon microstrip tracker (SMT) and a central fiber tracker (CFT) and is located within a 2 T superconducting solenoidal magnet. The liquid-argon and uranium calorimeter has a central section and two end caps. The muon system consists of three layers of scintillator trigger counters and tracking detectors: one layer before a 1.8 T toroidal magnet and two layers outside the magnet. A detailed description of the DØ detector is in Ref. [31].

We use a right-handed coordinate system in which the origin is at the center of the detector. The z-axis is along the proton direction and the y-axis is vertically upward. The angles ϕ and θ are respectively the azimuthal and polar angles.

The pseudorapidity is defined as $\eta = -\ln[\tan(\theta/2)]$. If a particle's energy is much larger than its mass, the pseudorapidity approximates the rapidity. η measured respect to the primary interaction vertex is referred to physics η, while η measured respect to the center of the detector is referred to detector η ($\eta_{\rm det}$).

2.2.1 Tracking detectors

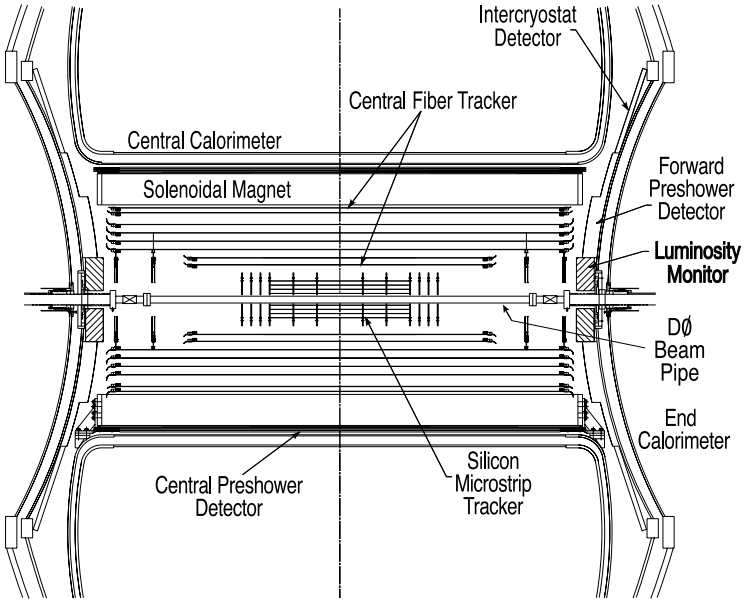

Figure 2.3: The central tracking system [31].

Figure 2.3 shows details of the central tracking system. The tracking system provides information about the interaction vertex and the outgoing charged particles. The charged particles interact with the tracking system and create patterns of hits which can be used to reconstruct the particles' paths and momenta.

The SMT is located closest to the beam pipe. It is designed for high resolution tracking near the interaction point. The SMT consists of six longitudinal silicon barrels interspersed with 16 radial disks (twelve F-disks and four H-disks) (see Fig. 2.4). Each longitudinal barrel has four layers arranged axially around the beam pipe. The SMT provides coverage in $|\eta_{\text{det}}|$ to 3 and total 792,576 readout channels.

In 2006, an inner barrel called Layer 0 was installed just outside the beam pipe to improve the tracking resolution and to compensate for radiation damage at the innermost layer of the SMT.

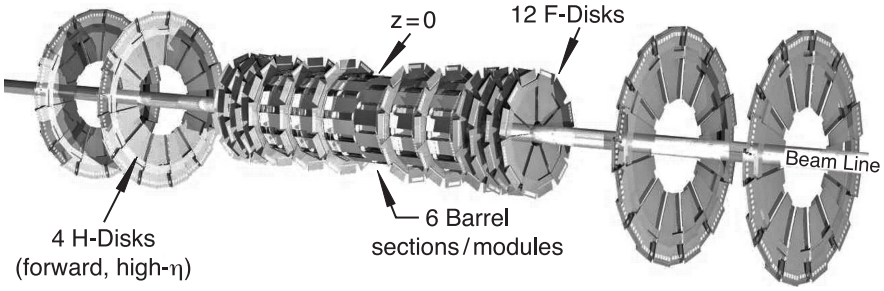

Figure 2.4: The silicon microstrip tracker [31].

The CFT sits outside the SMT and covers $|\eta_{\text{det}}| \lesssim 2.5$. It consists of eight coaxial barrels. Each barrel has two doublets of overlapping scintillating fibers. One doublet is parallel to the beam pipe and the other alternates by $\pm 3^\circ$ in ϕ relative to the axial layer. The photon signals from the scintillating fibers are transfered via clear fibers to the visible light photon counters (VLPCs) located underneath the detector.

Both the SMT and the CFT are located within a 2 T solenoidal magnetic field. It bends the charged particles' trajectories and helps to improve tracking and momentum resolution. The solenoidal field in the tracking system and the toroidal field in the muon system are frequently reversed to reduce any asymmetry from the detector.

Beyond the solenoid and in front of the calorimeter are the preshower detectors. They

are used to measure the energy losses due to the presence of the solenoid and to aid in electron and photon identification and triggering.

2.2.2 Calorimeter

Other important parts of the detector are three liquid-argon/uranium calorimeters including a central calorimeter (CC) and two end calorimeters (ECs) (see Figure 2.5). Each is contained in a separate cryostat. The central calorimeter covers $|\eta_{\rm det}| < 1$ and the two end calorimeters extend the coverage to 4.2. In addition, inner cryostat detectors (ICD) are installed to cover the gaps between the cryostats ($1.1 < |\eta_{\rm det}| < 1.4$).

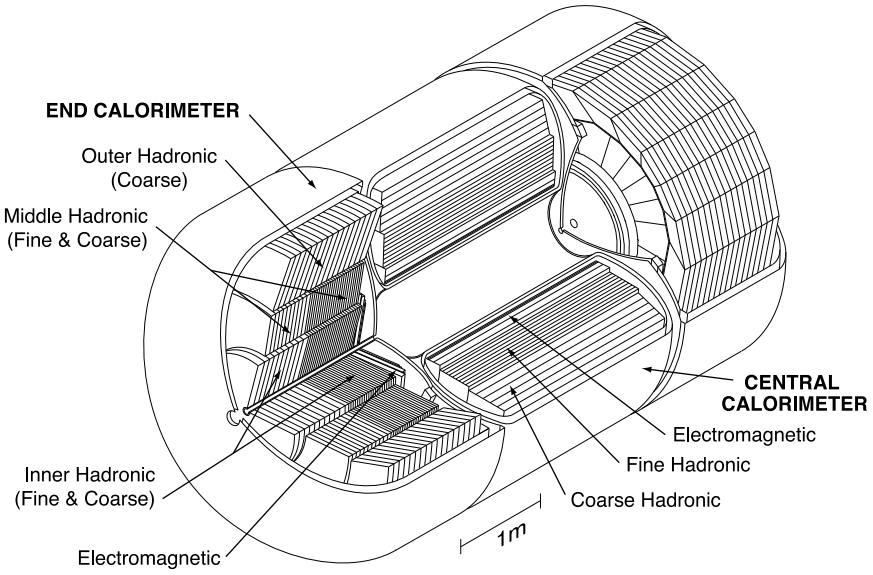

Figure 2.5: Isometric view of the calorimeter [31].

The DØ calorimeter uses a combination of metal absorbers and active liquid (liquid argon) to measure particles' energies. Different absorber materials are used to optimize the energy measurements for different types of particles. There are three sections: electromagnetic (EM), fine hadronic (FH), and coarse hadronic (CH). The EM section is used to absorb particles that interact electromagnetically, electrons and photons. The hadronic sections are used for particles that pass through the EM section but have strong interactions with the absorber materials of the hadronic calorimeters and develop hadron showers. The absorbers in the EM layers are thin, nearly pure, depleted uranium plates. The thickness

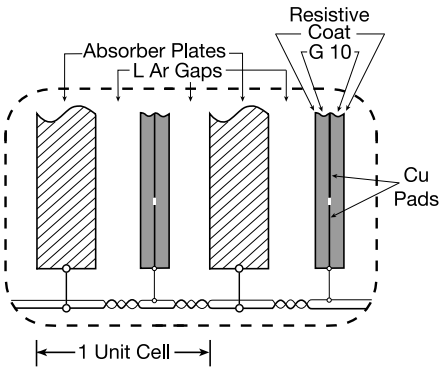

Figure 2.6: Layout of a calorimeter cell [31].

of the EM absorbers are (1.4, 2.0, 6.0, and 9.8 X_0) for the CC, and (1.6, 2.9, 7.9, 9.3 X_0) for the EC, where X_0 is one radiation length. The FH layers use 6 mm thick plates made from uranium-niobium alloy, and the CH layers use 46.5 mm thick plates of copper (in the CC) or stainless steel (in the EC). The calorimeter is built up from cells. A calorimeter cell consists of an absorber plate and a copper resistive plate with ≈ 2 kV in between. The gaps between the plates are filled with liquid argon (see Figure 2.6). The calorimeter cell typically has a size of 0.1×0.1 in $\Delta\eta \times \Delta\phi$. Cells in the third layer of the EM section have a smaller size of 0.5×0.5 to improve the spatial resolution of the EM shower centroids. The cells are grouped in modules (32 EM modules, and 16 FH and CH modules). There are 47,032 active readout channels connected to physical readout modules in the cryostats.

2.2.3 Muon detector

The muon system is the outermost layer of the DØ detector. It consists of a central muon system using proportional drift tubes (PDTs) and a forward muon system using mini drift tubes (MDTs). The central region covers $|\eta_{\rm det}| < 1$ and the forward region covers $1 < |\eta_{\rm det}| < 2$. The drift tubes are used to measure muons' coordinates and to aid in triggering. In addition, scintillation counters are also installed in both regions for triggering and for rejecting out-of-time background events.

Figure 2.7 shows exploded views of the muon wire chambers and the scintillation counters in the muon detector. The muon detector has three layers. The inner most layer (layer A) lies in front of a 1.8 T toroidal iron magnet. The other two layers (B and C) lie outside

the magnet. The toroidal magnet is used to measure muon momentum independently of the tracking system. This is useful for setting a low-p_T cutoff in the Level 1 trigger, providing a cleaner matching of a muon to a central track, eliminating π/K decays, and improving the momentum resolution for high momentum muons.

The muon detector is poorly instrumented at the central region underneath the detector to leave space for the detector support structure and the electronic readout hardware. More information about the muon system can be found in Ref. [32].

2.2.4 Luminosity monitor

The Tevatron luminosity at the DØ interaction point is measured by detecting inelastic $p\overline{p}$ collisions with the luminosity monitors (LMs). Each of the LMs consists of 24 plastic scintillation counters with photo multiplier tube (PMT) readouts. They are located at $z = \pm 140$ cm, in front of the end calorimeters, and cover the range $2.7 < |\eta_{\text{det}}| < 4.4$ (see Figure 2.8).

The luminosity monitors are also used to determine beam halo rates and to make a fast measurement of the z coordinate of the primary vertex.

2.2.5 Trigger and data acquisition

Figure 2.9 shows the outline of the DØ trigger and data acquisition systems. The trigger system consists of three levels. It is used to select interesting physics events and to reduce the event rate from ≈ 1.7 MHz to ≈ 50 Hz in order to record data to tape.

The first trigger level (Level 1) uses preliminary information from the tracking, calorimeter, and muon systems to reduce the rate to ≈ 2 kHz. The Level 1 central track trigger (L1CTT) looks for predefined track patterns which are consistent with the passages of charge particles. The Level 1 calorimeter trigger (L1Cal) looks for energy deposition patterns with transverse energies above predefined thresholds. And the Level 1 muon trigger (L1Muon) uses information from the muon system or connects the wire chamber signals with the tracks from the CTT to find predefined muon patterns. Transverse momentum thresholds may also be used in the L1CTT and L1Muon decisions.

The event rate is reduced further to ≈ 1 kHz in Level 2. In this level, global decisions are based on data collected from the Level 1 trigger and from different detector subsystems

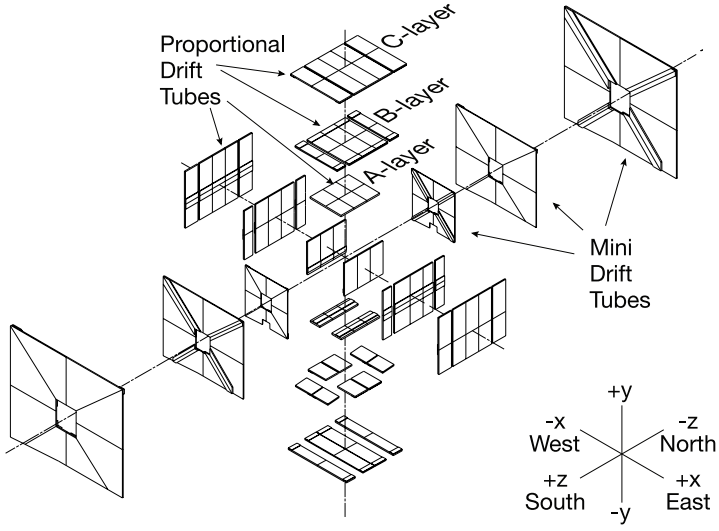

(a) The muon wire chambers

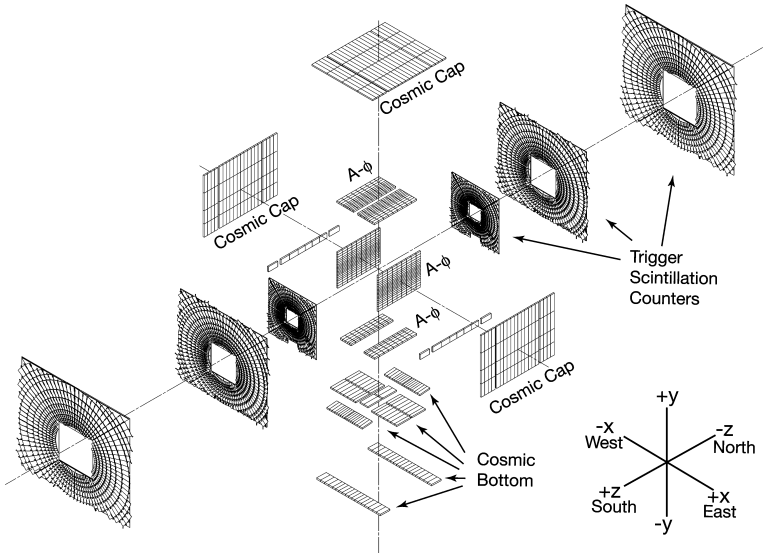

(b) The muon scintillation counters

Figure 2.7: Exploded views of (a) the muon wire chambers and (b) the muon scintillation counters [31].

to search for more specific particle signatures.

While the first two levels rely mainly on hardware and firmware, Level 3 uses software algorithms and a computing farm to reconstruct events quickly using all available detector information. The event rate is reduced to $\approx$ 50 Hz to write to tape for analysis.

The performance of each subsystem is carefully monitored. If there are problems in the detector that could affect the data quality, those events are tagged as bad by the data quality group [40] and are removed from the analysis.

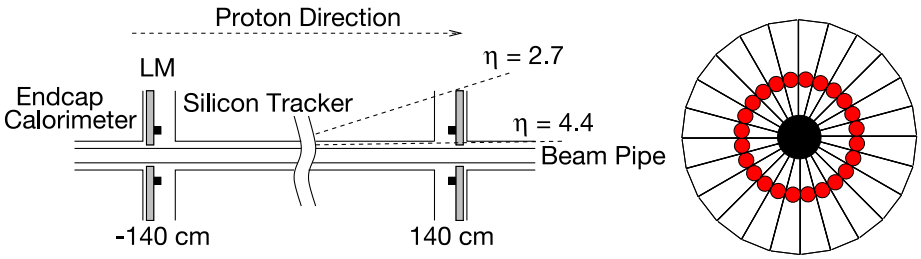

(a) (b)

Figure 2.8: Luminosity monitor: (a) locations of the luminosity monitors, (b) geometry of the LM counters. The solid dots represent the locations of the PMT readouts [31].

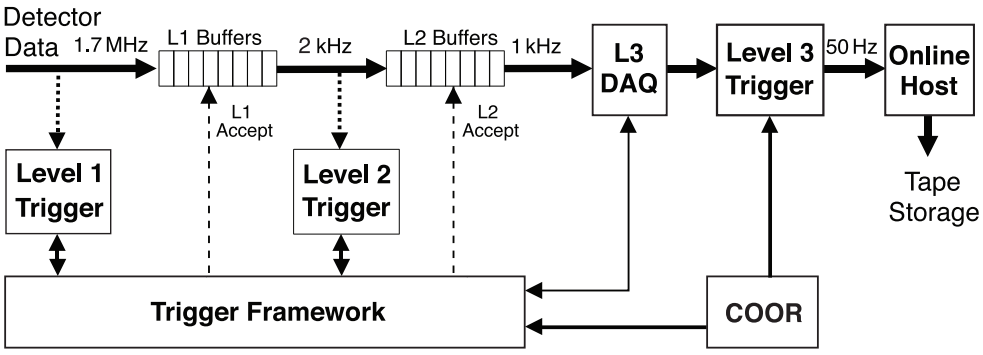

Figure 2.9: Outline of the DØ trigger and data acquisition systems [31].

CHAPTER 3

EVENT RECONSTRUCTION

In order to be used in the analysis, event information from the detector such as detector hits and energy deposits must be translated to physics objects. A sophisticated offline program called DØRECO [33] is used to reconstruct objects and their properties. This section describes the reconstruction algorithms for objects most relevant to this analysis such as tracks, primary vertices, muons, jets, and missing transverse energy. The Monte Carlo simulations used in this analysis are also introduced.

3.1 Charged tracks

To reconstruct tracks, DØ uses two tracking algorithms, the Alternative Algorithm (AA) [34] and the Histogram Track Finder (HTF) [35]. Hit information from the SMT and the CFT are fed to the two algorithms in parallel to create a pool of track hypotheses. Duplicated tracks are then removed from the pool.

3.1.1 Alternative Algorithm

The AA method begins with constructing an initial hypothesis from three hits in the SMT. Reconstruction begins at the innermost SMT layer outwards with the following conditions:

- the first hit can be in any barrel layers or F-disks
- the angle $\Delta\phi$ between the first and second hits, as seen from the beam spot, is less than 0.08 (see Figure 3.1)
- the radius of circle of the track hypothesis is greater than 30 cm (corresponding to a track p_T of 180 MeV).

In addition, the fit of these hits to the track hypothesis must has $\chi^2 < 16$. The minimum transverse distance of the track hypothesis to the beam spot (impact parameter) must be less than 2.5 cm.

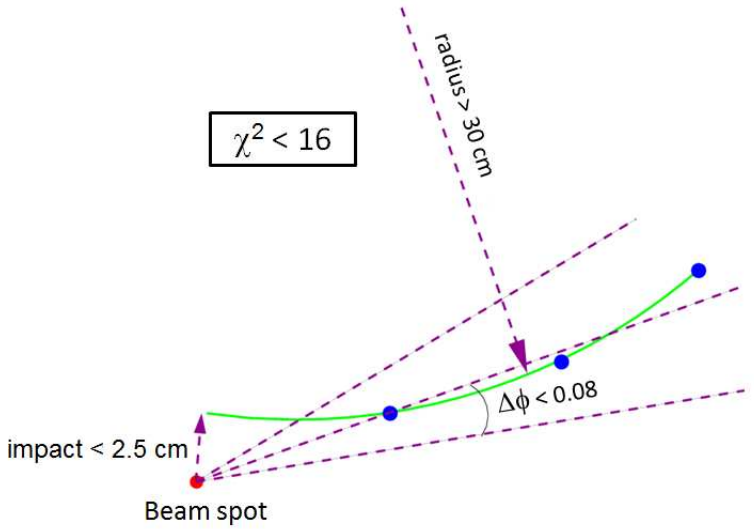

Figure 3.1: Schematic of the track hypothesis construction in the AA method [34].

The track hypothesis is then extrapolated to the rest of the tracking system. CFT hits are added to the track hypothesis as long as the χ^2 is less than 16. If more than one hit is found in a given layer, a corresponding number of new hypotheses is constructed.

If a given layer does not have hits in the expectation window, it is called a missing hit (miss). The miss lying in between two hits of a hypothesis is defined as an inside miss, and a forward (backward) miss is a miss in the forward (backward) track extrapolation.

Construction of the track continues until the end of the tracking system or until three misses are found consecutively. A track hypothesis is saved in the pool if it satisfies following conditions

- $N_{\text{hit}} \geq 4$
- $N_{\text{miss}} < (1/5)N_{\text{hit}}$
- $N_{\text{inside miss}} \leq 3$
- $N_{\text{SMT inside miss}} \leq 2$

- $N_{\text{inside miss}} + N_{\text{forward miss}} \leq 4$
- $N_{\text{inside miss}} + N_{\text{backward miss}} \leq 3$

where $N_{\text{hit(miss)}}$ is the number of hits (misses) in the hypothesis.

Two or more track hypotheses can share the same hits. An AAtrack is determined based on the number of shared axial hits (N_{shared}) and the total number of axial hits (N_{total}) as following

- $N_{\text{shared}} \leq (2/3)N_{\text{total}}$
- $N_{\text{shared}} \leq (1/5)N_{\text{total}}$ or $N_{\text{total}} - N_{\text{shared}} > 3$.

For tracks that have few or no hits in the SMT, the track construction is run again using hits in the CFT and the primary vertex information. This measurement uses tracks with at least 1 SMT hit to reduce background from in-flight decays of pions and kaons.

3.1.2 Histogram Track Finder

The position of a charged particle in a homogeneous magnetic field **B** in vacuum can be determined by three parameters: the curvature ($\rho = q|\mathbf{B}|/p_T$, where q is the particle charge), the impact parameter (d_0), and the azimuthal angle (ϕ) of the track at the point of closest approach to (0,0) in (x,y) space. The HTF method uses a Hough transformation [36] to convert the SMT hit positions in (x,y) space into lines in (ρ,ϕ) space. These lines fill a 2D histogram and the track candidates correspond to peaks in the histogram where the lines cross. As the histogram is created, a Kalman filter [37] is applied to these track candidates. Tracks with large χ^2 are removed. The track candidates are then extrapolated outwards to the CFT. The reverse process is also applied. The fit starts with hits in the CFT and extrapolates the track candidates into the SMT.

3.2 Primary vertex

Determining the primary vertex (PV) corresponding to a hard scattering collision among multiple $p\overline{p}$ collisions is important for reducing background and measuring transverse energies in the calorimeter.

In this process, a list of primary vertices is created from tracks satisfying the following conditions [38]:

- track $p_T > 0.5$ GeV
- at least 2 SMT hits
- $dca/\sigma_{dca} \leq 100$, where dca is the distance of closest approach of the track with respect to a common vertex.

The tracks that are within 2 cm of each other are grouped in the z direction. They are then fitted to determine a common vertex position corresponding to a minimum χ^2 using the Kalman filter. The vertex finding process is done again with a tightened selection of $dca/\sigma_{dca} \leq 3$. This allows more high p_T tracks to be associated to the primary vertex.

Next, the list of primary vertices is ordered based on their minimum bias probabilities. This probability is determined from the minimum bias probabilities of the associated tracks (the probability that the track comes from an inelastic scattering). The vertex with the smallest minimum bias probability is then chosen as the hard scattering interaction vertex.

3.3 Muon

When a muon interacts with the detector, it creates a track in the central tracking system and does not deposit much energy in the calorimeter. Therefore, the muon reconstruction is performed using information from the the muon system and central tracks.

Muon reconstruction [39] starts with linking hits within 20 cm of each other to form a local segment in each muon detector layer. The hits can not be in the same plane and not in the same underlying wire hit. If positions and directions of two local segments form a straight line, they are linked to form a larger segment. The segments are then fitted to scintillator hits to determine the segments' timing information.

The vertex is also lined up to segments in the A layer to improve the the angular resolution. Local segments in the B and C layers are matched to create a larger segment. The local segments are then filtered to keep those with the lowest χ^2 (the segments are fitted to a straight line path).

Finally, the local muons found in the muon system are extrapolated inward to the central tracking system to find associated tracks. The momentum of the muon with a matched central track is determined by the track momentum.

The muon identification (ID) quality is classified as loose, medium, and tight qualities based on the numbers of hits in the A and BC layers. A detailed description of muon ID qualities can be found in Ref. [40]. In this measurement, the W boson is reconstructed from an isolated muon matched to a central track. The muon candidates have medium quality with hits in the A and B-or-C layers (mediumnseg3 quality). They have at least two A layer wire hits, at least one A layer scintillator hit, and at least two BC layer wire hits.

The isolation requirement is used to eliminate secondary muons from heavy flavor quark decays. The muon isolation is determined from two parameters: EtHalo and EtTrkCone. EtHalo is the scalar sum of the transverse energies measured in the calorimeter inside a hollow cone $0.1 < R < 0.4$ around the muon. EtTrkCone is the scalar sum of all transverse momenta inside a cone of $\Delta R < 0.5$ around the muon (except the muon track).

As muons from cosmic rays are uncorrelated with $p\overline{p}$ collisions, they can effectively be vetoed by constraints in the scintillator timing, the *dca*, and the acollinearity between central tracks.

3.4 Jets

In the calorimeter, energy cells are added in towers of size $\Delta\eta \times \Delta\phi = 0.1 \times 0.1$. These towers are used as inputs for jet reconstruction using the RunII cone algorithm [42]. Towers with $p_T > 1$ GeV are chosen as precluster seeds. The seeds are combine with adjacent jets within a cone size $\Delta R < 0.3$ to form preclusters. Jet clusters are built up from preclusters in a cone size $\Delta R = 0.5$ around the jet centroid. Jet clusters with transverse energies less than 8 GeV are removed. If the same towers are shared by two jets and the shared energy is larger than 50% of the least energitic jet, the jets are merged. Otherwise the shared towers are split between the jets.

Due to calorimeter noise or out-of-cone energy deposition, the measured jet energy is not the true deposited energy from a parton. Therefore, a jet energy scale (JES) is need to correct the jet back to parton-level. The true jet energy ($E_{\rm jet}^{\rm true}$) is calculated from the measured jet energy ($E_{\rm jet}^{\rm meas}$) as [43]

$$E_{\rm jet}^{\rm true} = \frac{E_{\rm jet}^{\rm meas} - E_{\rm o}}{R_{\rm jet} \times S_{\rm jet}} \tag{3.1}$$

where E_{o} is the energy offset from noise, minimum bias interactions, and events from previous crossings. R_{jet} is the energy response of the calorimeter. S_{jet} is the fraction of the jet energy inside the jet cone.

3.5 Missing transverse energy

Neutrinos go through the detector without interacting with detector materials. The longitudinal component of the neutrino momentum cannot be measured because remnants of the collision are lost in the beam pipe. Its transverse energy can be inferred from the missing transverse energy ($\not\!\!E_T$) which is an energy imbalance in the transverse plan. $\not\!\!E_T$ is defined as a negative of the vector sum of all transverse momenta in the event. $\not\!\!E_T$ could come from physics objects that escape the detector without energy deposits like neutrinos, or from instrumental sources such as a noisy calorimeter, physics object resolution, etc.

To measure $\not\!\!E_T$, the calorimeter cells including the electromagnetic and fine hadronic parts are added to form a raw $\not\!\!E_T$. The coarse hadronic cells are excluded because they usually have higher noise and negative energy cells. Then, the raw $\not\!\!E_T$ is corrected for muon momenta and jet energies for a best neutrino transverse energy measurement. Muon momenta are added to the raw $\not\!\!E_T$, and the raw energy cells associated with jets are replaced with corrected energies [45].

3.6 Monte Carlo simulation

In this analysis, Monte Carlo (MC) simulation is used for estimating backgrounds from electroweak processes, correcting the muon charge asymmetry for effects from the detector, and creating theory predictions. MC generators are chosen based on purpose, speed of generating events, and the available framework for PDF sets.

3.6.1 PYTHIA

Backgrounds from electroweak processes are determined using the PYTHIA [46] generator with a full simulation process. The PYTHIA program simulates hard scattering processes at leading order in perturbation theory and combines with a non-perturbative model of

hadronization process. To take into account the composite nature of protons (and antiprotons) in the $p\overline{p}$ collisions, the PYTHIA generator is interfaced to the CTEQ6.1M PDFs. After being generated by PYTHIA, MC events are passed through a GEANT based simulation [47] program called DØgstar [48] to simulate the detector response. GEAN is a simulation program that models and simulates the interactions of particles with matter. DØgstar uses the GEANT libraries to determine energy deposits of particles in the detector. Then the DØSim [49] program is used to simulate the digitization process, the calorimeter pileup from previous events, and the electronics noise. It also merges randomly the MC hard scattering processes with triggered bunch crossings from data to simulate the effects from additional $p\overline{p}$ collisions.

However, PYTHIA MC events are not accurately matched to data. For instance, the muon p_T resolution in MC is more optimistic than in data, reconstruction efficiencies for muons are not precise, MC events does not have trigger simulation, and PYTHIA does not simulate the W boson p_T distribution well. Therefore, further corrections for theses inaccuracies are applied in the analysis.

3.6.2 RESBOS+PHOTOS

The RESBOS [50] generator has gluon resummation at low W boson p_T and NLO perturbative QCD calculations at high W boson p_T. The RESBOS events are generated with CTEQ6.6 PDFs. The PHOTOS [51] is used to correct for QED final state radiation.

RESBOS events are used to produce theory predictions for the muon charge asymmetry and to study smearing effects from the detector. About 50M events are generated and smeared (without going through GEANT) using a parametrized version of the muon p_T and the $\not\!\!E_T$ resolutions. The smearing is tuned such that the muon p_T and the $\not\!\!E_T$ resolutions are matched to those in data (see Section 4.6.4 for more information). This method is much faster than the full simulation and therefore allows generation of many events to reduce statistical uncertainties.

3.6.3 POWHEG+PYTHIA

In order to generate theory predictions with new CT10 and MSTW2008 PDF sets (which is not available in RESBOS), we use the POWHEG [54] NLO generator with PYTHIA for parton

showering. The fast simulation process described above is used to smear the POWHEG events. They are also used in the detector smearing study.

CHAPTER 4

ANALYSIS

4.1 Outline

In this analysis, we measure the muon charge asymmetry for W boson decay with 7.3 fb^{-1} of data. We use two data samples: Run IIa with 1 fb^{-1}, and Run IIb with 6.3 fb^{-1}.The analysis is done for $|\eta| < 2$ (Run IIa data) and $|\eta| < 1.6$ (Run IIb data) in bins of 0.2 in η and for $p_T^\mu > 25$ GeV (inclusive muon p_T bin), $25 < p_T^\mu < 35$ GeV, and $p_T^\mu > 35$ GeV.

To reconstruct $W \to \mu\nu$ events, we select events containing a good isolated muon matched to a central track with high transverse momentum (p_T) and high transverse missing energy ($\not\!\!E_T$). The $\not\!\!E_T$ is used as the transverse momentum of the neutrino. The requirements for event selection are described in Section 4.2.

The main backgrounds are due to electroweak processes and the multijet events. The electroweak background is due to the physics processes $W \to \tau\nu$, $Z \to \mu\mu$, and $Z \to \tau\tau$. It is estimated using Monte Carlo simulation as described in Section 4.5.1. In Section 4.5.2, we describe the method to estimate the multijet background, which comes primarily from semileptonic decays of heavy quarks.

The muon charge asymmetry is then corrected for the difference of ε^+ and ε^-, where $\varepsilon^\pm$ are the average efficiencies of positive and negative muons over a given muon (p_T,η) region. There is a difference because the muon p_T distributions of positive and negative muons are not identical for a given η bin, especially at high muon pseudorapidity. The muon efficiency is calculated from the tag-and-probe method as presented in Section 4.3, and then it is folded into the muon p_T distribution of the $W \to \mu\nu$ events to calculate the efficiency correction.

We also measure the muon charge misidentification probability, dilutes the muon charge asymmetry. We use $Z \to \mu\mu$ events to estimate the muon charge misidentification probability with the tag-and-probe method. The muon charge misID probability is insignificant as shown in Section 4.4.

Another possible bias is from the polarity of the solenoid. In the DØ detector, the solenoid surrounds the central tracking system. Its polarity is flipped frequently to avoid any asymmetry from the detector. However, the fractions of data collected within each solenoid polarity are not identical. Therefore, if there is an offset in the track curvature, the effects due to the solenoid will not be canceled out. This effect is discussed in Section 4.6.3.

The muon charge asymmetry is also corrected for muon p_T smearing and $\not\!\!E_T$ smearing before comparison to theory predictions. This correction is necessary because the momenta of the muon and the recoil jet are smeared out when they go through the detector. Consequently, the muon momentum and the $\not\!\!E_T$ measured by the detector are not the same as the momenta of the muon and the neutrino when they were created. The muon charge asymmetry should be corrected for this detector smearing effect in order to have an apples-to-apples comparison between the experimental results and the theory predictions. The smearing correction is described in Section 4.6.4.

The muon charge asymmetry is measured separately for Run IIa and Run IIb as presented in Sections 4.6.1 and 4.6.2. The muon charge asymmetry is CP invariant. Therefore, the CP-folded asymmetry such that $A(\eta) = -A(-\eta)$ is also measured in order to increase the statistical resolution, Section 4.6.5.

We measure the asymmetry in five (p_T^μ,p_T^ν) bins with the following kinematic cuts:

1. inclusive bin: $p_T^\mu > 25$ GeV, $p_T^\nu > 25$ GeV
2. bin 1: $25 < p_T^\mu < 35$ GeV, $p_T^\nu > 25$ GeV
3. bin 2: $p_T^\mu > 35$ GeV, $p_T^\nu > 25$ GeV
4. bin 3: $25 < p_T^\mu < 35$ GeV, $25 < p_T^\nu < 35$ GeV
5. bin 4: $p_T^\mu > 35$ GeV, $p_T^\nu > 35$ GeV.

The results for each kinematic bin are given in Sections 4.6.7 to 4.6.10.

The muon charge asymmetries for Run IIa and Run IIb are combined in Section 5.1. Finally, the combined results are compared with the electron charge asymmetry from DØ with 0.75 fb^{-1} of data and with the theory predictions from RESBOS NLO with CTEQ6.6 PDFs, and from POWHEG NLO with CT10 and MSTW2008 PDFs in Section 5.2. The measurements show good agreement between the two channels, but not with the theory predictions in non-inclusive bins.

4.2 Data samples and event selections

4.2.1 Data samples

We analyze the following data sets collected from April 2002 to July 2010 with integrated luminosity ≈ 7.3 fb^{-1}

1. Run IIa: VJets_MUinclusive_Moriond09_RunIIa_v1,
2. Run IIb1 and IIb2: VJets_MUinclusive_Summer09_RunIIb1and2,
3. Run IIb3: VJets_MUinclusive_RunIIb3_v1.

Data set (1) and a part of set (2) are skimmed from the MUinclusive data sets by the VJets group. They require at least one loose muon with $p_T > 12.5$ GeV. Another part of set (2) and set (3) require at least one loose muon with $p_T > 10$ GeV.

Within the single muon data, events tagged as bad quality in the CFT, SMT, calorimeter, muon system, solenoid or toroid by the data quality group and those with bad luminosity blocks are removed.

4.2.2 Triggers

We select events passing at least one of the single muon triggers (see Appendix A for detailed descriptions). Some of the single muon triggers of Run IIa have the maximum detector pseudorapidity ($\eta_{\rm det}$) coverage up to ± 2, where $\eta_{\rm det}$ is the pseudorapidity measured with respect to the center of the detector. This coverage in Run IIb, however, is reduced to ± 1.6 because the single muon triggers require a muon matching a central track to reduce the trigger rate.

4.2.3 Event selection

To choose good $W \to \mu\nu$ candidates, we select events with the following requirements:

1. The event passes at least one of the single muon triggers listed in Section 4.2.2.

2. The muon passes at least a mediumnseg3 quality with the following muon system conditions [40]:

   - the muon has at least two A layer wire hits and at least two BC layer wire hits
   - the muon has at least one A layer scintillator hit and at least one BC scintillator hit (except for central muons with less than four BC wire hits).

   The BC scintillator hit requirement in the central region is dropped for Run IIb.

3. The muon matches a central track with $p_T > 25$ GeV satisfying a tight track quality as follows:

   - the track has at least one hit in the SMT and at least two hits in the CFT
   - the distance of closest approach, dca, of the track to the beam position in the x-y plane satisfies $|dca| < 0.04$ cm
   - $\frac{\chi^2}{dof} < 9.5$, where χ^2 and the number of degrees of freedom (dof) are global fit parameters of the central track.

4. The central track matches a primary vertex (PV) within 2 cm in the z direction. The primary vertex is also required to lie within $|z_{PV}| < 60$ cm from the center of the detector. The radial primary vertex position must be less than 1 cm [44].

5. The muon must lie within the region of trigger acceptance, $|\eta_{\rm det}| < 2$ or $|\eta_{\rm det}| < 1.6$ as appropriate.

6. The muon must be isolated in the calorimeter and in the central tracker. The total transverse momentum of tracks in a cone of radius $R = 0.5$ in (η, ϕ) centered around the muon must be less than 2.5 GeV, and the total transverse energy measured in the calorimeter in the annulus $0.1 < R < 0.4$ centered around the muon track must be less than 2.5 GeV (NPTight requirements) [40].

7. $\Delta R(\mu, \text{closest jet}) > 0.5$, where $\Delta R(\mu, \text{closest jet})$ is the distance in (η, ϕ) space of the muon to the central axis of the closest jet with $p_T > 15$ GeV.

8. Missing transverse energy of the event $\not\!\!E_T > 25$ GeV. The $\not\!\!E_T$ is corrected for muons, coarse hadronic energy of JCCB jets, jet energy scale, and the electromagnetic energy scale.

9. Transverse mass of the μ and $\not\!\!E_T$ (M_T) must be above 50 GeV, where $M_T = \sqrt{(\not\!\!E_T + p_T^\mu)^2 - (\not\!\!E_x + p_x^\mu)^2 - (\not\!\!E_y + p_y^\mu)^2}$, and $\not\!\!E_x$ ($\not\!\!E_y$) and p_x^μ (p_y^μ) are transverse x (y) components of the missing energy and the muon momentum, respectively.

10. Cosmic ray muons are rejected using the scintillator timing cut, $|t_A| < 10$ ns.

11. $Z \to \mu\mu$ events are removed by rejecting events containing a second isolated track-matched mediumnseg3 muon or if there is a second central track with $p_T > 20$ GeV and back-to-back with the muon track in ϕ, $|\Delta\phi(\text{muon track, second track})| > 2.1$.

We select 558,886 $W \to \mu\nu$ candidates for Run IIa and 2,256,918 candidates for Run IIb. Figure 4.1 shows the W transverse mass, $\not\!\!E_T$, muon p_T, and W p_T distributions of selected events.

4.3 Muon efficiency

In this section, we present measurements of the muon identification (muon-ID) efficiency, tracking efficiency, trigger efficiency, isolation efficiency, and the total muon efficiency for a muon passing mediumneg3 muon, tight track, and NPTight isolation. The muon efficiencies not only depend on the geometry of the detector, but they are also sensitive to the instantaneous luminosity. Creating more activity in the detector environment, high instantaneous luminosity decreases the isolation and trigger efficiencies. Another factor affecting the efficiencies is the trigger filters. For Run IIb, due to the increase in the luminosity, the requirements for the single muon triggers are tightened. The tracking, isolation, and trigger efficiencies for Run IIb are significantly different from those for Run IIa.

4.3.1 Data and MC samples

We use dimuon data events with the same integrated luminosity as in the muon charge asymmetry measurement to calculate the muon efficiency. For MC muon efficiency, we use PYTHIA $Z \to \mu\mu$ events CSG_CAF_MCv4–ReqID_p18.13.01 for Run IIa and CSG_CAF_MCv4–ReqID_p21.11.00 for Run IIb. Request-IDs and numbers of events in the MC samples are listed in Table 4.1. The MC dimuon events are corrected for the luminosity profile and the beam shape of the data. The normalized luminosity and primary vertex (PV) z profiles for data and MC are shown in Figure 4.2.

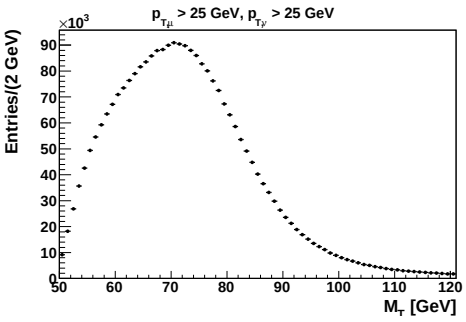

(a) Transverse mass

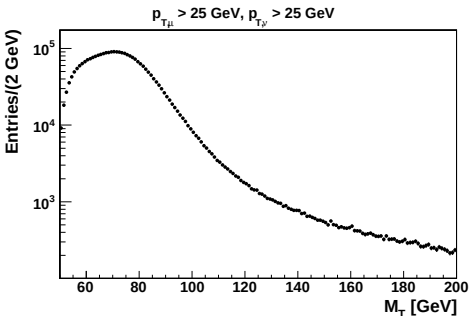

(b) Transverse mass in log scale

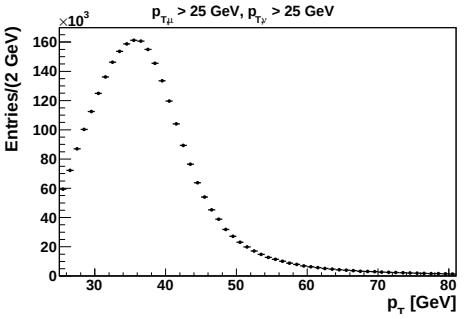

(c) Muon transverse momentum

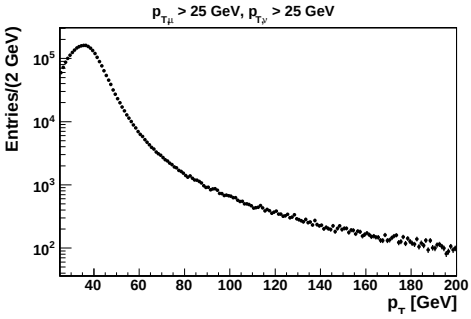

(d) Muon transverse momentum in log scale

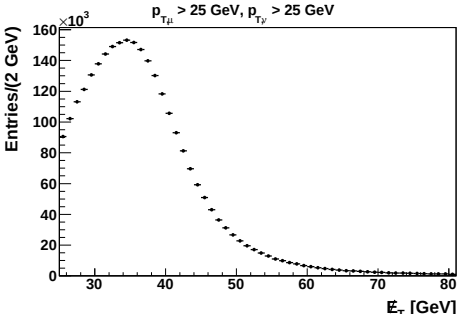

(e) Missing transverse energy

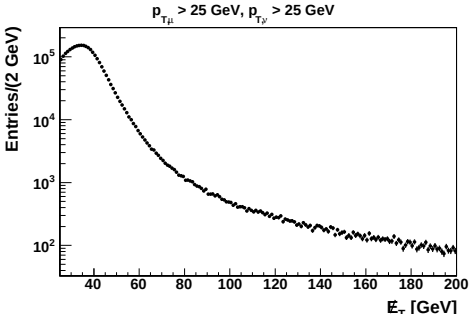

(f) Missing transverse energy in log scale

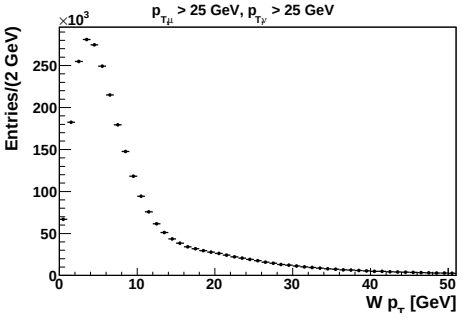

(g) W transverse momentum

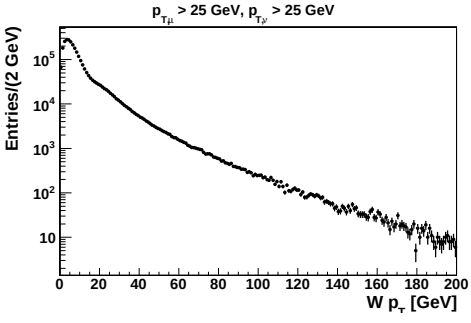

(h) W transverse momentum in log scale

Figure 4.1: W transverse mass, muon p_T, $\not\!\!E_T$, and W p_T distributions of the selected events

Table 4.1: PYTHIA MC $Z \to \mu\mu$ request-IDs and numbers of events.

Processes	Request-IDs	Number of events
Run IIa		
$Z \to \mu\mu$ $(15 < m_{\mu\mu} < 60$ GeV)	36591 $\to$ 36595, 40678 $\to$ 40687	2,999,418
$Z \to \mu\mu$ $(60 < m_{\mu\mu} < 130$ GeV)	38899 $\to$ 38912, 42047 $\to$ 42053	3,836,694
$Z \to \mu\mu$ $(130 < m_{\mu\mu} < 250$ GeV)	35709, 41252	504,091
Run IIb		
$Z \to \mu\mu$ $(15 < m_{\mu\mu} < 60$ GeV)	75077 $\to$ 75081	999,378
$Z \to \mu\mu$ $(60 < m_{\mu\mu} < 130$ GeV)	75087 $\to$ 75089, 86872 $\to$ 86876	1,499,154
$Z \to \mu\mu$ $(130 < m_{\mu\mu} < 250$ GeV)	75092, 75093	292,503

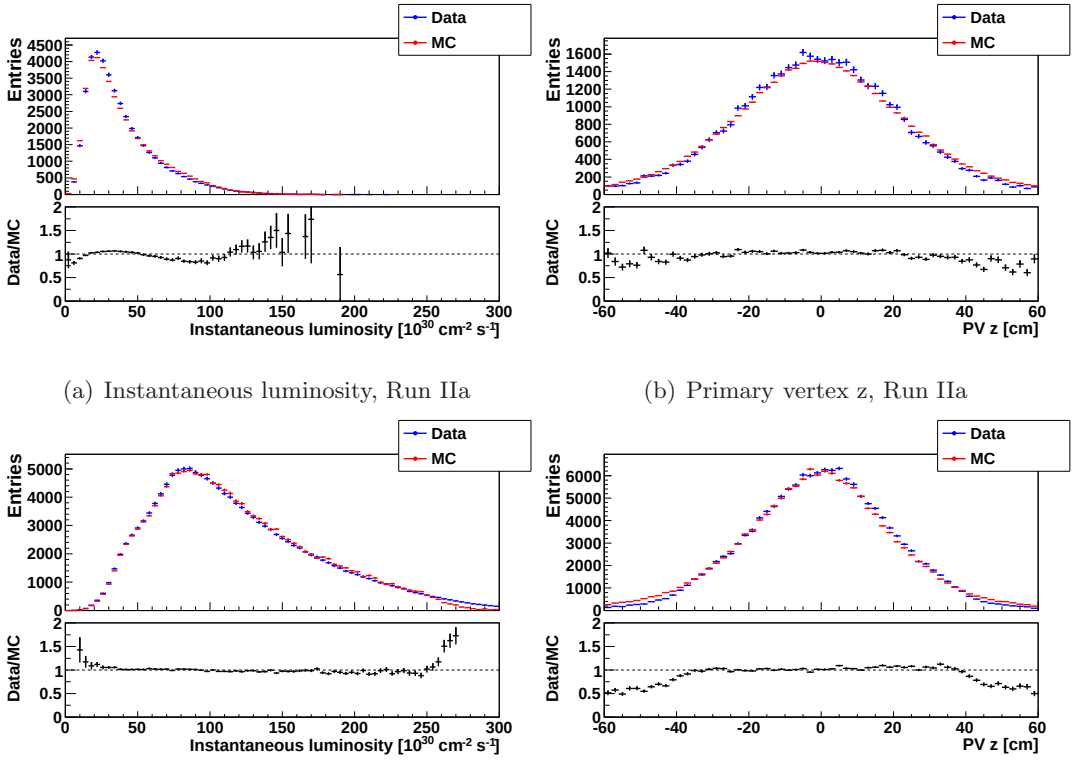

(a) Instantaneous luminosity, Run IIa

(b) Primary vertex z, Run IIa

(c) Instantaneous luminosity, Run IIb

(d) Primary vertex z, Run IIb

Figure 4.2: Normalized luminosity and primary vertex z distributions for data and MC.

4.3.2 Tag-and-probe method

The efficiencies are measured using the tag-and-probe method. A muon from a $Z \to \mu\mu$ event is used as a tag, and another muon called the probe is used to measure the probability that the probe passes a required quality. The $Z \to \mu\mu$ events are reconstructed with the following conditions:

- the events pass at least one of the single muon triggers listed in Section 4.2.2
- the primary vertex is required to be $|z_{\rm PV}| < 60$ cm, and Δz(tag,PV) < 2 cm
- the radial primary vertex position < 1 cm
- the tag muon passes the following requirements:
  - loose muon quality [40, 41]
  - matched to a central medium quality track [40, 41] with $p_T > 25$ GeV
  - A-layer scintillator time $|t_A| < 10$ ns
  - $|\eta_{\rm det}| < 2$
  - isolated using the cuts $\sum_{\Delta R<0.5}(p_{T,\rm track}) < 3.5$ GeV and $\sum_{0.1<\Delta R<0.4}(E_T) < 2.5$ GeV
  - fires one of the single muon triggers to avoid the bias due to the triggers
- the probe muon must satisfy the following conditions:
  - has opposite charge to the tag
  - Δz(tag,probe) < 2 cm
- the invariant mass of the tag and the probe $M(\mu,\mu) > 50$ GeV. We also require $M(\mu,\mu) < 120$ GeV in the muonID and isolation efficiency measurements to limit background contamination.

Figure 4.3 shows the shapes of the invariant mass distributions for Run IIa and Run IIb.

4.3.3 Systematic uncertainty

The muon efficiency could be affected by the presence of background. The background may come from multijet events (the tag and the probe are from the jets), $W \to \mu\nu$ + jets (the tag is a high p_T muon, the probe is from the jets), and $Z \to \tau\tau$ (the tag is a high p_T muon from the τ, the probe is from a charged pion).

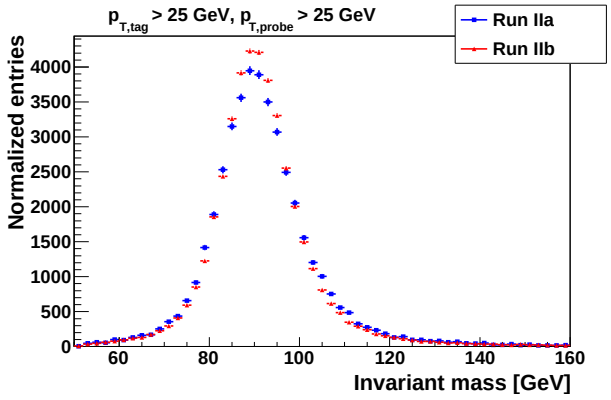

Figure 4.3: Dimuon invariant mass distributions for Run IIa (blue) and Run IIb (red)

To estimate the uncertainty due to the background, we vary some criteria that could change the contamination from the background:

- constraining the invariant mass ($|M_{\mu\mu} - 91.2| < 15$ GeV),
- requiring the tag and probe to be back-to-back ($\Delta\phi > 2.9$) to suppress $W \to \mu\nu$ events, and
- selecting dimuon events with no reconstructed jet to reduce the multijet background.

In addition, we also use the 0.2% uncertainty from the tag-and-probe method [41].

4.3.4 Muon identification efficiency

For the muon identification efficiency measurement, we estimate the probability for a muon to pass the mediumnseg3 quality requirements. Beside all criteria in Section 4.3.2, the following cuts are applied:

- the probe has a tight central track with $p_T > 25$ GeV
- the probe is isolated with the cuts $\sum_{\Delta R<0.5}(p_{T,\text{track}}) < 2.5$ GeV and $\sum_{0.1<\Delta R<0.4}(E_T) < 2.5$ GeV
- ΔR(tag,probe) > 2
- acollinearity $A > 0.05$, where $A = \pi - |\phi_{\text{tag}} - \phi_{\text{probe}}| + |\theta_{\text{tag}} - \theta_{\text{probe}}|$.

The muon-ID efficiency is the probability that the probe muon also passes the mediumnseg3 quality requirements described in Section 4.2.3. Figure 4.4 shows the mediumnseg3 muon-ID efficiency versus detector η and muon ϕ for data and MC.

The average muon-ID efficiencies are 74.8% (74.7%) for Run IIa data (Run IIb data). For Run IIb, the BC scintillator hit requirement is removed. The muon-ID efficiencies for MC are slightly different from those for data, 76.6% (77.0%) for Run IIa MC (Run IIb MC).

The ratio of the efficiencies, Data/MC, will be applied to MC muons to correct for the inaccuracy of the MC in Section 4.5.1. The ratio is estimated in detector η and muon ϕ with the binning:

- in muon detector η, we use 38 bins: $\{-2.1, -1.8, -1.7, -1.6, -1.5, -1.4, -1.3, -1.2, -1.1, -1, -0.9, -0.8, -0.7, -0.6, -0.5, -0.4, -0.3, -0.2, -0.1, 0, 0.1, 0.2, 0.3, 0.4, 0.5, 0.6, 0.7, 0.8, 0.9, 1, 1.1, 1.2, 1.3, 1.4, 1.5, 1.6, 1.7, 1.8, 2.1\}$
- in muon ϕ, we use 25 bins: $\{0, 0.098, 0.39, 0.68, 0.88, 1.17, 1.47, 1.66, 1.96, 2.25, 2.45, 2.74, 3.04, 3.23, 3.53, 3.82, 4.02, 4.31, 4.61, 4.81, 5.10, 5.39, 5.59, 5.89, 6.18, 6.28\}$

The average muon-ID correction factors are 0.976 for Run IIa and 0.970 for Run IIb. The systematic uncertainties on the muon-ID efficiencies and Data/MC scaling factors (SF) are summarized in Table 4.2.

Table 4.2: Summary of relative systematic uncertainties on muon-ID efficiencies and Data/MC scaling factors.

Source of systematic	Run IIa			Run IIb		
	Data	MC	Data/MC	Data	MC	Data/MC
Statistical uncertainty	0.21%	0.04%	0.22%	0.12%	0.07%	0.13%
$\lvert M_{\mu\mu} - 91.2\rvert < 15$ GeV	0.17%	0.09%	0.08%	0.01%	0.03%	0.02%
$\Delta\phi > 2.9$	0.43%	0.18%	0.24%	0.52%	0.21%	0.31%
Events with no jet	0.19%	0.19%	0.00%	0.49%	0.14%	0.35%
Tag and probe method	0.2%	0.2%	-	0.2%	0.2%	-
Total without stat.	0.54%	0.34%	0.26%	0.74%	0.32%	0.46%

4.3.5 Tracking efficiency

To measure the efficiency for a track to have tight track quality, we use all requirements in Section 4.3.2, except the Δz cut and the nCFT cut for the probe. We also apply the following requirements to selected $Z \to \mu\mu$ events:

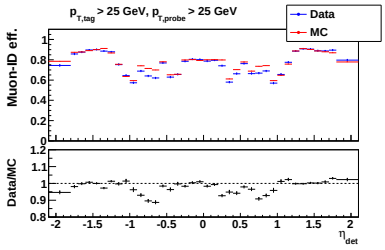

(a) MuonID efficiency versus detector η, Run IIa

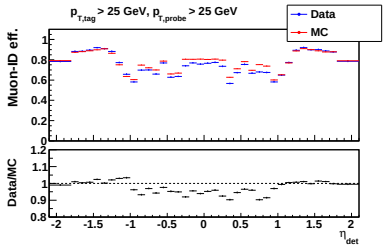

(b) MuonID efficiency versus detector η, Run IIb

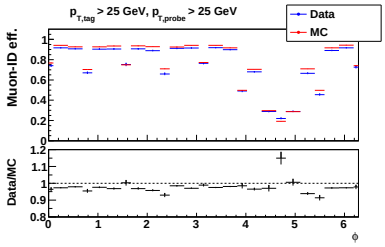

(c) MuonID efficiency versus muon ϕ, Run IIa

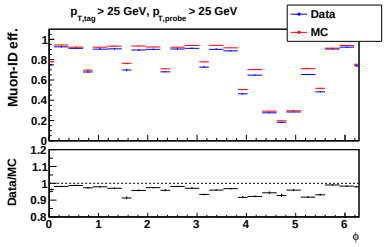

(d) MuonID efficiency versus muon ϕ, Run IIb

Figure 4.4: Muon identification efficiency versus (a,b) detector η, (c,d) muon ϕ for Run IIa and Run IIb.

- the probe has mediumnseg3 muon quality with $p_T > 25$ GeV
- the probe is isolated with the cuts $\sum_{\Delta R<0.5}(p_{T,\text{track}}) < 2.5$ GeV and $\sum_{0.1<\Delta R<0.4}(E_T) < 2.5$ GeV
- ΔR(tag,probe) > 2
- $|\Delta t_A|$(tag,probe) < 6 ns.

The tracking efficiency for tight tracks is the probability that the probe also passes the following requirements:

- nSMT > 1
- nCFT > 2
- $|dca| < 0.04$ cm
- $\frac{\chi^2}{dof} < 9.5$.

The tracking efficiency is affected by the single muon triggers. Some of the single muon triggers require a muon matching a track at the level 3 trigger. For Run IIb, due to the higher

luminosity, the trigger filters are tightened. Its tracking efficiency, therefore, becomes higher than that of Run IIa. Figure 4.5 shows the tracking efficiency for tight tracks in primary vertex (PV) z, $\eta_{\rm CFT}$, luminosity, and muon p_T for data and MC.

The average tracking efficiencies are 88.7% and 90.6% for Run IIa data and Run IIb data, respectively. The average MC tracking efficiencies are 89.2% (92.3%) for Run IIa MC (Run IIb MC). For correcting the simulated muon, the Data/MC scaling factor is calculated in PV z, $\eta_{\rm CFT}$, luminosity with the following binning:

- in PV z, we use 8 bins: $\{-60, -40, -15, -5, 0, 5, 15, 40, 60$ cm$\}$
- in $\eta_{\rm CFT}$, we use 36 bins: $\{-2.5, -1.8, -1.6, -1.5, -1.4, -1.3, -1.2, -1.1, -1, -0.9, -0.8, -0.7, -0.6, -0.5, -0.4, -0.3, -0.2, -0.1, 0, 0.1, 0.2, 0.3, 0.4, 0.5, 0.6, 0.7, 0.8, 0.9, 1, 1.1, 1.2, 1.3, 1.4, 1.5, 1.6, 1.8, 2.5\}$
- in luminosity, we use 5 bins: $\{0, 65, 100, 145, 190, 300$ $[10^{30}$ cm^{-2} s$^{-1}]\}$.

The average Data/MC scaling factors are 0.994 (0.982) for Run IIa (Run IIb). The systematic uncertainties on the tracking efficiencies and Data/MC scaling factors are summarized in Table 4.3.

Table 4.3: Summary of relative systematic uncertainties on tracking efficiencies and Data/MC scaling factors.

Source of systematic	Run IIa			Run IIb		
	Data	MC	Data/MC	Data	MC	Data/MC
Statistical uncertainty	0.17%	0.03%	0.17%	0.08%	0.04%	0.09%
$\lvert M_{\mu\mu} - 91.2\rvert < 15$ GeV	1.20%	0.69%	0.51%	1.38%	0.86%	0.52%
$\Delta\phi > 2.9$	0.08%	0.01%	0.07%	0.19%	0.05%	0.15%
Events with no jet	0.01%	0.11%	0.10%	0.03%	0.07%	0.04%
Tag and probe method	0.2%	0.2%	-	0.2%	0.2%	-
Total without stat.	1.22%	0.73%	0.53%	1.41%	0.89%	0.54%

4.3.6 Isolation efficiency

In the isolation efficiency measurement, we estimate the efficiency for a selected muon to pass the NPTight isolation requirements. The following requirements are applied in addition to all cuts but the isolation condition of the tag in Section 4.3.2:

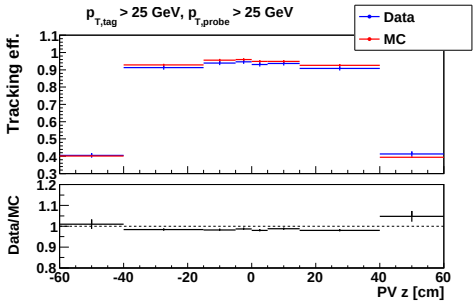

(a) Tracking efficiency versus PV z, Run IIa

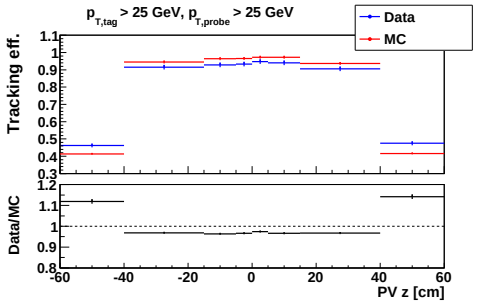

(b) Tracking efficiency versus PV z, Run IIb

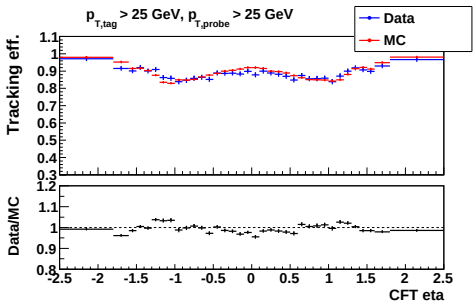

(c) Tracking efficiency versus η_{CFT}, Run IIa

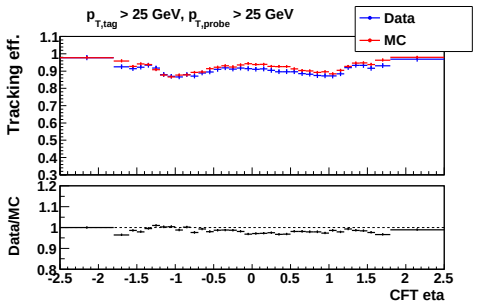

(d) Tracking efficiency versus η_{CFT}, Run IIb

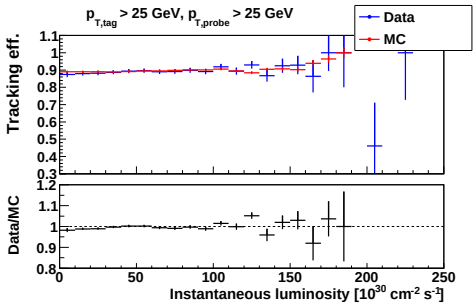

(e) Tracking efficiency versus luminosity, Run IIa

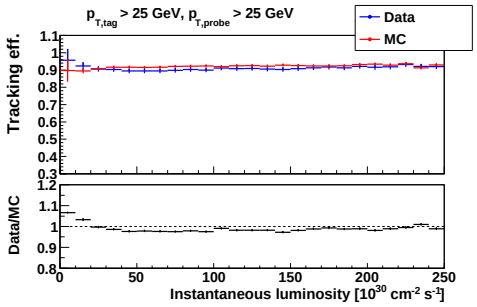

(f) Tracking efficiency versus luminosity, Run IIb

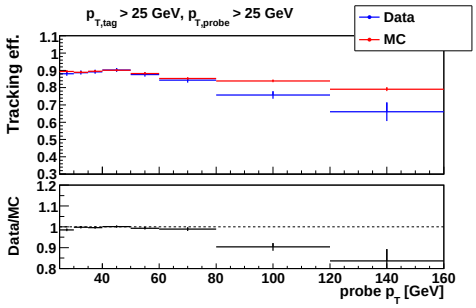

(g) Tracking efficiency versus muon p_T, Run IIa

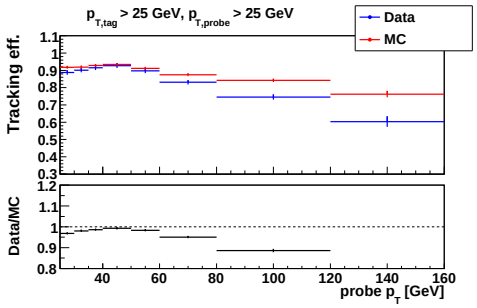

(h) Tracking efficiency versus muon p_T, Run IIb

Figure 4.5: Tracking efficiency versus (a,b) PV z, (c,d) η_{CFT}, (e,f) luminosity, and (g,h) muon p_T for Run IIa and Run IIb.

- the tag is isolated using the cuts $\sum_{\Delta R<0.5}(p_{T,\text{track}}) < 2.5$ GeV and $\sum_{0.1<\Delta R<0.4}(E_T) <$ 10 GeV.
- the probe muon passes the following requirements:
  - mediumnseg3 muon quality
  - tight track quality
  - $p_T > 25$ GeV
- acollinearity $A > 0.05$.

In this measurement, we relax the tag calorimeter isolation requirement to avoid any isolation bias from the tag [41]. The isolation efficiency is the probability that the probe muon passes the NPTight isolation requirements ($\sum_{\Delta R<0.5}(p_{T,\text{track}}) < 2.5$ GeV, $\sum_{0.1<\Delta R<0.4}(E_T) <$ 2.5 GeV) and the ΔR(probe,nearest jet) > 0.5.

Run IIb as mentioned before has high instantaneous luminosity. Therefore, it has more activity in the detector environment. The isolation efficiency consequently is reduced in Run IIb. Figure 4.6 shows the isolation efficiencies as functions of ΔR(probe,nearest jet), η_{CFT}, luminosity, and muon p_T.

The scaling factors for MC correction are applied in two steps, SF(ΔR)×SF(NPTight|ΔR). Where SF(ΔR) is the scaling factor for the ΔR isolation, and SF(NPTight|ΔR) is the scaling factor for the NPTight isolation given that the ΔR isolation is passed.

The SF(ΔR) are parametrized in luminosity and $|\eta_{\text{CFT}}|$ using the binning:

- in luminosity, we use 5 bins: {0, 65, 100, 145, 190, 300 [10^{30} cm^{-2} s^{-1}]}
- in $|\eta_{\text{CFT}}|$, we use 3 bins: {0, 1, 1.4, 2.5}.

The SF(NPTight|ΔR) is parametrized in $|\eta_{\text{CFT}}|$, muon p_T, and ΔR with the binning:

- in $|\eta_{\text{CFT}}|$, we use 3 bins: {0, 1, 1.5, 2.5}
- in muon p_T, we use 4 bins: {15, 25, 35, 45, 125 GeV}
- in ΔR, we use 5 bins: {0, 0.5, 1, 2.5, 10, 100}.

The average isolation efficiencies are 91.4% (85.4%) for Run IIa (Run IIb). They are 90.7% (85.5%) for Run IIa MC (Run IIb MC). The average Data/MC scaling factors are 1.01 (0.999) for Run IIa (Run IIb). The systematic uncertainty on the isolation efficiencies and scaling factors are presented in Table 4.4.

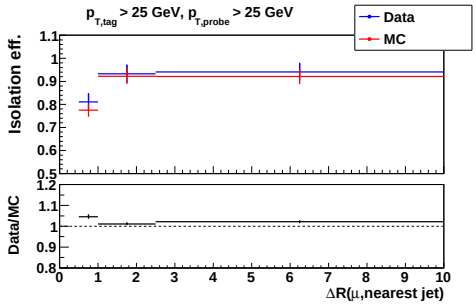

(a) Iso. efficiency versus $\Delta R(\mu, \text{nearest jet})$, Run IIa

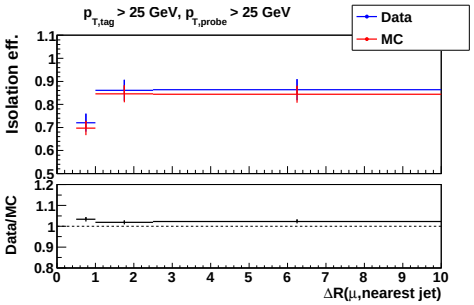

(b) Iso. efficiency versus $\Delta R(\mu, \text{nearest jet})$, Run IIb

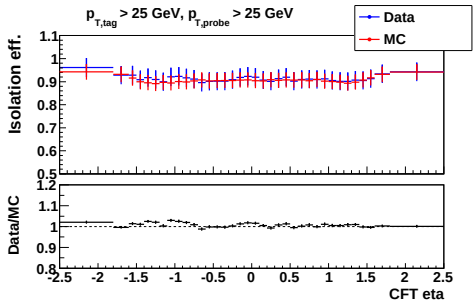

(c) Isolation efficiency versus η_{CFT}, Run IIa

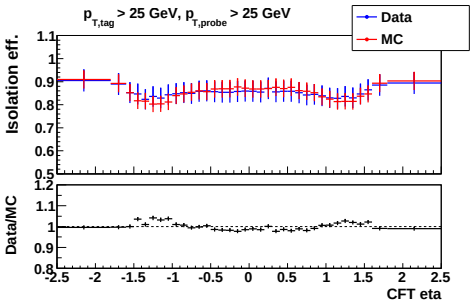

(d) Isolation efficiency versus η_{CFT}, Run IIb

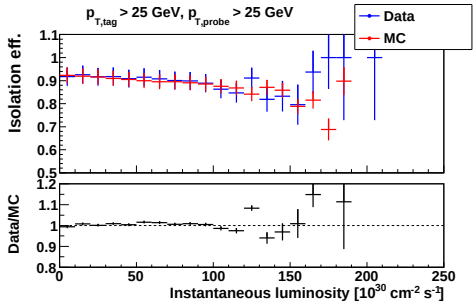

(e) Isolation efficiency versus luminosity, Run IIa

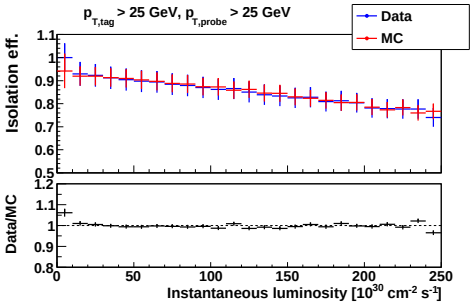

(f) Isolation efficiency versus luminosity, Run IIb

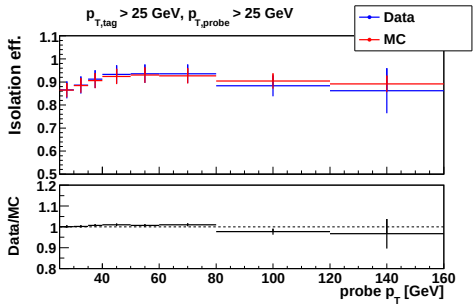

(g) Isolation efficiency versus muon p_T, Run IIa

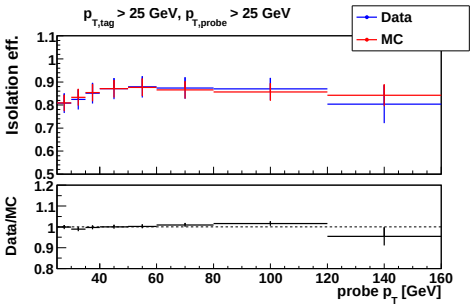

(h) Isolation efficiency versus muon p_T, Run IIb

Figure 4.6: Isolation efficiency versus (a,b) $\Delta R(\mu, \text{nearest jet})$, (c,d) η_{CFT}, (e,f) luminosity, and (g,h) muon p_T for Run IIa and Run IIb.

Table 4.4: Summary of relative systematic uncertainties on isolation efficiencies and Data/MC scaling factors.

Source of systematic	Run IIa			Run IIb		
	Data	MC	Data/MC	Data	MC	Data/MC
Statistical uncertainty	0.16%	0.03%	0.16%	0.11%	0.06%	0.12%
$\lvert M_{\mu\mu} - 91.2\rvert < 15$ GeV	0.40%	0.38%	0.03%	0.42%	0.40%	0.02%
$\Delta\phi > 2.9$	0.34%	0.05%	0.29%	0.07%	0.11%	0.04%
Events with no jet	4.18%	3.59%	0.59%	5.26%	4.32%	0.94%
Tag and probe method	0.2%	0.2%	-	0.2%	0.2%	-
Total without stat.	4.21%	3.62%	0.65%	5.28%	4.34%	0.94%

4.3.7 Single muon trigger efficiency

For the trigger efficiency, we measure the probability for a muon to pass all cuts in Section 4.2.3 except the trigger requirement, and to fire at least one of the the single muon triggers. To avoid the inefficiency from prescaled triggers, we require that the tag fires only unprescaled triggers [58]. After reconstructing $Z \to \mu\mu$ events using all requirements in Section 4.3.2 but the Δz cut, we add the following conditions to estimate the trigger efficiency:

- the probe muon passes the following requirements:
  - mediumnseg3 muon quality
  - tight track quality
  - $p_T > 25$ GeV
  - isolated with the cuts $\sum_{\Delta R<0.5}(p_{T,\text{track}}) < 2.5$ GeV and $\sum_{0.1<\Delta R<0.4}(E_T) < 2.5$ GeV
- ΔR(tag,probe) > 2
- acollinearity $A > 0.05$.

The trigger efficiency is the probability that the probe muon fires at least one of the single muon triggers listed in Section 4.2.2. The probe must match the fired trigger. Figure 4.7 shows the trigger efficiencies in η_{det}, phi, luminosity, and p_T. The figure shows that in comparison to Run IIa, the trigger filters of Run IIb are tighter, and the η_{det} coverage is reduced.

For MC, the trigger is not simulated. Therefore, we apply the trigger efficiency to MC in ϕ, η_{det}, and luminosity using the binning:

- in ϕ, we use 25 bins: {0, 0.1, 0.39, 0.69, 0.88, 1.19, 1.47, 1.67, 1.96, 2.26, 2.45, 2.75, 3.043, 3.24, 3.53, 3.83, 4.02, 4.32, 4.61, 4.81, 5.1, 5.4, 5.6, 5.89, 6.18, 6.28}
- in η_{det}, we use 20 bins: {−2.1, −1.8, −1.6, −1.4, −1.2, −1, −0.8, −0.6, −0.4, −0.2, 0, 0.2, 0.4, 0.6, 0.8, 1, 1.2, 1.4, 1.6, 1.8, 2.1}
- in luminosity, we use 6 bins: {0, 80, 100, 125, 160, 200, 400 [10^{30} cm^{-2} s^{-1}]}.

The average trigger efficiencies are 74.4% and 65.0% for Run IIa and Run IIb, respectively. The systematic uncertainties on trigger efficiency are summarized in Table 4.5.

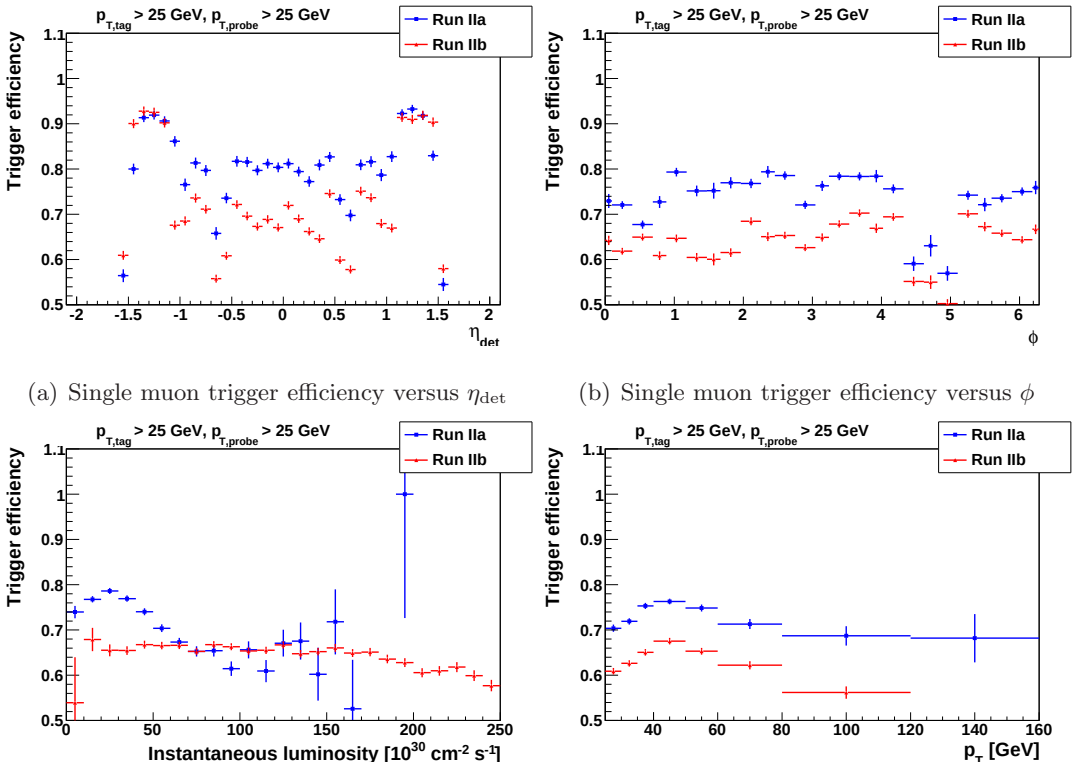

(a) Single muon trigger efficiency versus η_{det}

(b) Single muon trigger efficiency versus ϕ

(c) Single muon trigger efficiency versus luminosity

(d) Single muon trigger efficiency versus p_T

Figure 4.7: Single muon trigger efficiency versus (a) η_{det}, (b) ϕ, (c) luminosity, and (d) p_T for Run IIa (blue) and Run IIb (red).

Table 4.5: Summary of relative systematic uncertainties on trigger efficiencies for Run IIa and Run IIb.

Source of systematic	Run IIa	Run IIb
Statistical uncertainty	0.25%	0.17%
$\lvert M_{\mu\mu} - 91.2\rvert < 15$ GeV	0.66%	1.01%
$\Delta\phi > 2.9$	0.07%	0.09%
Events with no jet	0.21%	0.02%
Tag and probe method	0.2%	0.2%
Total without stat.	0.72%	1.03%

4.3.8 Total muon efficiency

Total muon certification efficiency is the product of the individual efficiencies,

$$\varepsilon = \varepsilon_{\text{muon-ID}} \times \varepsilon_{\text{tracking}} \times \varepsilon_{\text{trigger}} \times \varepsilon_{\text{isolation}} \tag{4.1}$$

where ε is the total muon efficiency, $\varepsilon_{\text{muon-ID}}$ is the muon identification efficiency, $\varepsilon_{\text{tracking}}$ is the tracking efficiency, $\varepsilon_{\text{trigger}}$ is the single muon trigger efficiency, and $\varepsilon_{\text{isolation}}$ is the isolation efficiency.

Figure 4.8 shows the total efficiency in physics η, muon p_T, and luminosity. The average total efficiencies are 45.0% and 37.6% for Run IIa and Run IIb, respectively. Table 4.6 summaries the systematic uncertainties on total muon efficiency for Run IIa and Run IIb.

Table 4.6: Summary of relative systematic uncertainties on muon efficiencies for Run IIa and Run IIb.

Source of systematic	Run IIa	Run IIb
Statistical uncertainty	0.41%	0.24%
$\lvert M_{\mu\mu} - 91.2\rvert < 15$ GeV	2.10%	2.84%
$\Delta\phi > 2.9$	0.78%	0.88%
Events with no jet	4.15%	5.78%
Tag and probe method	0.2%	0.2%
Total without stat.	4.72%	6.51%

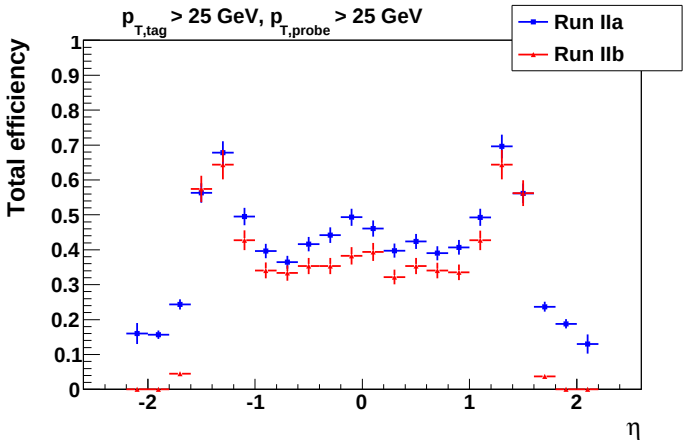

(a) Total muon efficiency versus η

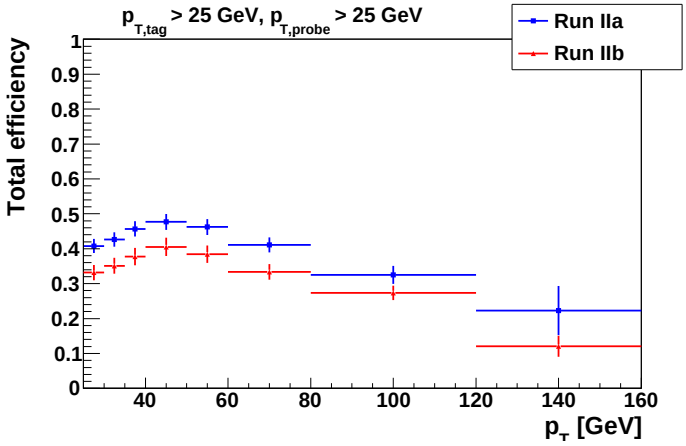

(b) Total muon efficiency versus p_T

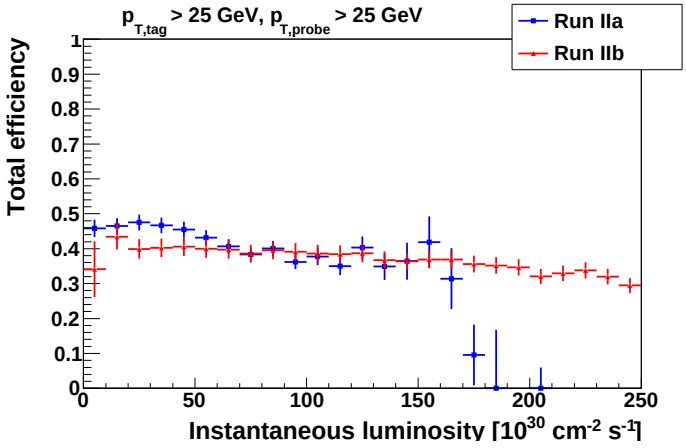

(c) Total muon efficiency versus luminosity

Figure 4.8: Total muon efficiency versus (a) η, (b) p_T, and (c) luminosity for Run IIa (blue) and Run IIb (red).

4.3.9 Ratio $k = \epsilon^+/\epsilon^-$ for $W \to \mu\nu$ events

In $p\overline{p}$ collisions, the W^+ and W^- in general are boosted in opposite directions. As a result, the transverse momentum spectra of the positive and negative muons are different in a given pseudorapidity bin as shown in Figure 4.9. The spectra in this figure are plotted using the PYTHIA MC generator-level. In the η bin $(-2, -1.7)$, the negative muon p_T distribution (red) is shifted to higher p_T, while the positive muon p_T distribution is lower. The reverse trend is shown in the bin (1.7,2). The difference is gradually reduced for smaller $|\eta|$ bins. In the central region, $0 < |\eta| < 0.2$, the two spectra are nearly identical.

As we can see in Figure 4.8, the total muon efficiency depends on η, p_T, and luminosity. Therefore, the average total efficiency of the positive muons (ϵ^+) in a given η bin is not identical to that of negative muons (ϵ^-).

We use the p_T distributions from data and the data total efficiency to estimate ϵ^+ and ϵ^-. The total efficiency is folded into the p_T distributions of the positive and negative muons separately. The total efficiency is parametrized in physics η, p_T, and luminosity using the following binning:

- in physics η, we use 20 bins: {−2.0, −1.8, −1.6, −1.4, −1.2, −1.0, −0.8, −0.6, −0.4, −0.2, 0, 0.2, 0.4, 0.6, 0.8, 1.0, 1.2, 1.4, 1.6, 1.8, 2.0}
- in p_T, we use 9 bins: {20, 25, 30, 35, 40, 50, 60, 80, 120, 160 GeV}
- in luminosity, we use 5 bins: {0, 65, 100, 145, 190, 300 [10^{30} cm^{-2} s^{-1}]}.

In each physics η bin, the average efficiency is calculated as $\epsilon^{\pm} = \frac{\sum \epsilon_i}{N^{\pm}}$, where ϵ_i is the tag-and-probe total efficiency of event i, and $N^{\pm}$ is the total number of positive (negative) events in the bin.

Figure 4.10 shows the relative efficiency correction, $k = \epsilon^+/\epsilon^-$, for Run IIa and Run IIb. The difference between the ϵ^+ and ϵ^- becomes larger at high $|\eta|$ bins due to the difference in their p_T distributions. We vary the total efficiency from the tag-and-probe method by one standard deviation to estimate the systematic uncertainty on k.

4.4 Charge misidentification

The muon charge asymmetry is diluted by misidentification of the muon charge. The charge misidentification (charge misID) probability is the probability that a muon's charge

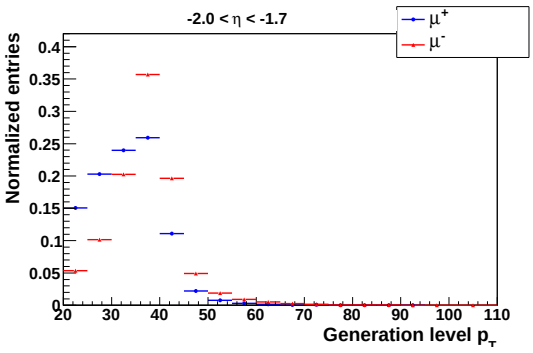

(a) $-2 < \eta < -1.7$

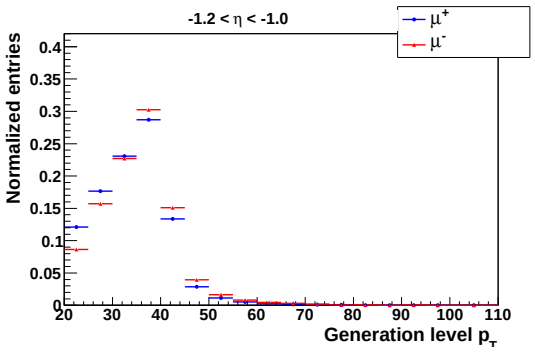

(b) $-1.2 < \eta < -1$

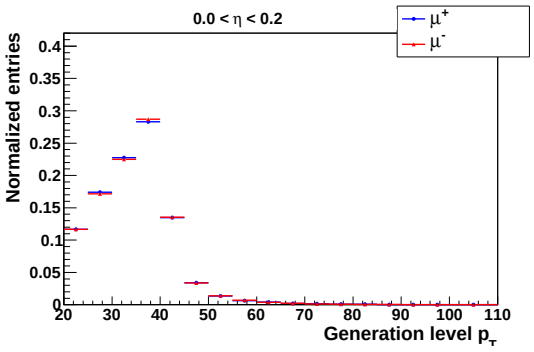

(c) $0 < \eta < 0.2$

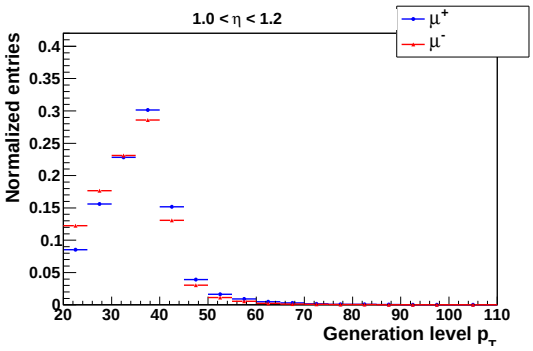

(d) $1 < \eta < 1.2$

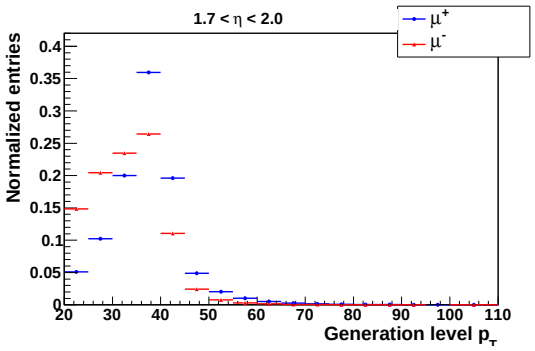

(e) $1.7 < \eta < 2$

Figure 4.9: MC truth p_T distributions of positive (blue) and negative (red) muons in the physics η bins: $-2 < \eta < -1.7$, $-1.2 < \eta < -1$, $0 < \eta < 0.2$, $1 < \eta < 1.2$, and $1.7 < \eta < 2$.

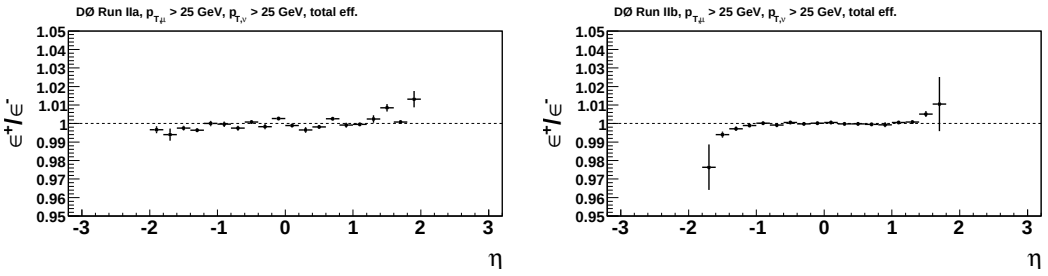

(a) Run IIa (b) Run IIb

Figure 4.10: Ratios of the positive and negative muon efficiencies for (a) Run IIa and (b) Run IIb.

is misidentified as the opposite sign. We use the tag-and-probe method with the same requirements as in the tracking efficiency measurement to estimate the muon charge misID probability. We also require that the probe has a tight central track and fires at least one of the single muon triggers listed in Section 4.2.2.

The charge misID probability (g) is the ratio of the number of events with same sign tag-and-probe muons to the total number of probes. The tracking system measures the charge of muons very well. There are only 19 (27) same signed events in 18,954 (52,200) tag-probes for Run IIa (Run IIb). On average, the muon charge misID is 0.1% (0.05%) for Run IIa (Run IIb). Figure 4.12 shows the muon charge misID probability as a function of physics η and p_T for Run IIa and Run IIb.

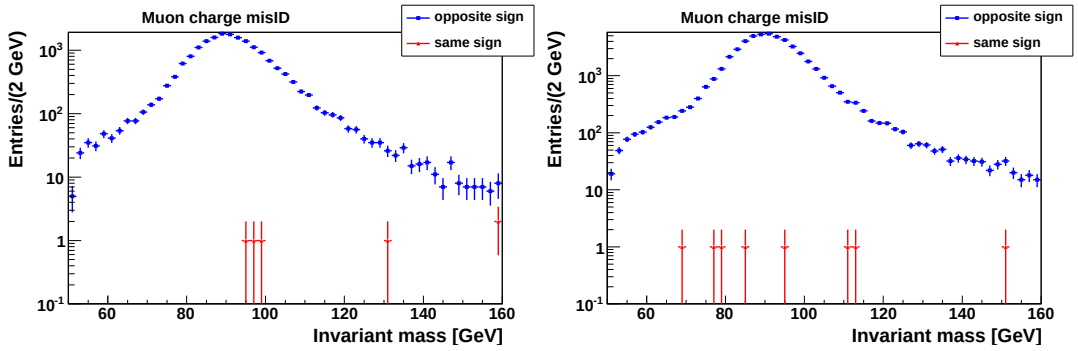

(a) Run IIa (b) Run IIb

Figure 4.11: Invariant mass distributions of opposite sign muons (blue) and same sign muons (red).

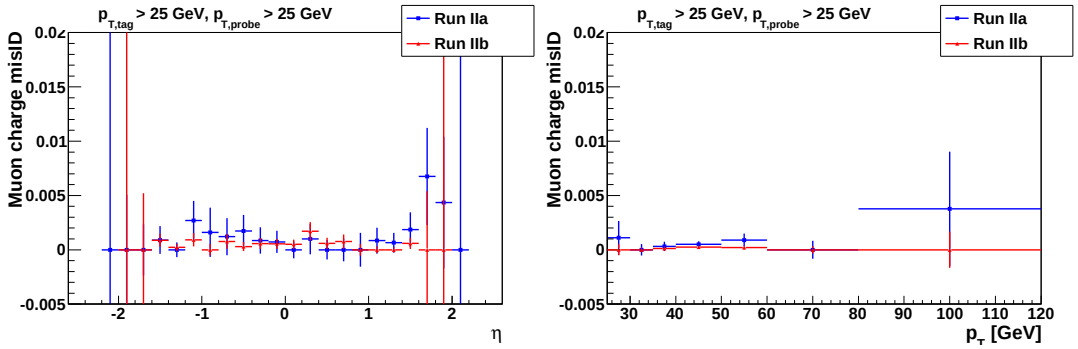

(a) Muon charge misid versus η

(b) Muon charge misid versus p_T

Figure 4.12: Muon charge misidentification probability as a function of (a) physics η and (b) p_T for Run IIa (blue) and Run IIb (red).

4.5 Backgrounds

The main backgrounds in the analysis are due to electroweak processes and multijet events. The electroweak background is due to the processes $W \to \tau\nu$, $Z/\gamma \to \mu\mu$, and $Z/\gamma \to \tau\tau$. The multijet background comes primarily from semileptonic heavy flavor decays.

4.5.1 Electroweak background

The electroweak (EW) background is due to the processes $Z/\gamma \to \mu\mu$, where one of the muons is mis-reconstructed, and $W \to \tau\nu$ and $Z/\gamma \to \tau\tau$, where a tau lepton decay includes a muon.

The EW background is estimated using PYTHIA MC samples following the same procedure as was used to reconstruct the $W \to \mu\nu$ signal. The MC sample names are CSG_CAF_MCv4–ReqID_p18.13.01 for Run IIa and CSG_CAF_MCv4–ReqID_p21.11.00 for Run IIb. Request-IDs and numbers of events of the samples are listed in Table 4.7.

The momenta of MC muons are smeared to have similar resolution in the data and MC. The MC samples are corrected for the luminosity profile and the beam shape of data. We also apply the muon-ID, tracking, and isolation Data/MC scaling factors as well as the trigger efficiency to the MC to take into account the difference in the efficiencies for Data and MC. The scaling factors and trigger efficiency are calculated in Section 4.3.

The MC samples are then normalized to have the same luminosities as the data, 1.08

fb^{-1} and 6.22 fb^{-1} for Run IIa and Run IIb, respectively. Table 4.8 shows the cross sections used to normalize the MC in next-to-next-to-leading-order (NNLO).

Table 4.7: PYTHIA MC request-IDs and numbers of events.

Processes	request-IDs	number of events
Run IIa		
$W \to \mu\nu$	125272 $\to$ 125311	7,722,335
$W \to \tau\nu$	37646 $\to$ 37650, 39231 $\to$ 39245	3,900,417
$Z \to \mu\mu$ ($15 < m_{\mu\mu} < 60$ GeV)	36591 $\to$ 36595, 40678 $\to$ 40687	2,999,418
$Z \to \mu\mu$ ($60 < m_{\mu\mu} < 130$ GeV)	38899 $\to$ 38912, 42047 $\to$ 42053	3,836,694
$Z \to \mu\mu$ ($130 < m_{\mu\mu} < 250$ GeV)	35709, 41252	504,091
$Z \to \mu\mu$ ($250 < m_{\mu\mu} < 500$ GeV)	35714, 41256	151,473
$Z \to \mu\mu$ ($m_{\mu\mu} > 500$ GeV)	35717, 41259	75,428
$Z \to \tau\tau$ ($15 < m_{\tau\tau} < 60$ GeV)	36596 $\to$ 36600, 40688 $\to$ 40697	2,980,304
$Z \to \tau\tau$ ($60 < m_{\tau\tau} < 130$ GeV)	37782 $\to$ 37791, 39216 $\to$ 39230	5,031,341
$Z \to \tau\tau$ ($130 < m_{\tau\tau} < 250$ GeV)	35711, 41254	499,329
$Z \to \tau\tau$ ($250 < m_{\tau\tau} < 500$ GeV)	35715, 41257	150,069
$Z \to \tau\tau$ ($m_{\tau\tau} > 500$ GeV)	35718, 41258	81,864
Run IIb		
$W \to \mu\nu$	132152 $\to$ 132191	7,189,759
$W \to \tau\nu$	89232 $\to$ 89236, 89617 $\to$ 89626	2,693,866
$Z \to \mu\mu$ ($15 < m_{\mu\mu} < 60$ GeV)	75077 $\to$ 75081	999,378
$Z \to \mu\mu$ ($60 < m_{\mu\mu} < 130$ GeV)	75087 $\to$ 75089, 86872 $\to$ 86876	1,499,154
$Z \to \mu\mu$ ($130 < m_{\mu\mu} < 250$ GeV)	75092, 75093	292,503
$Z \to \mu\mu$ ($250 < m_{\mu\mu} < 500$ GeV)	75095, 75096	339,066
$Z \to \mu\mu$ ($m_{\mu\mu} > 500$ GeV)	75098, 75099	299,545
$Z \to \tau\tau$ ($15 < m_{\tau\tau} < 60$ GeV)	65717 $\to$ 65721	999,604
$Z \to \tau\tau$ ($60 < m_{\tau\tau} < 130$ GeV)	66012, 66032, 66033, 66052, 66072, 86909 $\to$ 86913	1,972,509
$Z \to \tau\tau$ ($130 < m_{\tau\tau} < 250$ GeV)	66373, 86908	442,527
$Z \to \tau\tau$ ($250 < m_{\tau\tau} < 500$ GeV)	66375	194,173
$Z \to \tau\tau$ ($m_{\tau\tau} > 500$ GeV)	66377	102,103

Table 4.8: Cross sections used to normalize MC samples [61]

	σ(NNLO) [pb]
$W \to \ell\nu$	2719.1
Z ($15 < m_{\ell\ell} < 60$ GeV)	512.6
Z ($60 < m_{\ell\ell} < 130$ GeV)	257.6
Z ($130 < m_{\ell\ell} < 250$ GeV)	1.875
Z ($m_{\ell\ell} > 250$ GeV)	0.1536

The systematic uncertainty in the electroweak background is estimated from the uncertainties on the cross section, 3.5% [61], and the integrated luminosity, 6.1% [64]. The electroweak background is estimated separately for each η and p_T bin. The contributions of the electroweak background in all p_T bins are shown in Table 4.10.

4.5.2 Multijet background

To estimate the multijet (MJ) background, we fit the MC signal and all backgrounds to the selected data in transverse mass using the template fit method. The MJ background is found from the non-isolation region where the multijet background is the highest component. We also assume that the shape of the MJ background in the non-isolation region is the same as in the isolation region (the signal region).

A MJ model (M_{MJ}) is derived from data. We select single muon events as in Section 4.2.3, except for the isolation requirements. Then the selected muons are required to be non-isolated with the total transverse momentum of tracks surrounding the muon in a cone of $R = 0.5$ (EtTrkCone) above 2.5 GeV. No calorimeter isolation (EtHalo) requirement is applied. We choose EtTrkCone instead of the EtHalo because it depends less on the geometry of the detector than the EtHalo.

The contaminations from the $W \to \mu\nu$ and EW events in the non-isolation region are estimated from MC. We subtract the MC $W \to \mu\nu$ and EW events passing the anti-isolation requirement from the anti-isolated data events. Figure 4.13 shows the contribution of the $W \to \mu\nu$ and EW contamination in M_T for the non-isolated data events.

For creating a MC model (M_{MC}), we add the isolated EW background to the isolated MC signal. The shapes of the isolated MC model and the MJ model are compared in Figure 4.14.

The models of signal and backgrounds are fitted to data using RooFit [62] to find the expected numbers of signal and backgrounds. The numbers of events are constrained as a function of M_T as

$$M_D(M_T) = \left(\frac{N_{MC}}{N_{MC} + N_{MJ}}\right) M_{MC}(M_T) + \left(\frac{N_{MJ}}{N_{MC} + N_{MJ}}\right) M_{MJ}(M_T) \qquad (4.2)$$

where N_{MJ} is the number of MJ background events, and N_{MC} is the sum of MC signal and electroweak background. M_D is the transverse mass shape of the observed isolated data

events. M_{MC} is the MC model constructed from the MC signal and EW samples. M_{MJ} is the MJ background model.

The shape of the M_T distribution and the number of events are then constrained in the extended likelihood formalism:

$$-\log L = -\sum_{\text{data}} \log M_D - \log \mathcal{P}(N_{\text{expected}}, N_D) \tag{4.3}$$

where $N_{\text{expected}} = N_{MC} + N_{MJ}$, and N_D is the number of isolated data events in a M_T bin. $\mathcal{P}$ is the Poisson probability.

N_{MC} and N_{MJ} are found from the minimized $-\log$(likelihood) performed by MINUIT [63]. The fit is done in the range $50 < M_T < 100$ GeV with two free parameters, N_{MC} and N_{MJ}. The expected normalization values are found separately for Run IIa and Run IIb.

Finally, scaling factors, $SF_{MJ} = N_{MJ}/N_{\text{anti-iso}}$ and $SF_{MC} = N_{MC}/N_{MC,0}$, are used to normalize the non-isolated data events and isolated MC samples, where $N_{\text{anti-iso}}$ and $N_{MC,0}$ are the initial numbers of the non-isolated data events and isolated MC events in the fit range.

The fit results for Run IIa and Run IIb are shown in Table 4.9 and Figure 4.15. In this figure, the solid blue line is the fit template. The dashed blue line is the normalized MC component and the dashed red line is the normalized multijet component, and the black dots show the data. The bottom window shows the χ of data with respect to the fit template curve.

Table 4.9: Outputs of the template fit.

	N_{MC}	N_{MJ}	correlation	SF_{MC}	SF_{MJ}	χ^2/dof (MC+MJ,data)
Run 2a	499351	16788	-0.967	0.962	0.166	2.41
Run 2b	2087242	50761	-0.960	0.962	0.129	3.30

We do not set any upper limit for M_T in the muon charge asymmetry measurement. The fit range is limited, however, because the PYTHIA MC does not simulate the data well at high M_T. The ratio data to MC increases significantly for $M_T > 100$ GeV, Figure 4.16.

Figure 4.17 displays MJ/MJ$_0$, where MJ$_0$ is the default MJ background and MJ is the

MJ background for different fit ranges. The discrepancy between MJ_0 and MJ(50–90 GeV) is about 30%.

The disagreement between data and MC for $M_T > 100$ GeV primarily comes from the MC signal. We re-weight the MC signal to the ratio (Data − backgrounds)/MC in M_T to study the MJ background with the maximum fit range higher than 100 GeV. Figure 4.18 shows MJ/MJ_0 after re-weighting the MC signal. The difference between MJ_0 and MJ(50–200 GeV) is about 4%.

The anti-isolated events are chosen with the EtTrkCone requirement and without the EtHalo requirement. EtTrkCone is less sensitive to the geometry of the calorimeter than EtHalo. In addition, MC signal matches the data better in EtTrkCone than in EtHalo. We also do the fit using the EtHalo requirement and with both isolation requirements. The M_T shapes of the anti-isolated events with different isolation requirements are shown in Figure 4.19. Figure 4.20 shows MJ/MJ_0 with different EtTrkCone and EtHalo cuts: EtTrkCone > 2.5 GeV, EtTrkCone > 5 GeV, EtHalo > 2.5 GeV, EtHalo > 5 GeV, EtTrkCone > 2.5 GeV and EtHalo > 2.5 GeV, EtTrkCone > 5 GeV and EtHalo > 5 GeV. The difference between MJ and MJ_0 is within 6%.

The MC signal and EW background are subtracted from the anti-isolated data events. Therefore, the MJ shape also depends on the precision of the MC anti-isolation sample. We vary the MC by a scaling factor m from 0.8 to 1.2 to study the dependence of the MJ background on the MJ shape. Figure 4.21 shows that the discrepancy between MJ(m) and MJ_0 is less than 1%.

The default bin size of the M_T distribution is 1 GeV. The fit is also done with different bin sizes: 0.5 GeV, 2 GeV, and 5 GeV. Figure 4.22 shows that $\Delta MJ/MJ_0$ is about 1%.

In summary, the MJ background depends most strongly on the fit range. This is the main component of the systematic uncertainty of the MJ background. The systematic uncertainty assigned to the MJ background is 30%.

4.5.3 Total background

The contributions from the MJ and EW backgrounds are listed in Table 4.10. The values are presented as percentages of the selected events. The EW background contributes 7.2% of the selected events, and the MJ background contributes 3.2%. Figures 4.23 and 4.24

show the M_T, $\not\!\!E_T$, p_T, Wp_T, and η distributions of data, backgrounds, and the MC signal in linear and logarithmic scales. The MC does not match well to data in Wp_T or physics η.

To make sure that the disagreement between data and MC is not due to mismeasured efficiencies, we compare data and MC for $Z \to \mu\mu$ events (see Appendix B). The data and MC dimuon events match reasonably well in muon η_{det} and ϕ. Therefore, the discrepancy for $W \to \mu\nu$ is primarily from the mismodeling of the MC samples. However, we do not use the MC signal directly in the asymmetry calculation, and the contributions of the MJ and EW backgrounds are small.

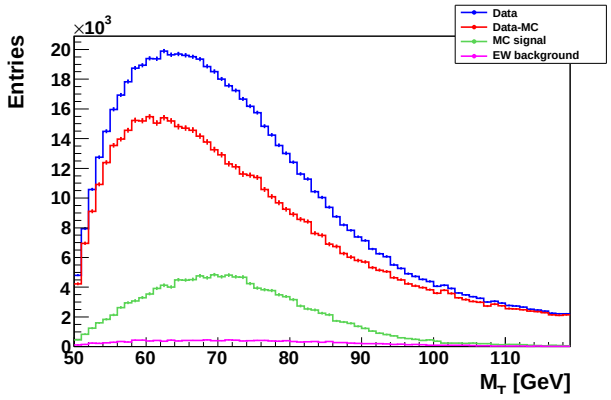

Figure 4.13: M_T distributions of the anti-isolated events.

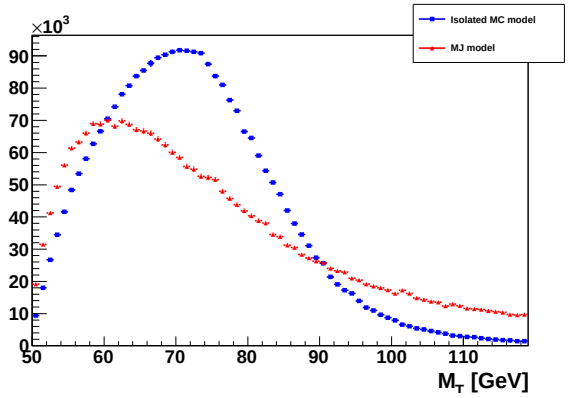

Figure 4.14: Shapes of the isolated MC model and the MJ model determined from the non-isolated events.

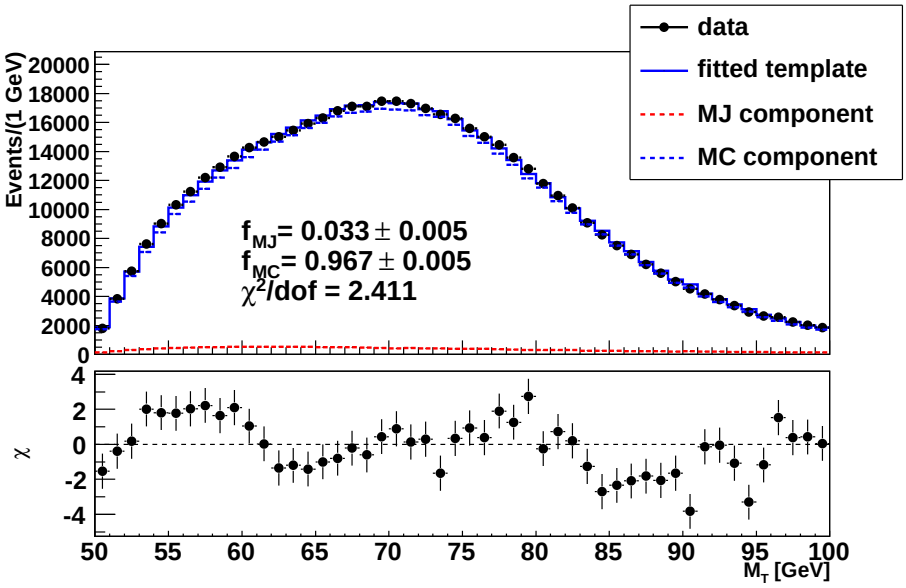

(a) Run IIa

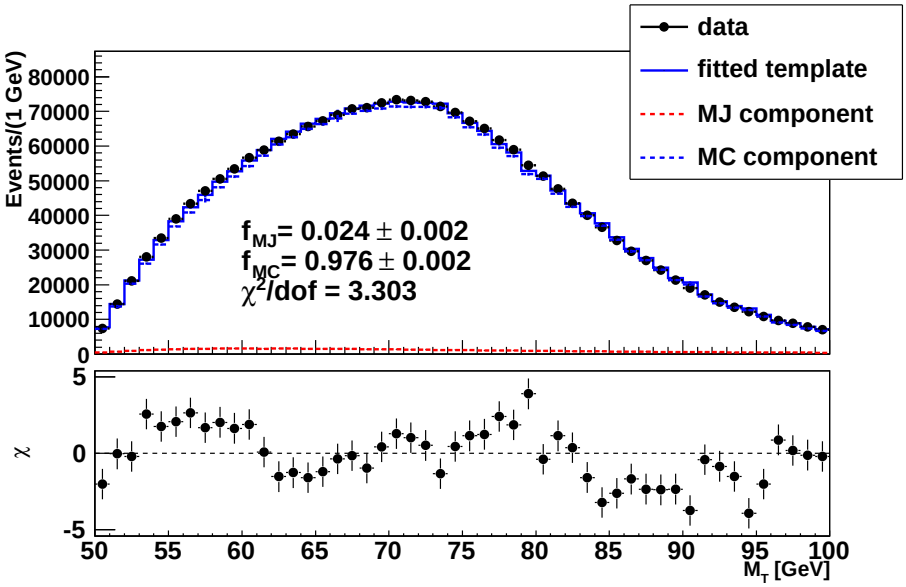

(b) Run IIb

Figure 4.15: Outputs of the template fit in M_T for Run IIa and Run IIb. The bottom windows show the chi of data w.r.t. the template fit curve, $\chi = \frac{N_D - N_{\text{expected}}}{\sqrt{N_D}}$.

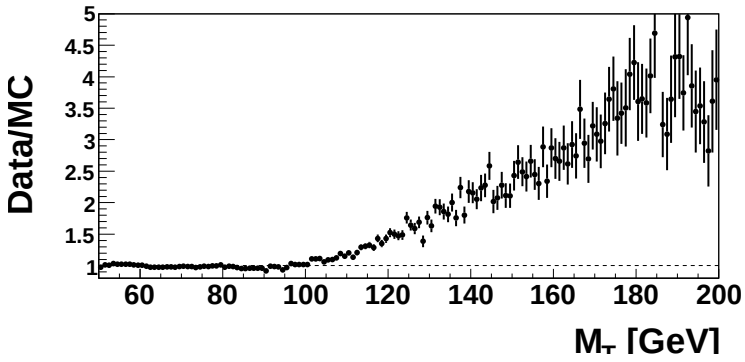

Figure 4.16: Ratio of data to MC.

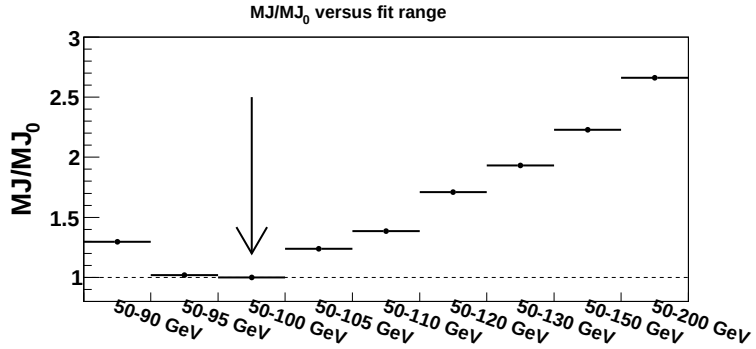

Figure 4.17: MJ/MJ_0 versus fit range. The arrow points to the fit range used.

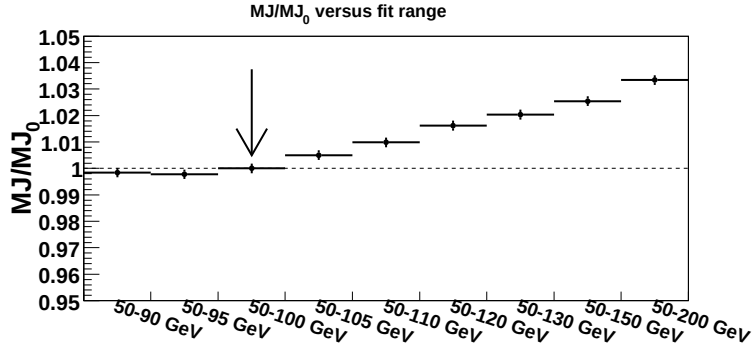

Figure 4.18: MJ/MJ_0 versus fit range. The MC signal is re-weighted to the ratio, (Data-backgrounds)/MC, to eliminate the disagreement between data and MC at high M_T. The arrow points to the fit range used.

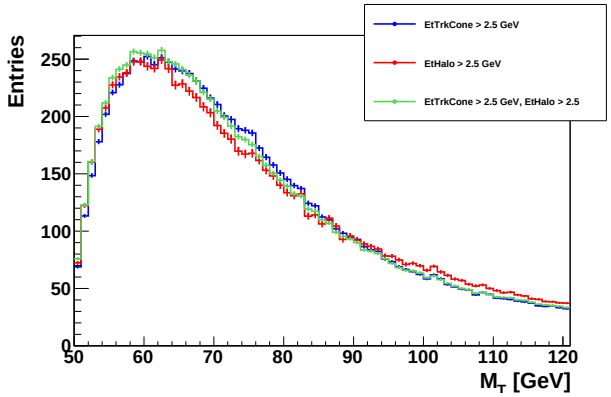

Figure 4.19: M_T shapes of the non-isolated data events with different anti-isolation requirements. The non-isolated $W \to \mu\nu$ and EW events are subtracted from the data.

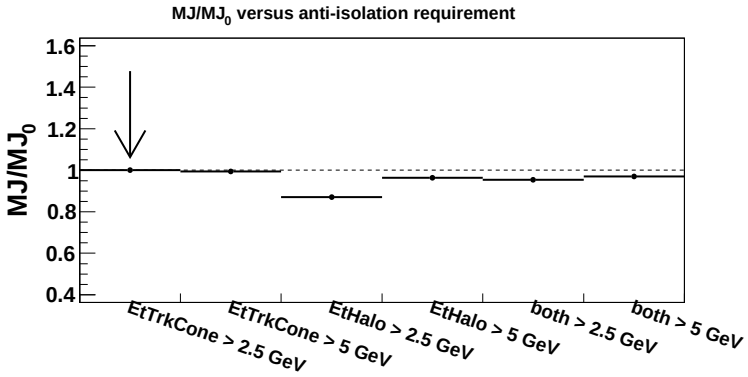

Figure 4.20: $\mathrm{MJ/MJ_0}$ versus anti-isolation requirement. The arrow indicates the cut used.

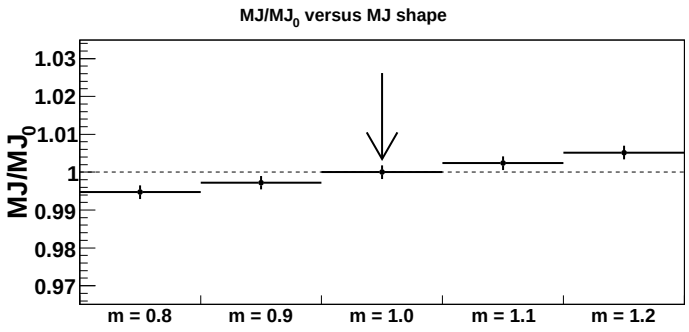

Figure 4.21: $\mathrm{MJ/MJ_0}$ versus MJ shape. The arrow indicates the default scaling factor m.

Table 4.10: Contributions of the multijet background and the electroweak backgrounds to the selected events. The values are given as percentages of the selected events.

	percent background ± stat ± sys
$p_T > 25$ GeV, $\not\!\!E_T > 25$ GeV	
Multijet background	3.224 ± 0.011 ± 0.967
$W \to \tau\nu$	1.639 ± 0.008 ± 0.115
$Z/\gamma \to \mu\mu$	5.453 ± 0.014 ± 0.382
$Z/\gamma \to \tau\tau$	0.092 ± 0.002 ± 0.006
$25 < p_T < 35$ GeV, $\not\!\!E_T > 25$ GeV	
Multijet background	3.936 ± 0.018 ± 1.181
$W \to \tau\nu$	3.036 ± 0.016 ± 0.213
$Z/\gamma \to \mu\mu$	4.486 ± 0.020 ± 0.314
$Z/\gamma \to \tau\tau$	0.123 ± 0.003 ± 0.009
$p_T > 35$ GeV, $\not\!\!E_T > 25$ GeV	
Multijet background	2.731 ± 0.013 ± 0.819
$W \to \tau\nu$	0.673 ± 0.006 ± 0.047
$Z/\gamma \to \mu\mu$	6.122 ± 0.019 ± 0.429
$Z/\gamma \to \tau\tau$	0.070 ± 0.002 ± 0.005
$25 < p_T < 35$ GeV, $25 < \not\!\!E_T < 35$ GeV	
Multijet background	2.642 ± 0.018 ± 0.793
$W \to \tau\nu$	3.468 ± 0.021 ± 0.243
$Z/\gamma \to \mu\mu$	4.600 ± 0.024 ± 0.322
$Z/\gamma \to \tau\tau$	0.140 ± 0.004 ± 0.010
$p_T > 35$ GeV, $\not\!\!E_T > 35$ GeV	
Multijet background	3.088 ± 0.016 ± 0.926
$W \to \tau\nu$	0.509 ± 0.007 ± 0.036
$Z/\gamma \to \mu\mu$	6.189 ± 0.023 ± 0.433
$Z/\gamma \to \tau\tau$	0.040 ± 0.002 ± 0.003

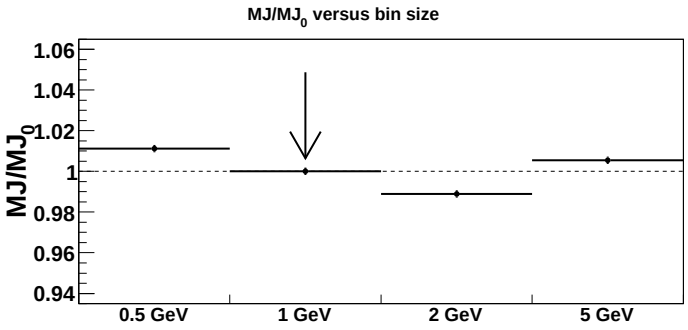

Figure 4.22: MJ/MJ$_0$ versus bin size. The arrow indicates the default bin size.

4.6 Muon charge asymmetry

4.6.1 Calculating the muon charge asymmetry

The muon charge asymmetry is calculated as

$$A = \frac{N_\mu^+ - N_\mu^-}{N_\mu^+ + N_\mu^-}, \tag{4.4}$$

where N_μ^+ and N_μ^- are the true numbers of positive and negative muons from $W \to \mu\nu$ events. Determining the true numbers of positive and negative muon events requires taking not only the backgrounds into account, but also the overall signal efficiency and the muon charge misidentification probability.

In terms of the true numbers of muon events from $W \to \mu\nu$ events, after background subtraction, the observed number of muon events is

$$N^+ = \varepsilon^+(1-g)N_\mu^+ + \varepsilon^- g N_\mu^- \tag{4.5}$$

$$N^- = \varepsilon^-(1-g)N_\mu^- + \varepsilon^+ g N_\mu^+ \tag{4.6}$$

where N^+ (N^-) is the number of observed positive (negative) $W \to \mu\nu$ events, ε^+ (ε^-) is the total signal efficiency of positive (negative) muons, and g is the charge misID probability. $N^\pm$ can also be written as

$$N^\pm = N^\pm_{\text{data}} - N^\pm_{\text{EW}} - N^\pm_{\text{MJ}}, \tag{4.7}$$

where $N^\pm_{\text{data}}$ is the number of selected muons, $N^\pm_{\text{EW}}$ is the number of muons from electroweak backgrounds, and $N^\pm_{\text{MJ}}$ is the number of muons from multijet background.

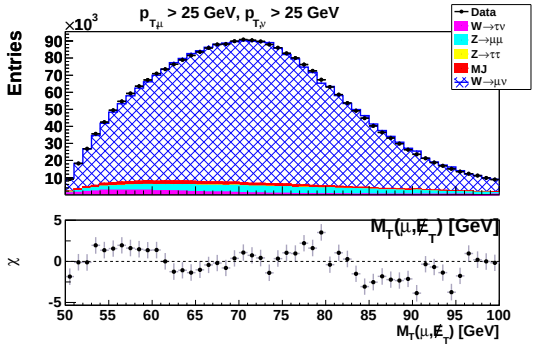

(a) Transverse mass distribution

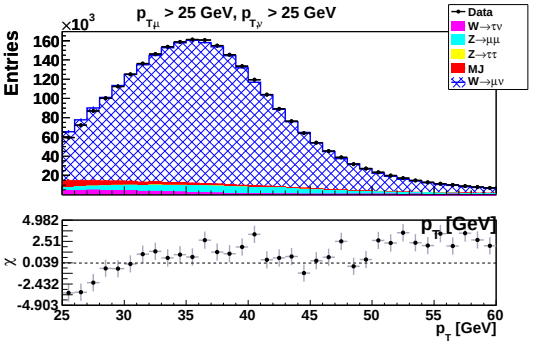

(b) Muon transverse momentum

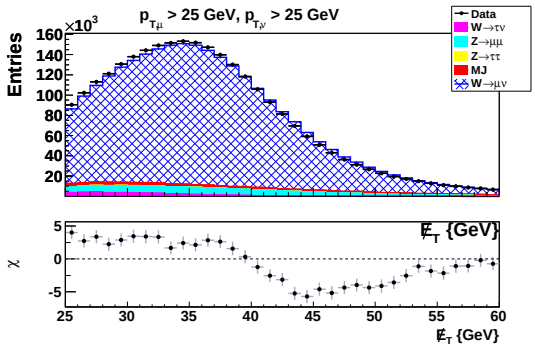

(c) Missing transverse energy

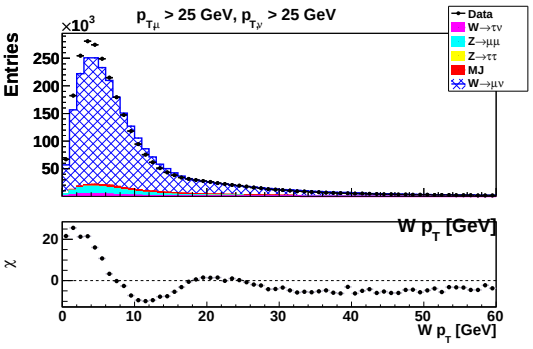

(d) W transverse momentum

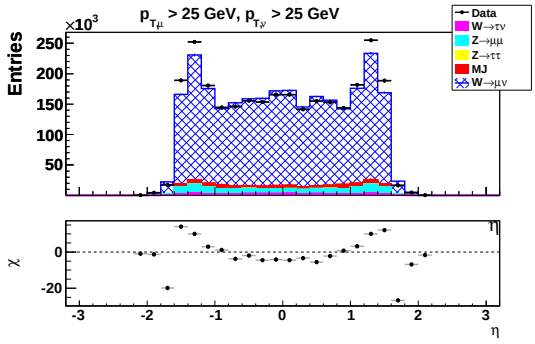

(e) physics η

Figure 4.23: Stacked distributions of M_T, p_T, $\not{E}_T$, W p_T, and physics η of data (black dots), multijet background (red), and electroweak backgrounds from Monte Carlo, $W \to \tau\nu$ (pink), $Z \to \mu\mu$ (cyan), $Z \to \tau\tau$ (yellow), and MC signal $W \to \mu\nu$ (hatched blue) for $p_T > 25$ GeV and $\not{E}_T > 25$ GeV. The bottom windows display the χ of data w.r.t the total MC, where $\chi = \frac{N_{\text{data}} - N_{\text{MC}}}{\sqrt{\Delta N^2_{\text{data}} + \Delta N^2_{\text{MC}}}}$. We do not use the MC signal in the asymmetry calculation.

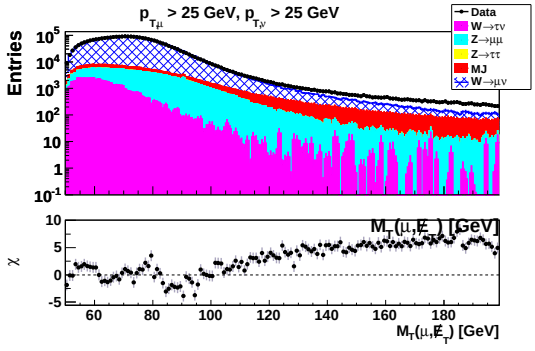

(a) Transverse mass distribution

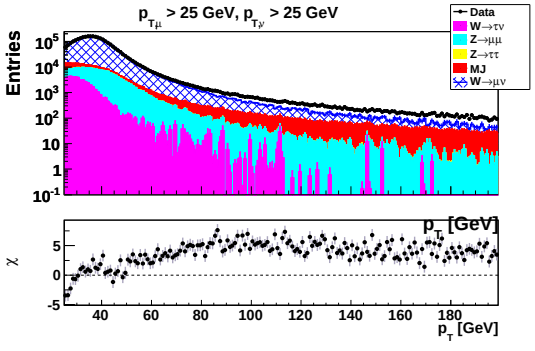

(b) Muon transverse momentum

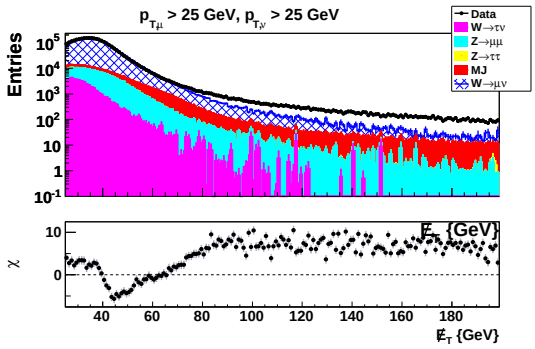

(c) Missing transverse energy

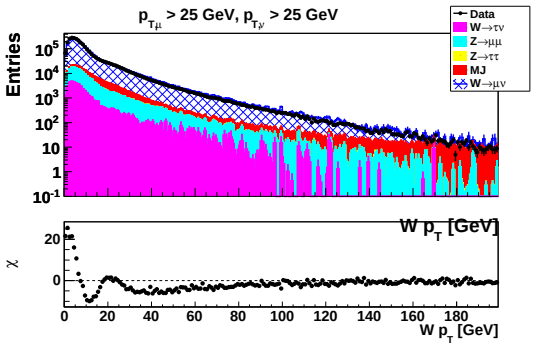

(d) W transverse momentum

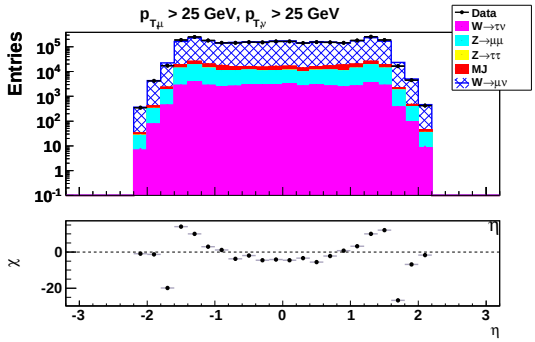

(e) physics η

Figure 4.24: Stacked distributions of M_T, p_T, $\not{E}_T$, W p_T, and physics η of data (black dots), multijet background (red), and electroweak backgrounds from Monte Carlo, $W \to \tau\nu$ (pink), $Z \to \mu\mu$ (cyan), $Z \to \tau\tau$ (yellow), and MC signal $W \to \mu\nu$ (hatched blue) for $p_T > 25$ GeV and $\not{E}_T > 25$ GeV. The bottom windows display the χ of data w.r.t. the total MC, where $\chi = \frac{N_{\text{data}} - N_{\text{MC}}}{\sqrt{\Delta N^2_{\text{data}} + \Delta N^2_{\text{MC}}}}$. We do not use the MC signal in the asymmetry calculation.

The linear Eqs. (4.5) and (4.6) can be expressed as,

$$\begin{bmatrix} N^+ \\ N^- \end{bmatrix} = \begin{bmatrix} \varepsilon^+(1-g) & \varepsilon^- g \\ \varepsilon^+ g & \varepsilon^-(1-g) \end{bmatrix} \begin{bmatrix} N_\mu^+ \\ N_\mu^- \end{bmatrix} \tag{4.8}$$

$$\Rightarrow \qquad N_\mu^+ = \frac{\begin{vmatrix} N^+ & \varepsilon^- g \\ N^- & \varepsilon^-(1-g) \end{vmatrix}}{\begin{vmatrix} \varepsilon^+(1-g) & \varepsilon^- g \\ \varepsilon^+ g & \varepsilon^-(1-g) \end{vmatrix}} = \frac{\varepsilon^-(1-g)N^+ - \varepsilon^- g N^-}{\varepsilon^+\varepsilon^-(1-g)^2 - \varepsilon^+\varepsilon^- g^2} \tag{4.9}$$

$$N_\mu^- = \frac{\begin{vmatrix} \varepsilon^+(1-g) & N^+ \\ \varepsilon^+ g & N^- \end{vmatrix}}{\begin{vmatrix} \varepsilon^+(1-g) & \varepsilon^- g \\ \varepsilon^+ g & \varepsilon^-(1-g) \end{vmatrix}} = \frac{\varepsilon^+(1-g)N^- - \varepsilon^+ g N^+}{\varepsilon^+\varepsilon^-(1-g)^2 - \varepsilon^+\varepsilon^- g^2} \tag{4.10}$$

Plugging Eqs. (4.9) and (4.10) into (4.4), we have:

$$A = \frac{[\varepsilon^-(1-g)N^+ - \varepsilon^- g N^-] - [\varepsilon^+(1-g)N^- - \varepsilon^+ g N^+]}{[\varepsilon^-(1-g)N^+ - \varepsilon^- g N^-] + [\varepsilon^+(1-g)N^- - \varepsilon^+ g N^+]} \tag{4.11}$$

$$A = \frac{[\varepsilon^-(1-g) + \varepsilon^+ g]N^+ - [\varepsilon^+(1-g) + \varepsilon^- g]N^-}{[\varepsilon^-(1-g) - \varepsilon^+ g]N^+ + [\varepsilon^+(1-g) - \varepsilon^- g]N^-} \tag{4.12}$$

Seting $k = \varepsilon^+/\varepsilon^-$, Eq. (4.12) becomes:

$$A = \frac{(1-g+kg)N^+ - (k-kg+g)N^-}{(1-g-kg)N^+ + (k-kg-g)N^-}. \tag{4.13}$$

The systematic uncertainty on A is a quadrature sum of the partial uncertainties of all parameters. The partial uncertainties from $N_{\rm EW}$, $N_{\rm MJ}$, g, and k are calculated as

$$\Delta A(N_{\rm EW}) = \Delta N_{\rm EW} \frac{2k(1-2g)[(N^+_{\rm data} - N^+_{\rm MJ})N^-_{\rm EW} - (N^-_{\rm data} - N^-_{\rm MJ})N^+_{\rm EW}]}{[(1-g-kg)(N^+_{\rm data} - N^+_{\rm EW} - N^+_{\rm MJ}) + (k-kg-g)(N^-_{\rm data} - N^-_{\rm EW} - N^-_{\rm MJ})]^2 N_{\rm EW}} \tag{4.14}$$

$$\Delta A(N_{\rm MJ}) = \Delta N_{\rm MJ} \frac{2k(1-2g)[(N^+_{\rm data} - N^+_{\rm EW})N^-_{\rm MJ} - (N^-_{\rm data} - N^-_{\rm EW})N^+_{\rm MJ}]}{[(1-g-kg)(N^+_{\rm data} - N^+_{\rm EW} - N^+_{\rm MJ}) + (k-kg-g)(N^-_{\rm data} - N^-_{\rm EW} - N^-_{\rm MJ})]^2 N_{\rm MJ}} \tag{4.15}$$

$$\Delta A(g) = \Delta g \frac{2k(N^{+2} - N^{-2})}{[(1-g-kg)(N^+_{\rm data} - N^+_{\rm EW} - N^+_{\rm MJ}) + (k-kg-g)(N^-_{\rm data} - N^-_{\rm EW} - N^-_{\rm MJ})]^2} \tag{4.16}$$

$$\Delta A(k) = \Delta k \frac{2[(1-g)N^+ - gN^-][gN^+ - (1-g)N^-]}{[(1-g-kg)(N^+_{\rm data} - N^+_{\rm EW} - N^+_{\rm MJ}) + (k-kg-g)(N^-_{\rm data} - N^-_{\rm EW} - N^-_{\rm MJ})]^2} \tag{4.17}$$

where $\Delta N_{\rm EW}$, $\Delta N_{\rm MJ}$, Δg, and Δk are the total uncertainties on the corresponding parameters (see Appendix C for more detail).

4.6.2 Measuring the muon charge asymmetry

We measure the muon charge asymmetry for $|\eta| < 2$ for Run IIa ($|\eta| < 1.6$ for Run IIb) with the following η bin edges:
$\{-2.0, -1.8, -1.6, -1.4, -1.2, -1.0, -0.8, -0.6, -0.4, -0.2, 0, 0.2, 0.4, 0.6, 0.8, 1.0, 1.2, 1.4, 1.6, 1.8, 2.0\}$.

The muon charge asymmetry is calculated separately (within each η bin) using equation (4.13) for five sets of data with the following kinematic cuts:

1. $p_T^\mu > 25$ GeV, $\not\!\!E_T > 25$ GeV,
2. $25 < p_T^\mu < 35$ GeV, $\not\!\!E_T > 25$ GeV,
3. $p_T^\mu > 35$ GeV, $\not\!\!E_T > 25$ GeV,
4. $25 < p_T^\mu < 35$ GeV, $25 < \not\!\!E_T < 35$ GeV,
5. $p_T^\mu > 35$ GeV, $\not\!\!E_T > 35$ GeV.

The first three sets have $\not\!\!E_T > 25$ GeV, and the last two sets have symmetric cuts for p_T^μ and $\not\!\!E_T$.

In this measurement, the backgrounds, g, and k are measured independently in each η and p_T bin. The backgrounds are subtracted bin by bin. Results after further corrections for all five kinematic bins are presented in Sections 4.6.6 to 4.6.10.

4.6.3 Effect of magnet polarities

In this section, we study the effect of the magnet polarities on the muon charge asymmetry. In the DØ detector, the central tracking system lies inside a 2 T solenoid. The solenoid polarity is flipped frequently to avoid any asymmetry from the detector. However, if there is an offset in the track curvature and the portions of data in each solenoid polarity are not identical, the effect will not be canceled out.

We separate the selected events by solenoid polarity to check for bias. Muon charge asymmetries for forward and backward solenoid polarities are then calculated separately without any corrections for Run IIa and Run IIb. Figure 4.25 compares the shapes of the muon p_T distributions of positive muons (μ^+) to negative muons (μ^-). The ratios μ^+/μ^- in the bottom windows of Figure 4.25 show that for forward solenoid, the momenta

of the positive muons are smaller than those of negative muons at p_T less than 35 GeV, and higher than the negative muon momenta at high p_T. The reverse trend happens for backward solenoid. Consequently, the asymmetry with forward solenoid is higher than the asymmetry with backward solenoid at low p_T, and it becomes lower at high p_T as shown in Figure 4.26. We also see that individual run epochs show different amounts of offset. Each epoch of data has a slightly different tracking geometry due to opening and closing the detector.

We use PYTHIA MC to test that an offset in the track curvature could cause the observed shifts. To simulate the effect of forward solenoid (positive curvature offset), a small trial curvature offset, 0.00025, is added to $1/p_T$ of positive sign tracks and subtracted from negative sign tracks. For backward solenoid (negative curvature offset), exactly the same method is used except the signs are flipped. Figure 4.27 shows that this method can reproduce the overall shifts. It also confirms that if there are exactly identical amounts of positive offset and negative offset, the bias in the asymmetry due to the solenoid would be averaged out.

In this measurement, we correct this effect by weighting the data so that all epochs have 25% of their luminosity in each polarity combination (solenoid and toroid polarities althought little or no effect is seen with toroid polarity). Tables 4.11 lists the contribution of each polarity combination and the corresponding scaling factor in each epoch. Then the scaled asymmetry ($A_{\rm scl}$) is calculated from the numbers of weighted events using equation 4.13. The systematic uncertainty on the correction is estimated from the non-inelastic partial uncertainty of the integrated luminosity, 2.8% [64]. Figure 4.28 shows the difference of the asymmetries before and after polarity weighting. The maximum shift due to the polarity weighting is about 0.005 (0.002) for Run IIa (Run IIb).

4.6.4 Detector p_T and $\not\!\!E_T$ smearing correction

When the muon and the recoil jet (recoil) go through the detector, their momenta are smeared out. Consequently, the muon momentum and the $\not\!\!E_T$ at the detector level are not the same as the momenta of the muon and the neutrino when they were produced. To compare the measured muon charge asymmetry to the theory prediction, we correct the asymmetry for the smearing of the muon p_T and the $\not\!\!E_T$ due to the DØ detector.

Table 4.11: Percent of luminosity of data and the corresponding scaling factors (SF) in each polarity combination for data-taking epochs. s_f is the forward solenoid, s_b is the backward solenoid, t_f is the forward toroid, and t_b is the backward toroid.

Epoch	Lumi (pb^{-1})	$s_f t_f$		$s_b t_f$		$s_f t_b$		$s_b t_b$	
		% lumi	SF	% lumi	SF	% lumi	SF	% lumi	SF
Run IIa1	53.16	31.36	0.797	18.05	1.385	26.34	0.949	24.25	1.031
Run IIa2	118.32	21.18	1.180	34.76	0.719	23.25	1.075	20.81	1.201
Run IIa3	78.15	32.19	0.777	26.93	0.928	19.22	1.301	21.66	1.154
Run IIa4	827.58	25.25	0.990	28.08	0.890	24.73	1.011	21.94	1.139
Run IIb1	1221.13	21.54	1.161	24.66	1.014	27.23	0.918	26.57	0.941
Run IIb2	3054.51	28.55	0.876	21.91	1.141	23.9	1.046	25.64	0.975
Run IIb3	1976.53	19.46	1.185	26.65	0.938	28.28	0.884	25.71	0.972

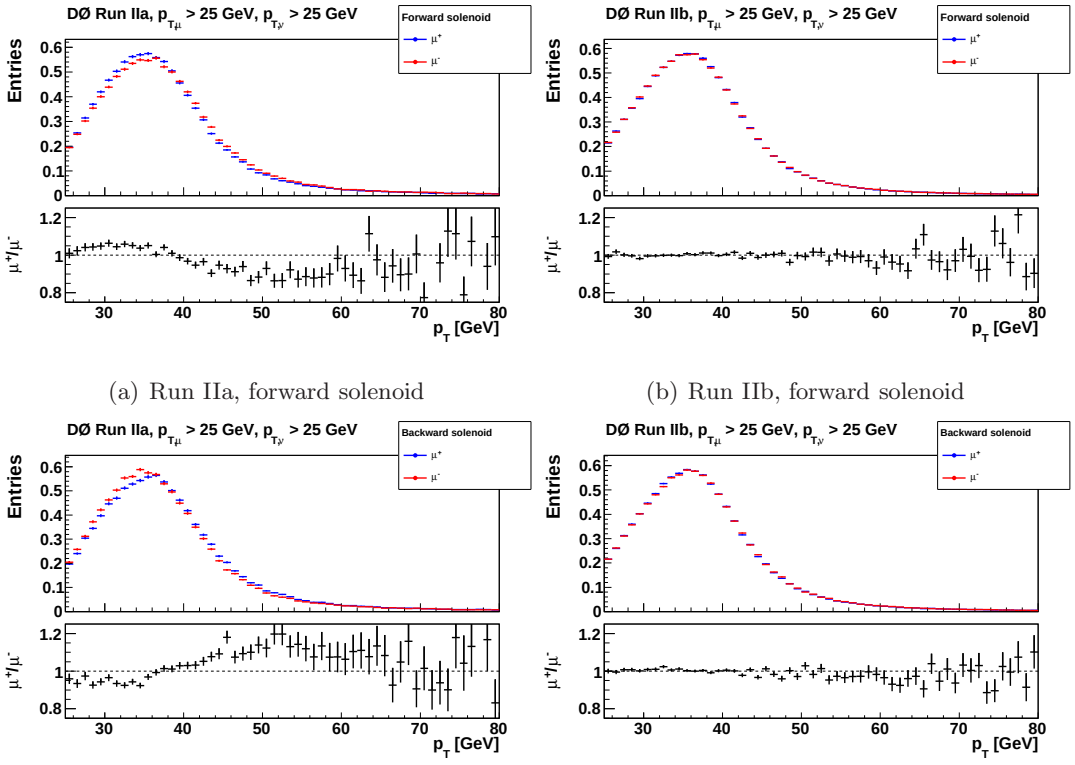

(a) Run IIa, forward solenoid

(b) Run IIb, forward solenoid

(c) Run IIa, backward solenoid

(d) Run IIb, backward solenoid

Figure 4.25: Comparison of muon p_T distributions of positive muons (blue) and negative muons (red) for Run IIa and Run IIb. The bottom windows show the ratio μ^+/μ^-. Entries are normalized by area.

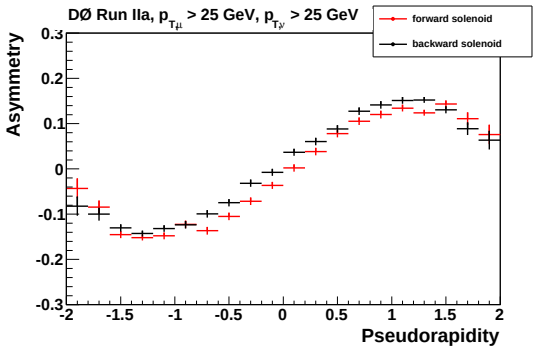

(a) Run IIa, $p_T > 25$ GeV, $\not\!\!E_T > 25$ GeV

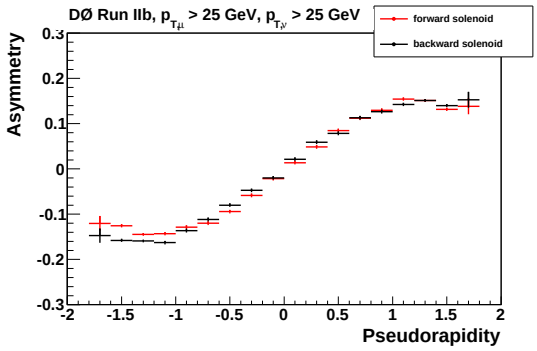

(b) Run IIb, $p_T > 25$ GeV, $\not\!\!E_T > 25$ GeV

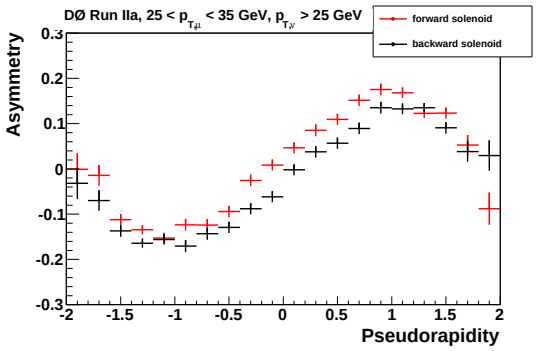

(c) Run IIa, $25 < p_T < 35$ GeV, $\not\!\!E_T > 25$ GeV

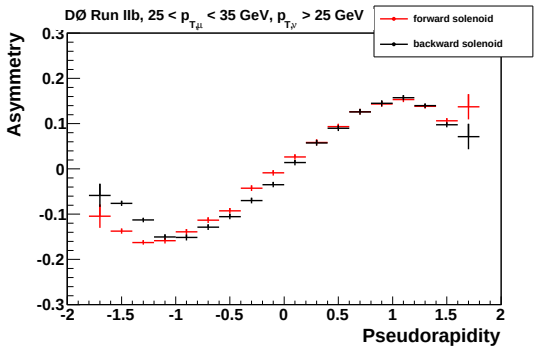

(d) Run IIb, $25 < p_T < 35$ GeV, $\not\!\!E_T > 25$ GeV

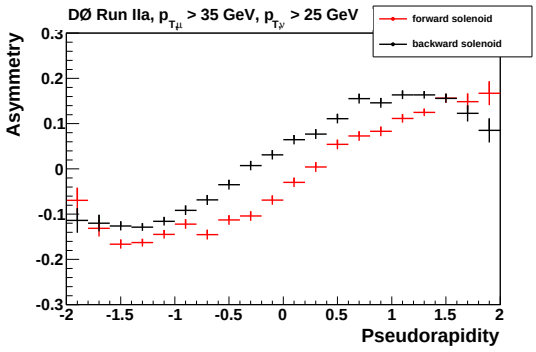

(e) Run IIa, $p_T > 35$ GeV, $\not\!\!E_T > 25$ GeV

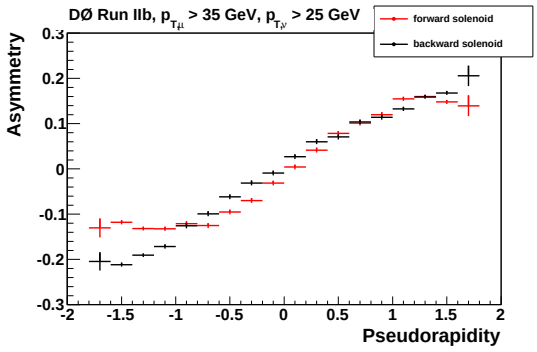

(f) Run IIb, $p_T > 35$ GeV, $\not\!\!E_T > 25$ GeV

Figure 4.26: Comparison of muon charge asymmetry for forward solenoid (blue) and reverse solenoid (red) for Run IIa and Run IIb.

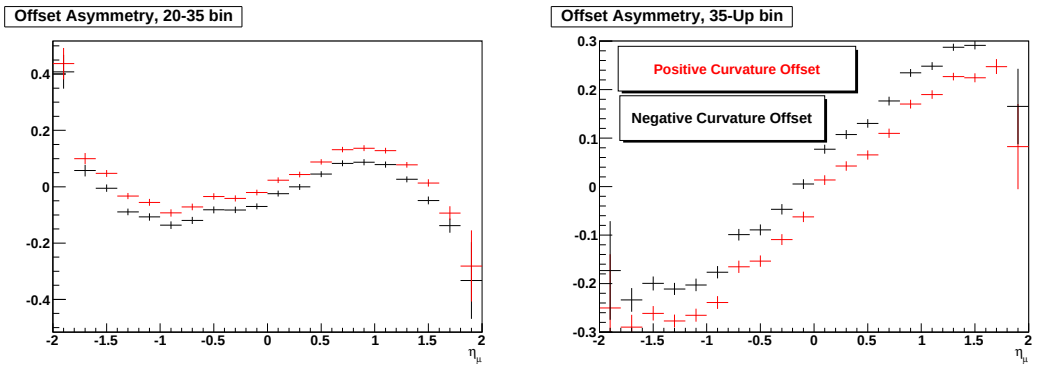

(a) $20 < p_T < 35$ GeV, $\not\!\!E_T > 20$ GeV

(b) $p_T > 35$ GeV, $\not\!\!E_T > 20$ GeV

Figure 4.27: Comparison of muon charge asymmetry with forward solenoid (positive curvature offset in red) and reverse solenoid (negative curvature offset in black) for MC events.

We use a MC $W \to \mu\nu$ sample generated by RESBOS with the CTEQ6.6 PDF set to estimate the smearing correction. The muon p_T at the generator level is smeared to have the same momentum resolution as data

$$\frac{q}{p_T} \to (1+S)\frac{q}{p_T} + G_1\left(A \oplus \frac{B\sqrt{\cosh\eta}}{p_T}\right) \tag{4.18}$$

where q is the charge of the muon, p_T is the truth muon p_T, and G_1 is a Gaussian random number with mean 0 and rms 1. S accounts for the difference in momentum scale between data and MC. The smearing parameter A corresponds to the detector hit resolution, and parameter B is for the multiple scattering effect. The values of A, B, and S for Run IIa and Run IIb are presented in Table 4.12.

Table 4.12: Muon momentum smearing parameters [67].

	A	B	S
Run IIa	0.0025 ± 0.0002	0.023 ± 0.002	0.0046 ± 0.021
Run IIb	0.0023 ± 0.0001	0.025 ± 0.002	0.0053 ± 0.017

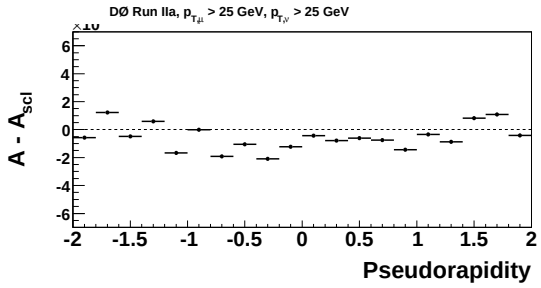

(a) Run IIa, $p_T > 25$ GeV, $\not\!\!E_T > 25$ GeV

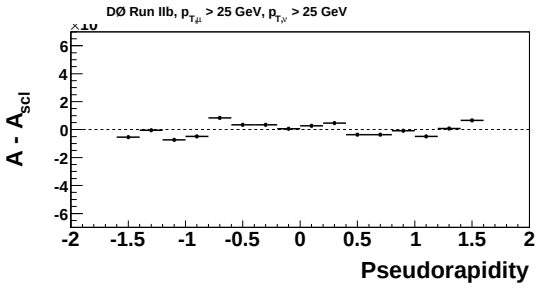

(b) Run IIb, $p_T > 25$ GeV, $\not\!\!E_T > 25$ GeV

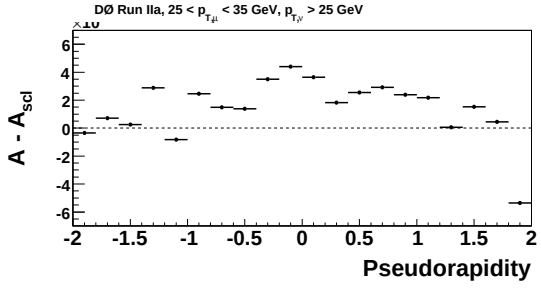

(c) Run IIa, $25 < p_T < 35$ GeV, $\not\!\!E_T > 25$ GeV

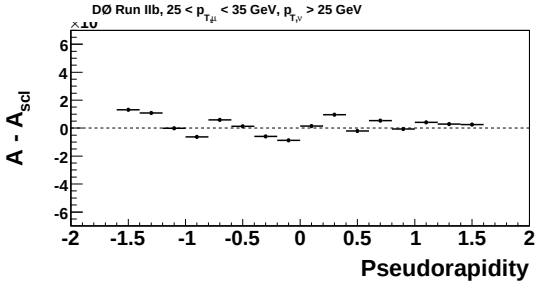

(d) Run IIb, $25 < p_T < 35$ GeV, $\not\!\!E_T > 25$ GeV

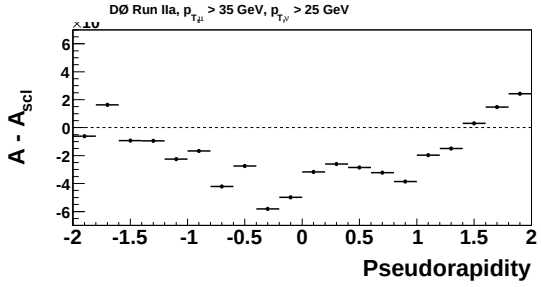

(e) Run IIa, $p_T > 35$ GeV, $\not\!\!E_T > 25$ GeV

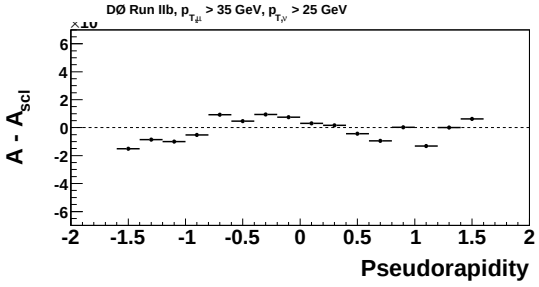

(f) Run IIb, $p_T > 35$ GeV, $\not\!\!E_T > 25$ GeV

Figure 4.28: Difference between A and $A_{\rm scl}$ for Run IIa and Run IIb.

The recoil energy is then calculated and smeared using the following equations:

$$u_{\parallel} = -\alpha \cdot p_{T,W} + \beta \cdot G_2 \tag{4.19}$$

$$u_{\perp} = \beta \cdot G_3 \tag{4.20}$$

$$u_x = u_{\parallel} \cdot \frac{p_{x,W}}{p_{T,W}} + u_{\perp} \cdot \frac{p_{y,W}}{p_{T,W}} \tag{4.21}$$

$$u_y = u_{\parallel} \cdot \frac{p_{x,W}}{p_{T,W}} - u_{\perp} \cdot \frac{p_{y,W}}{p_{T,W}} \tag{4.22}$$

where $\alpha = 0.55 \pm 0.05$ is the hadronic energy scale, and $\beta = 3.5 \pm 0.3$ GeV corresponds to the hadronic calorimeter response [57]. G_2 and G_3 are Gaussian random numbers with mean 0 and rms 1. $p_{T,W}$, $p_{T,x}$, and $p_{T,y}$ are the transverse, x, and y momentum components of the W boson. $u_{\parallel}$ and $u_{\perp}$ are the parallel and perpendicular recoil energy components with respect to the W boson. u_x and u_y are the x and y components of the smeared recoil.

Finally, the $\not\!\!E_T$ is calculated from the smeared muon p_T and the recoil jet as

$$n\not\!\!E_x = -(p_{x,\mu} + u_x) \tag{4.23}$$

$$\not\!\!E_y = -(p_{y,\mu} + u_y) \tag{4.24}$$

$$\not\!\!E_T = \sqrt{\not\!\!E_x^2 + \not\!\!E_y^2} \tag{4.25}$$

where $\not\!\!E_x$ and $\not\!\!E_y$ are the x and y components of the missing tranverse energy, and $p_{x,\mu}$ and $p_{y,\mu}$ are the x and y components of the smeared muon momentum.

The smearing correction is the difference between the asymmetries determined at the generator level ($A_{\rm gen}$) and detector level ($A_{\rm det}$). At the generator level, the asymmetry is measured using generated muon and neutrino p_T's with kinematic cuts matching those used for the data (Section 4.6.1):

1. $p_T^{\mu} > 25$ GeV, $p_T^{\nu} > 25$ GeV
2. $25 < p_T^{\mu} < 35$ GeV, $p_T^{\nu} > 25$ GeV
3. $p_T^{\mu} > 35$ GeV, $p_T^{\nu} > 25$ GeV
4. $25 < p_T^{\mu} < 35$ GeV, $25 < p_T^{\nu} < 35$ GeV
5. $p_T^{\mu} > 35$ GeV, $p_T^{\nu} > 35$ GeV.

At the detector level, the smeared muon p_T and the $\not\!\!E_T$ are used in place of the generated muon and neutrino p_T's. The corrected asymmetry is the scaled asymmetry shifted by the smearing correction:

$$a = A_{\text{gen}} - A_{\text{det}} \tag{4.26}$$

$$A^* = A_{\text{scl}} + a \tag{4.27}$$

where A_{scl} is the scaled asymmetry (Section 4.6.3), a is the smearing correction, and A^* is the corrected asymmetry. Figure 4.29 compares the MC asymmetry at the generator and detector levels. The smearing corrections for Run IIa and Run IIb are shown in Figure 4.30.

The partial systematic uncertainties of the smearing correction are estimated by varying the smearing parameters A, S, α, and β by one sigma, shown in Figures 4.31 and 4.32. To estimate the uncertainty from the MC modeling, we calculate the difference between the asymmetries in the generator level from RESBOS with CTEQ6.6 and POWHEG with CT10. The systematic uncertainty is the sum in quadrature of all partial uncertainties.

4.6.5 CP folding

The muon charge asymmetry is symmetric under CP folding. To measure the CP-folded asymmetry, all numbers of positive and negative events of data and backgrounds are combined as

$$N^+_{\text{CP}}(\eta) = N^+(\eta) + N^-(-\eta) \tag{4.28}$$

$$N^-_{\text{CP}}(\eta) = N^-(\eta) + N^+(-\eta) \tag{4.29}$$

All corrections (g, k, solenoid weighting, and smearing) are recalculated after folding the η bins. The CP-folded corrected asymmetries for the positive and negative η sides are compared for Run IIa and Run IIb in Figures 4.33 and 4.34. To avoid the correlation between the positive and negative sides, we only compare the asymmetries with the statistical uncertainties. The asymmetries in both sides are consistent. The partial uncertainties on the CP folded asymmetry for Run IIa and Run IIb are displayed in Figures 4.35 and 4.36.

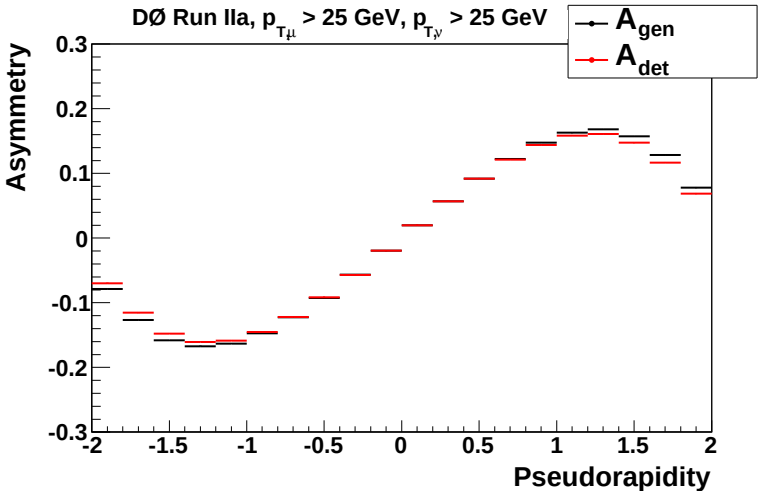

(a) $p_T > 25$ GeV, $\not\!\!E_T > 25$ GeV

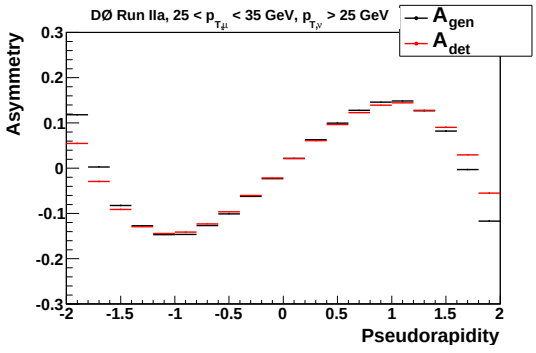

(b) $25 < p_T < 35$ GeV, $\not\!\!E_T > 25$ GeV

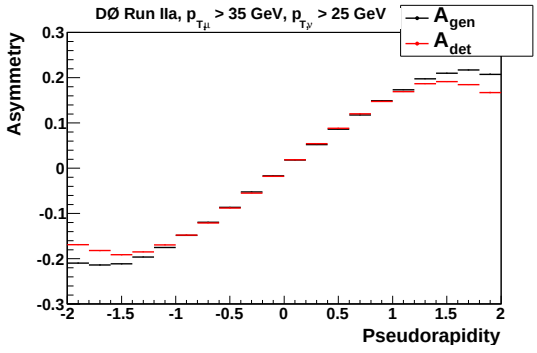

(c) $p_T > 35$ GeV, $\not\!\!E_T > 25$ GeV

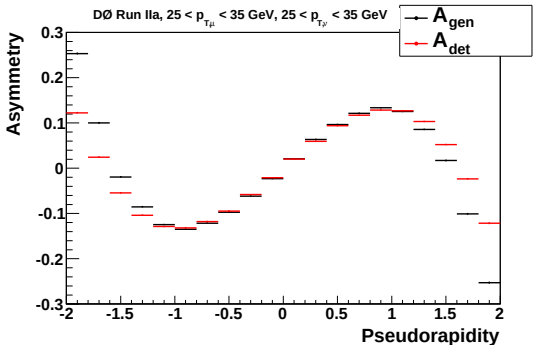

(d) $25 < p_T < 35$ GeV, $25 < \not\!\!E_T < 35$ GeV

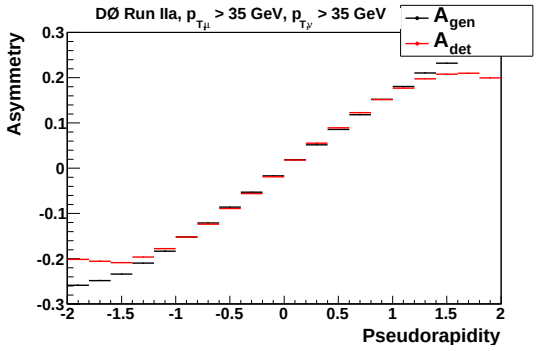

(e) $p_T > 35$ GeV, $\not\!\!E_T > 35$ GeV

Figure 4.29: Comparison of muon charge asymmetry as a function of η between MC at the generation level (black) and the detector level (red).

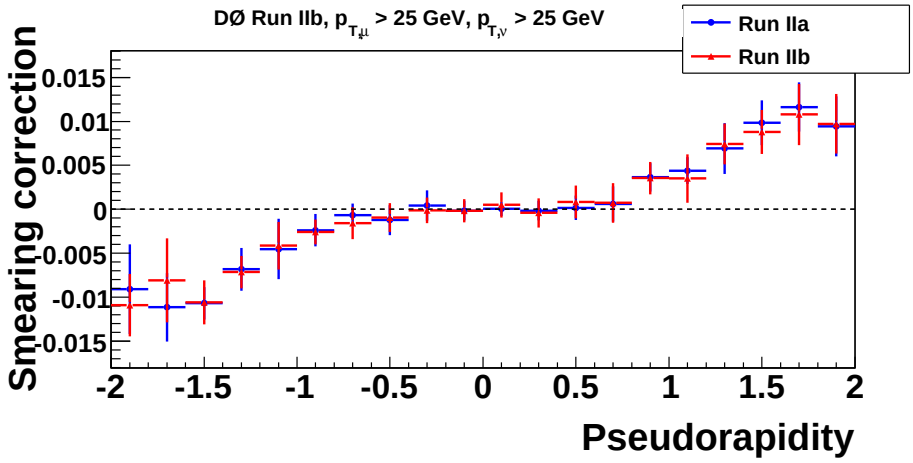

(a) $p_T > 25$ GeV, $\not\!\!E_T > 25$ GeV

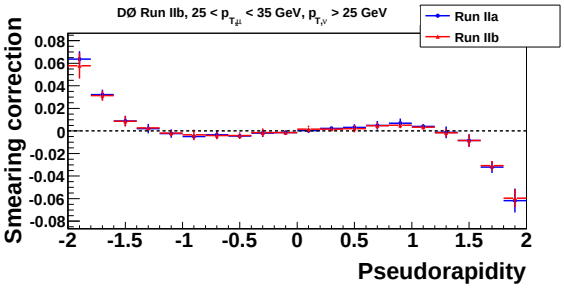

(b) $25 < p_T < 35$ GeV, $\not\!\!E_T > 25$ GeV

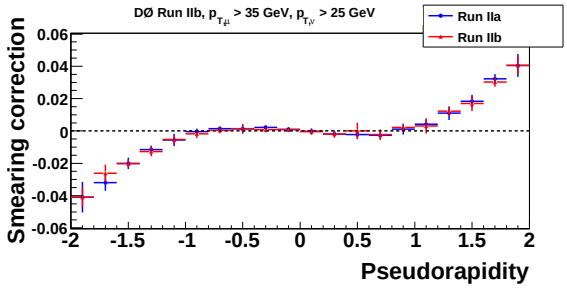

(c) $p_T > 35$ GeV, $\not\!\!E_T > 25$ GeV

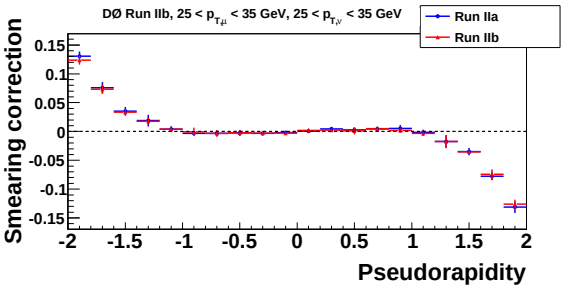

(d) $25 < p_T < 35$ GeV, $25 < \not\!\!E_T < 35$ GeV

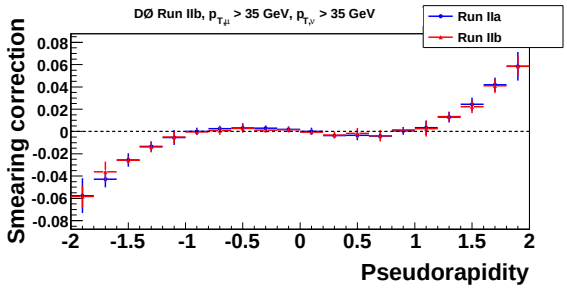

(e) $p_T > 35$ GeV, $\not\!\!E_T > 35$ GeV

Figure 4.30: Smearing correction for Run IIa (blue) and Run IIb (red).

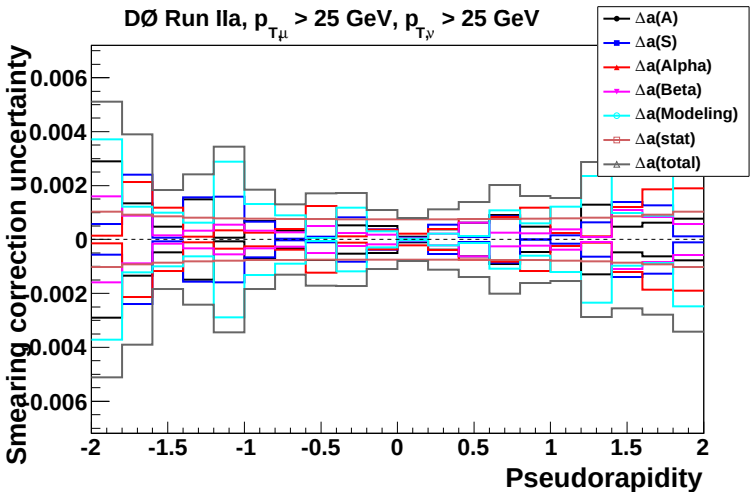

(a) Run IIa, $p_T > 25$ GeV, $\not\!\!E_T > 25$ GeV

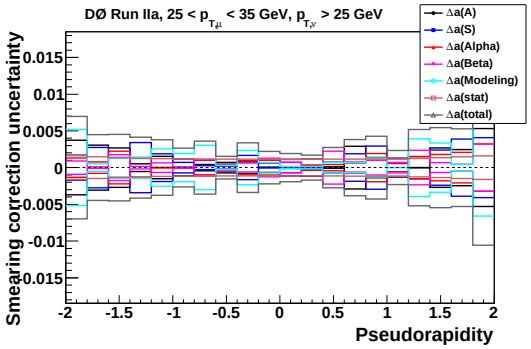

(b) Run IIa, $25 < p_T < 35$ GeV, $\not\!\!E_T > 25$ GeV

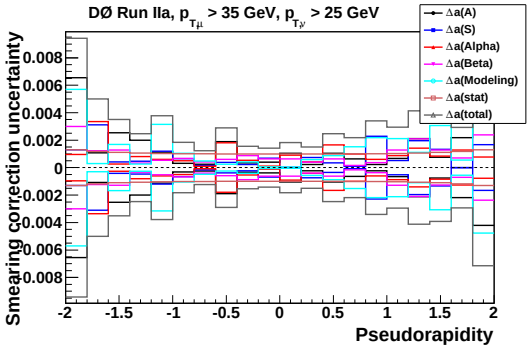

(c) Run IIa, $p_T > 35$ GeV, $\not\!\!E_T > 25$ GeV

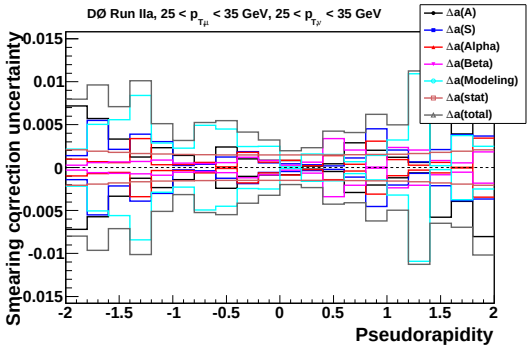

(d) Run IIa, $25 < p_T < 35$ GeV, $25 < \not\!\!E_T < 35$ GeV

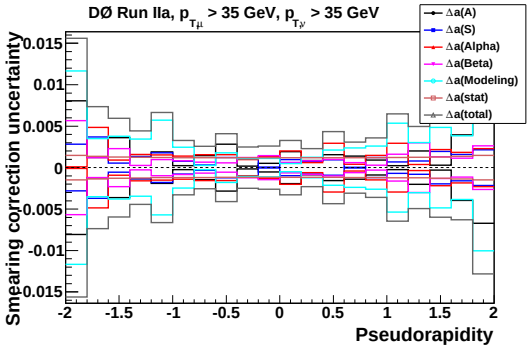

(e) Run IIa, $p_T > 35$ GeV, $\not\!\!E_T > 35$ GeV

Figure 4.31: Partial systematic uncertainties of the smearing correction for Run IIa.

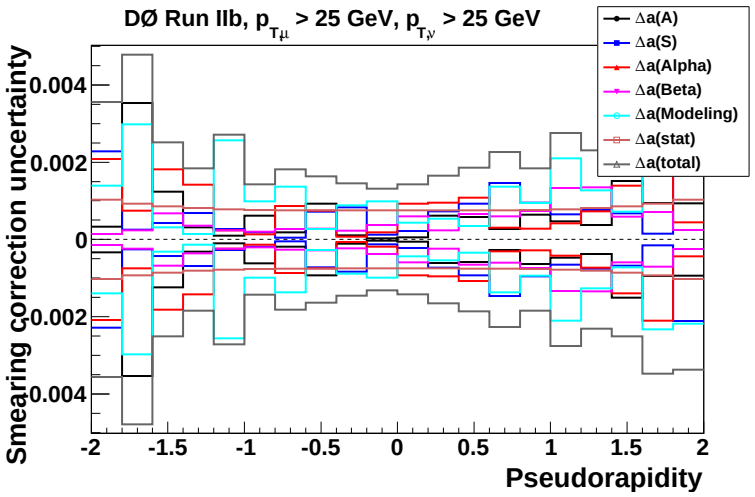

(a) Run IIb, $p_T > 25$ GeV, $\not\!\!E_T > 25$ GeV

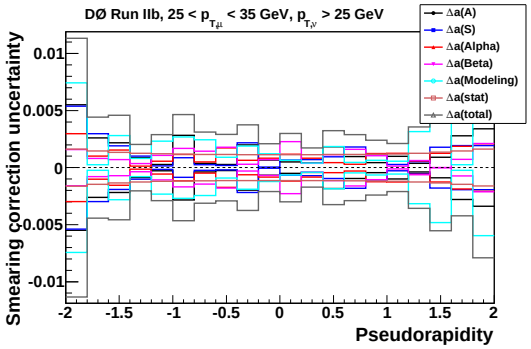

(b) Run IIb, $25 < p_T < 35$ GeV, $\not\!\!E_T > 25$ GeV

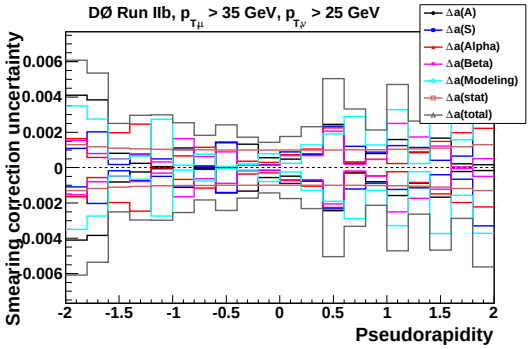

(c) Run IIb, $p_T > 35$ GeV, $\not\!\!E_T > 25$ GeV

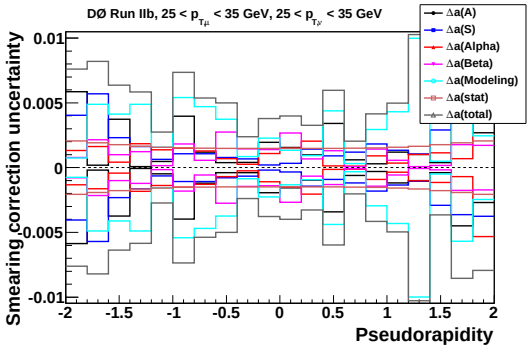

(d) Run IIb, $25 < p_T < 35$ GeV, $25 < \not\!\!E_T < 35$ GeV

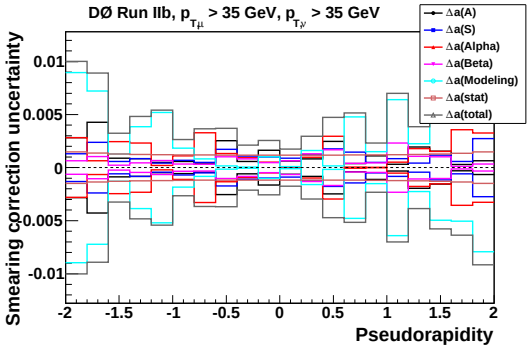

(e) Run IIb, $p_T > 35$ GeV, $\not\!\!E_T > 35$ GeV

Figure 4.32: Partial systematic uncertainties of the smearing correction for Run IIb.

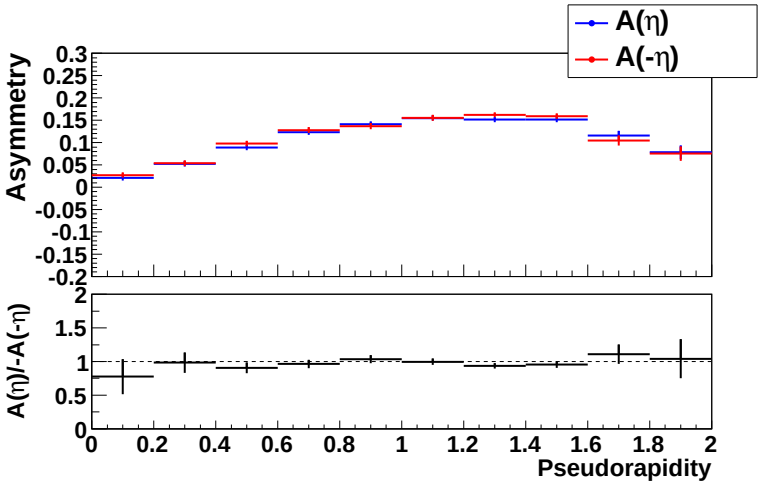

(a) $p_T > 25$ GeV, $\not\!\!E_T > 25$ GeV

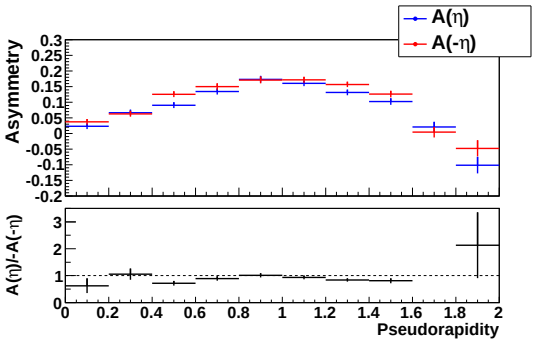

(b) $25 < p_T < 35$ GeV, $\not\!\!E_T > 25$ GeV

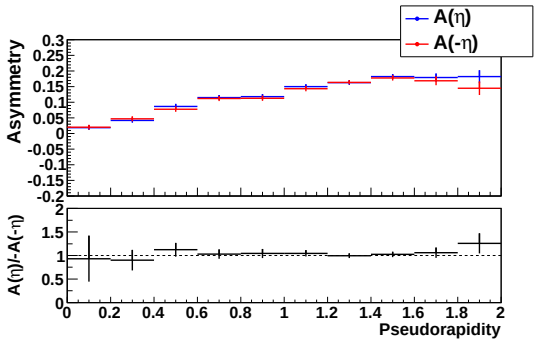

(c) $p_T > 35$ GeV, $\not\!\!E_T > 25$ GeV

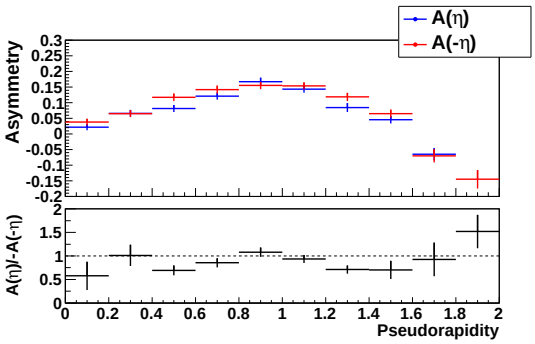

(d) $25 < p_T < 35$ GeV, $25 < \not\!\!E_T < 35$ GeV

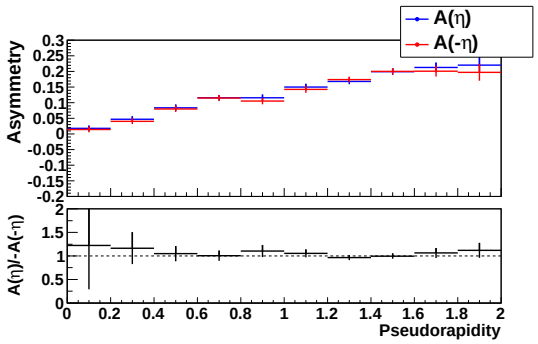

(e) $p_T > 35$ GeV, $\not\!\!E_T > 35$ GeV

Figure 4.33: Comparison of A(η) (blue) and A($-\eta$) (red) for Run IIa.

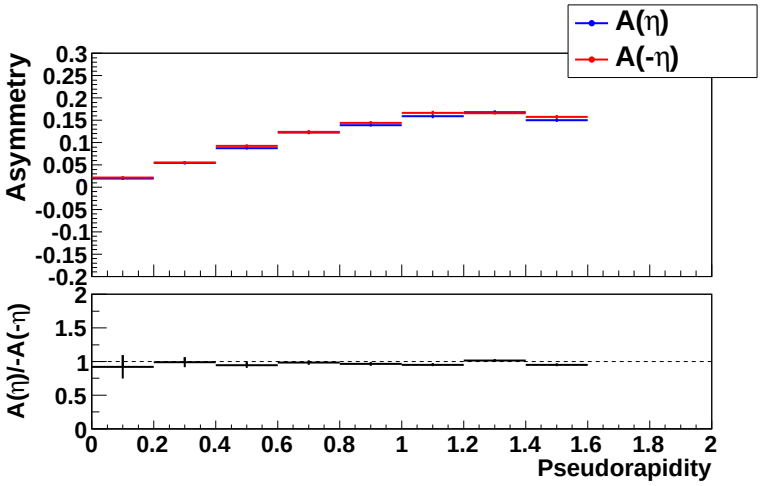

(a) $p_T > 25$ GeV, $\not\!\!E_T > 25$ GeV

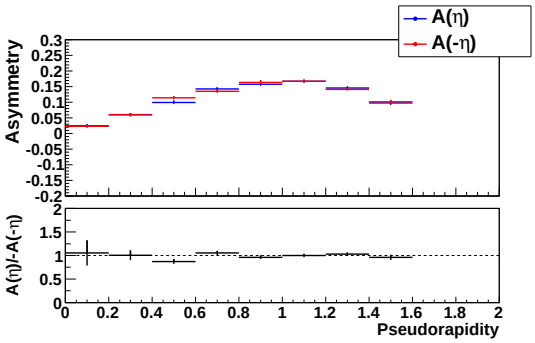

(b) $25 < p_T < 35$ GeV, $\not\!\!E_T > 25$ GeV

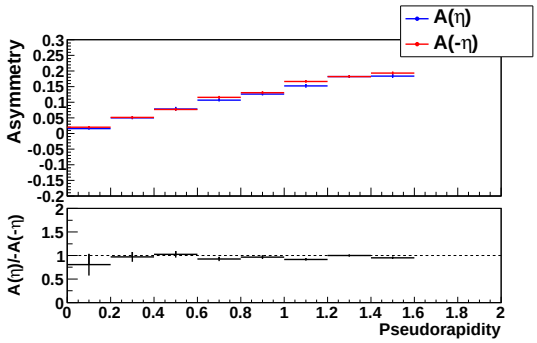

(c) $p_T > 35$ GeV, $\not\!\!E_T > 25$ GeV

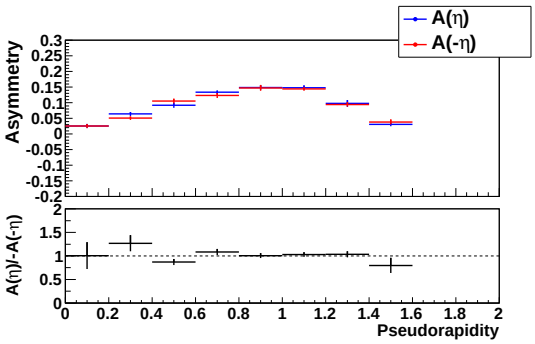

(d) $25 < p_T < 35$ GeV, $25 < \not\!\!E_T < 35$ GeV

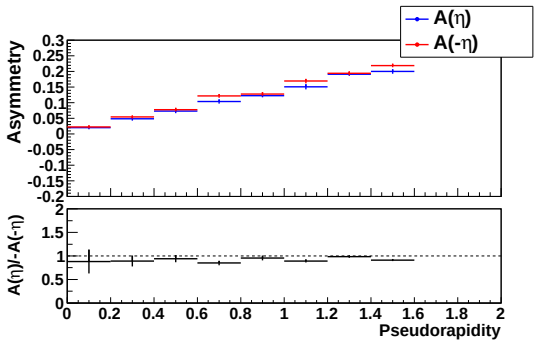

(e) $p_T > 35$ GeV, $\not\!\!E_T > 35$ GeV

Figure 4.34: Comparison of A(η) (blue) and A($-\eta$) (red) for Run IIb.

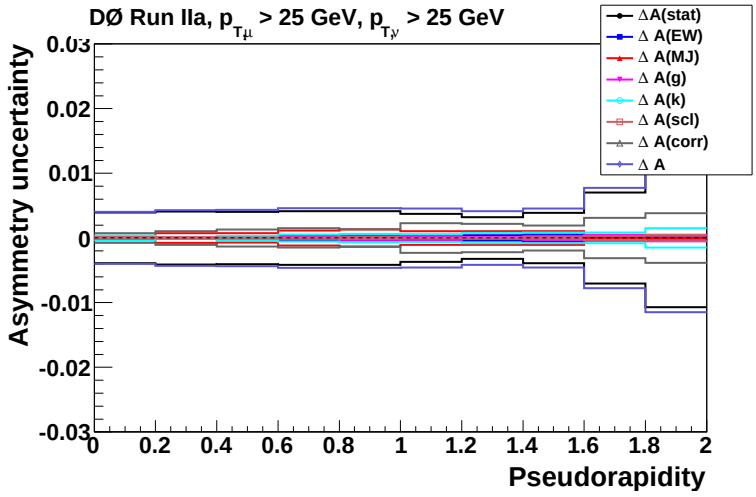

(a) $p_T > 25$ GeV, $\not\!\!E_T > 25$ GeV

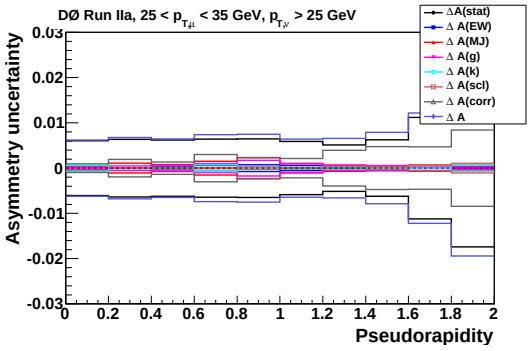

(b) $25 < p_T < 35$ GeV, $\not\!\!E_T > 25$ GeV

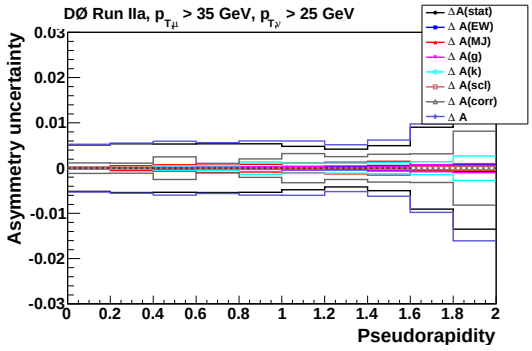

(c) $p_T > 35$ GeV, $\not\!\!E_T > 25$ GeV

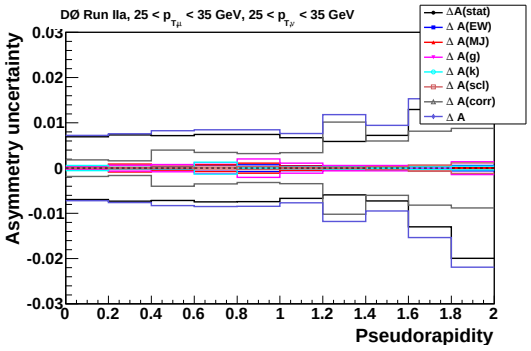

(d) $25 < p_T < 35$ GeV, $25 < \not\!\!E_T < 35$ GeV

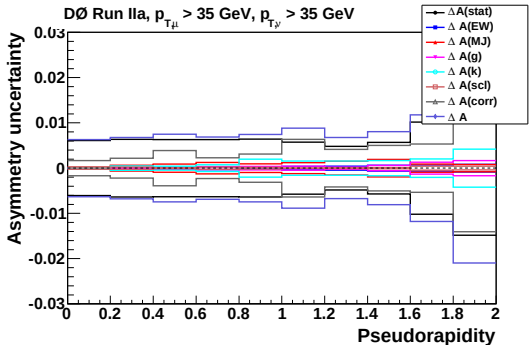

(e) $p_T > 35$ GeV, $\not\!\!E_T > 35$ GeV

Figure 4.35: Partial systematic uncertainties on muon charged asymmetry for Run IIa.

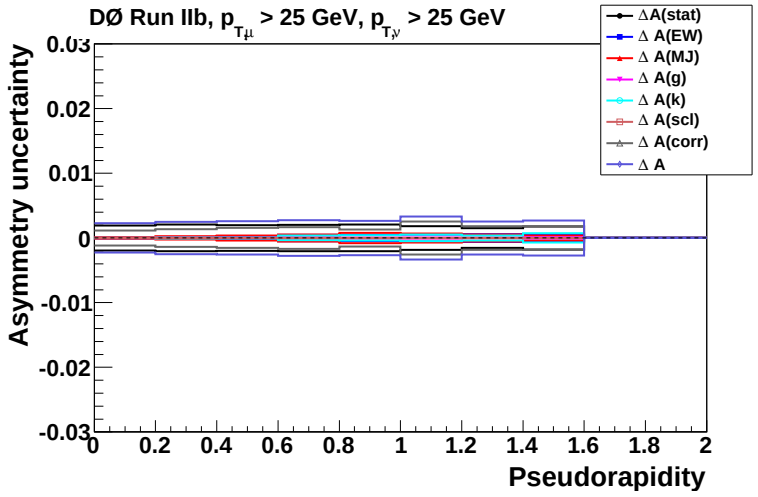

(a) $p_T > 25$ GeV, $\not\!\!E_T > 25$ GeV

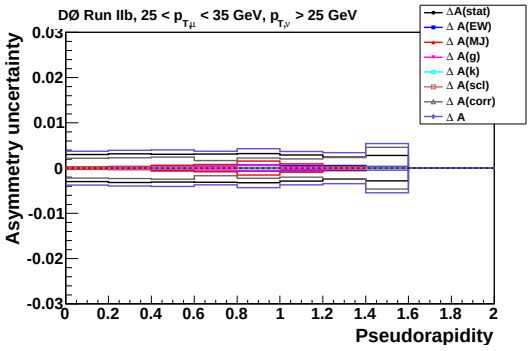

(b) $25 < p_T < 35$ GeV, $\not\!\!E_T > 25$ GeV

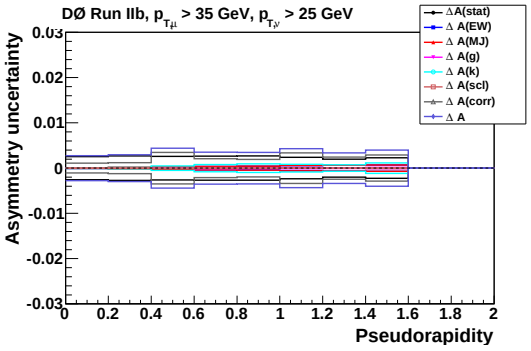

(c) $p_T > 35$ GeV, $\not\!\!E_T > 25$ GeV

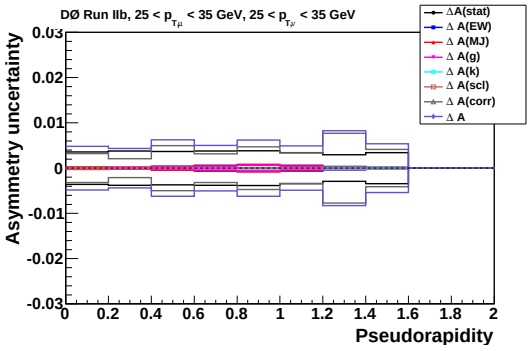

(d) $25 < p_T < 35$ GeV, $25 < \not\!\!E_T < 35$ GeV

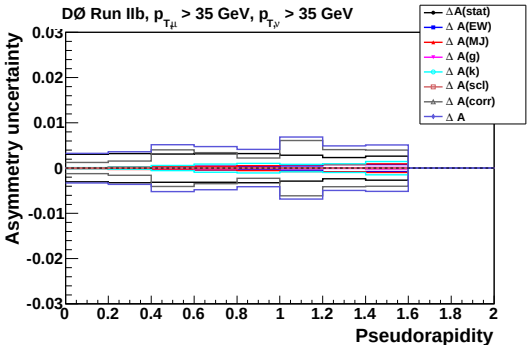

(e) $p_T > 35$ GeV, $\not\!\!E_T > 35$ GeV

Figure 4.36: Partial systematic uncertainties on muon charged asymmetry for Run IIb.

4.6.6 Results for $p_T > 25$ GeV, $\not\!\!E_T >$ 25 GeV

Table 4.13: Corrected CP-folded asymmetry for $p_T > 25$ GeV and $\not\!\!E_T > 25$ GeV for Run IIa: the mean value of η ($< \eta >$), number of weighted positive (negative) muons ($N^{\pm}_{\rm scl}$), number of positive and negative backgrounds ($N^{\pm}_{\rm BG}$), muon charge misID (g), ratio of positive and negative muon efficiencies (k), smearing correction (a), and the corrected CP-folded asymmetry ($A^*_{\rm CP}$).

$< \eta >$	$N^+_{\rm scl}$	$N^-_{\rm scl}$	$N^+_{\rm BG}$	$N^-_{\rm BG}$	g $\times 10^2$	k	a $\times 10^2$	$A^*_{\rm CP}$ $\times 10^2$
0.10	33214	31867	3343.0	3337.3	0.037	0.998	0.010	2.40
0.30	30968	27996	3066.0	2895.9	0.092	1.000	−0.028	5.29
0.50	33026	27770	3206.3	2960.2	0.088	0.999	0.070	9.33
0.71	32277	25507	3389.0	3086.7	0.056	1.002	0.062	12.56
0.89	32513	25188	3956.1	3455.5	0.079	1.000	0.301	13.90
1.11	40497	30467	4328.0	3732.5	0.174	1.000	0.445	15.50
1.30	53446	40102	5083.8	4435.2	0.033	1.003	0.687	15.65
1.49	36857	27952	3419.9	3096.3	0.137	1.006	1.027	15.52
1.69	10967	9041	1062.4	940.0	0.347	1.003	1.139	11.06
1.88	4666	4084	443.3	423.9	0.236	1.009	0.925	7.64

Table 4.14: Uncertainties of the corrected CP-folded asymmetry for $p_T > 25$ GeV and $\not\!\!E_T > 25$ GeV for Run IIa: the mean value of η ($< \eta >$), statistical uncertainty [$\Delta A(N_{\rm data}$], uncertainty from electroweak background [$\Delta A(N_{\rm EW})$], uncertainty from multijet background [$\Delta A(N_{\rm MJ})$], uncertainty from charge misidentification [$\Delta A(g)$], uncertainty from ratio of positive and negative muon efficiencies [$\Delta A(k)$], uncertainty from solenoid weighting [ΔA(scl)], uncertainty from smearing correction [$\Delta A(a)$], and total uncertainty of the corrected CP-folded asymmetry [$\Delta A^*_{\rm CP}$]. All uncertainties have been multiplied by 100.

$< \eta >$	$\Delta A(N_{\rm data})$	$\Delta A(N_{\rm EW})$	$\Delta A(N_{\rm MJ})$	$\Delta A(g)$	$\Delta A(k)$	ΔA(scl)	$\Delta A(a)$	$\Delta A^*_{\rm CP}$
0.10	0.3920	0.010	0.033	0.002	0.038	0.0100	0.073	0.402
0.30	0.4114	0.003	0.073	0.009	0.003	0.0101	0.105	0.431
0.50	0.4041	0.025	0.072	0.014	0.034	0.0062	0.133	0.434
0.71	0.4131	0.044	0.115	0.020	0.053	0.0065	0.150	0.460
0.89	0.4132	0.040	0.130	0.030	0.063	0.0140	0.138	0.462
1.11	0.3716	0.045	0.104	0.029	0.058	0.0006	0.231	0.457
1.30	0.3236	0.041	0.106	0.014	0.081	0.0031	0.217	0.414
1.49	0.3893	0.053	0.105	0.027	0.082	0.0138	0.192	0.458
1.69	0.7044	0.030	0.005	0.047	0.082	0.0314	0.312	0.777
1.88	1.0678	0.037	0.009	0.048	0.149	0.0491	0.385	1.148

Table 4.15: Corrected CP-folded asymmetry for $p_T > 25$ GeV and $\not\!\!E_T > 25$ GeV for Run IIb: the mean value of η ($<\eta>$), number of weighted positive (negative) muons ($N^{\pm}_{\rm scl}$), number of positive and negative backgrounds ($N^{\pm}_{\rm BG}$), muon charge misID (g), ratio of positive and negative muon efficiencies (k), smearing correction (a), and the corrected CP-folded asymmetry ($A^{*}_{\rm CP}$).

$<\eta>$	$N^{+}_{\rm scl}$	$N^{-}_{\rm scl}$	$N^{+}_{\rm BG}$	$N^{-}_{\rm BG}$	g $\times 10^2$	k	a $\times 10^2$	$A^{*}_{\rm CP}$ $\times 10^2$
0.10	135788	130673	12905.4	12702.8	0.052	1.000	0.033	2.06
0.30	124228	111625	11801.2	10906.4	0.110	1.000	−0.015	5.50
0.50	135403	114303	13102.0	12014.3	0.045	0.999	0.089	9.05
0.71	134472	106898	13399.5	12177.2	0.076	1.000	0.115	12.37
0.89	130411	100349	14877.8	12951.6	0.000	0.999	0.307	14.20
1.11	167844	123793	16973.1	14503.2	0.046	1.001	0.382	16.31
1.30	238507	175730	22208.4	19277.4	0.011	1.001	0.728	16.73
1.49	178351	134763	16525.7	14488.3	0.074	1.005	0.969	15.46

Table 4.16: Uncertainties of the corrected CP-folded asymmetry for $p_T > 25$ GeV and $\not\!\!E_T > 25$ GeV for Run IIb: the mean value of η ($<\eta>$), statistical uncertainty [$\Delta A(N_{\rm data}$], uncertainty from electroweak background [$\Delta A(N_{\rm EW})$], uncertainty from multijet background [$\Delta A(N_{\rm MJ})$], uncertainty from charge misidentification [$\Delta A(g)$], uncertainty from ratio of positive and negative muon efficiencies [$\Delta A(k)$], uncertainty from solenoid weighting [ΔA(scl)], uncertainty from smearing correction [$\Delta A(a)$], and total uncertainty of the corrected CP-folded asymmetry [$\Delta A^{*}_{\rm CP}$]. All uncertainties have been multiplied by 100.

$<\eta>$	$\Delta A(N_{\rm data})$	$\Delta A(N_{\rm EW})$	$\Delta A(N_{\rm MJ})$	$\Delta A(g)$	$\Delta A(k)$	ΔA(scl)	$\Delta A(a)$	$\Delta A^{*}_{\rm CP}$
0.10	0.1938	0.006	0.014	0.001	0.005	0.0050	0.117	0.227
0.30	0.2057	0.006	0.026	0.005	0.009	0.0037	0.136	0.248
0.50	0.1994	0.030	0.039	0.005	0.008	0.0032	0.155	0.257
0.71	0.2022	0.050	0.054	0.010	0.036	0.0019	0.168	0.276
0.89	0.2064	0.049	0.080	0.008	0.042	0.0015	0.133	0.266
1.11	0.1831	0.053	0.071	0.010	0.051	0.0029	0.257	0.332
1.30	0.1536	0.059	0.053	0.005	0.037	0.0019	0.183	0.254
1.49	0.1769	0.055	0.039	0.011	0.072	0.0032	0.182	0.272

4.6.7 Results for $25 < p_T < 35$ GeV, $\not\!\!E_T > 25$ GeV

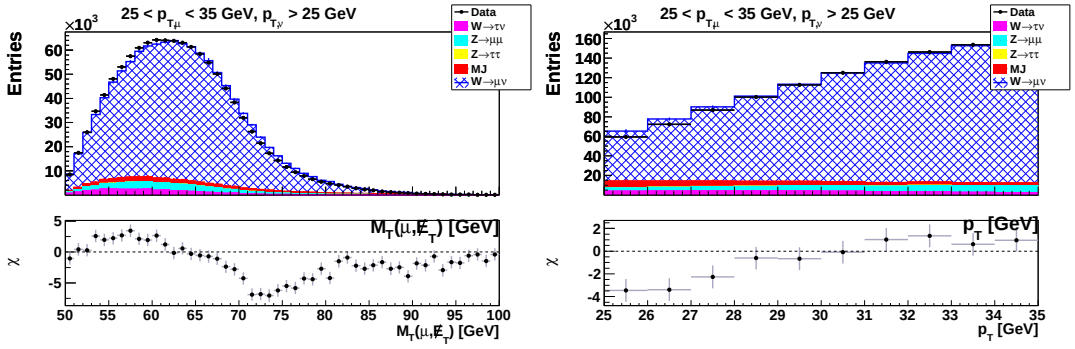

(a) Transverse mass distribution

(b) Muon transverse momentum

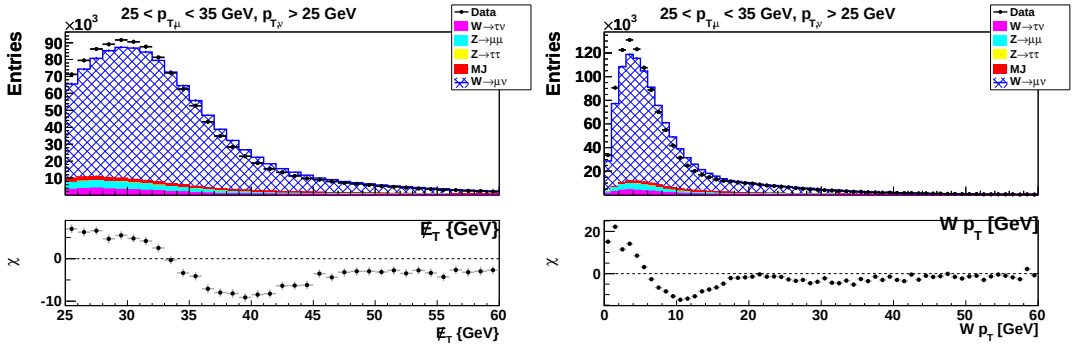

(c) Missing transverse energy

(d) W transverse momentum

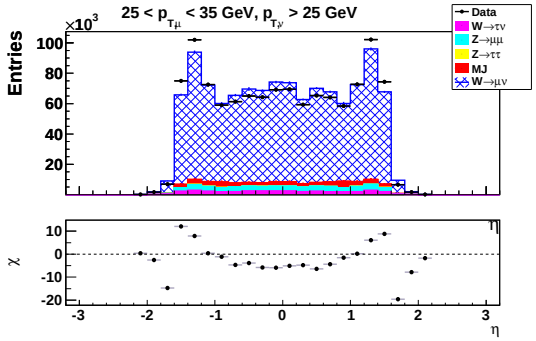

(e) physics η

Figure 4.37: Stacked distributions of M_T, p_T, $\not\!\!E_T$, W p_T, and physics η of data (black dots), multijet background (red), and electroweak backgrounds from Monte Carlo, $W \to \tau\nu$ (pink), $Z \to \mu\mu$ (cyan), $Z \to \tau\tau$ (yellow), and MC signal $W \to \mu\nu$ (hatched blue) for $25 < p_T < 35$ GeV and $\not\!\!E_T > 25$ GeV. The bottom windows display the χ of data w.r.t the total MC, where $\chi = \frac{N_{\text{data}} - N_{\text{MC}}}{\sqrt{\Delta N^2_{\text{data}} + \Delta N^2_{\text{MC}}}}$.

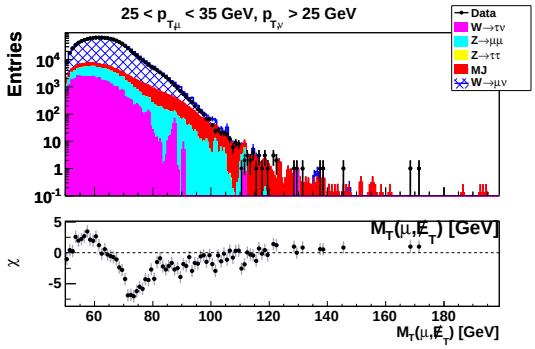

(a) Transverse mass distribution

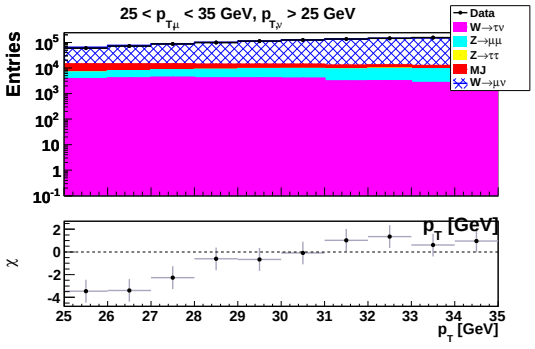

(b) Muon transverse momentum

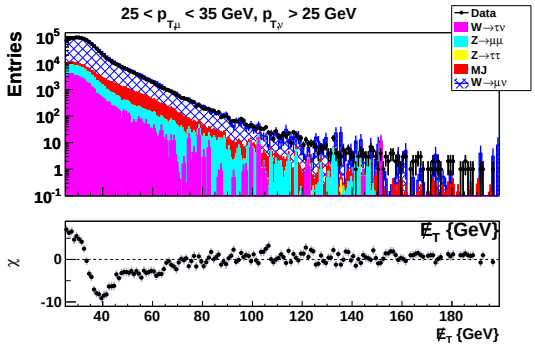

(c) Missing transverse energy

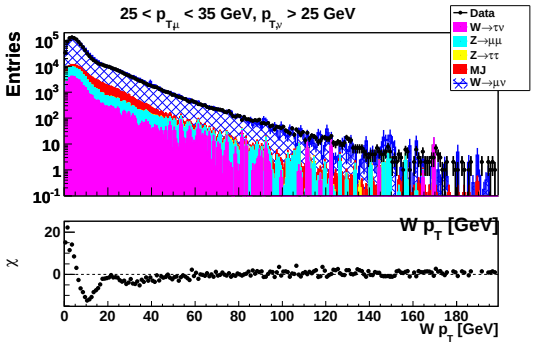

(d) W transverse momentum

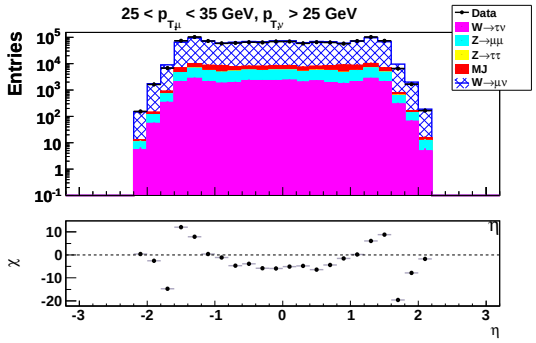

(e) physics η

Figure 4.38: Stacked distributions of M_T, p_T, $\not\!\!E_T$, W p_T, and physics η of data (black dots), multijet background (red), and electroweak backgrounds from Monte Carlo, $W \to \tau\nu$ (pink), $Z \to \mu\mu$ (cyan), $Z \to \tau\tau$ (yellow), and MC signal $W \to \mu\nu$ (hatched blue) for $25 < p_T < 35$ GeV and $\not\!\!E_T > 25$ GeV. The bottom windows display the χ of data w.r.t. the total MC, where $\chi = \frac{N_{\text{data}} - N_{\text{MC}}}{\sqrt{\Delta N^2_{\text{data}} + \Delta N^2_{\text{MC}}}}$.

Table 4.17: Corrected CP-folded asymmetry for $25 < p_T < 35$ GeV and $\not\!\!E_T > 25$ GeV for Run IIa: the mean value of η ($< \eta >$), number of weighted positive (negative) muons ($N^{\pm}_{\rm scl}$), number of positive and negative backgrounds ($N^{\pm}_{\rm BG}$), muon charge misID (g), ratio of positive and negative muon efficiencies (k), smearing correction (a), and the corrected CP-folded asymmetry ($A^{*}_{\rm CP}$).

$< \eta >$	$N^{+}_{\rm scl}$	$N^{-}_{\rm scl}$	$N^{+}_{\rm BG}$	$N^{-}_{\rm BG}$	g $\times 10^2$	k	a $\times 10^2$	$A^{*}_{\rm CP}$ $\times 10^2$
0.10	13869	13206	1773.8	1770.9	0.395	0.998	0.092	3.03
0.30	12976	11530	1605.1	1503.4	0.000	0.999	0.210	6.52
0.50	14082	11579	1645.8	1491.6	0.000	1.001	0.392	10.80
0.71	13468	10440	1681.8	1535.3	0.000	1.002	0.419	14.24
0.89	13451	9920	1939.3	1696.5	0.000	1.000	0.585	17.26
1.11	16300	11986	1905.2	1611.2	0.000	0.998	0.314	16.63
1.30	21255	16063	2032.6	1755.1	0.000	1.001	−0.165	14.44
1.49	14164	11222	1266.3	1148.4	0.000	1.001	−0.859	11.41
1.69	4149	3799	371.7	327.7	0.000	0.995	−3.212	1.25
1.88	1651	1666	156.6	149.0	0.000	1.004	−6.270	−7.18

Table 4.18: Uncertainties of the corrected CP-folded asymmetry for $25 < p_T < 35$ GeV and $\not\!\!E_T > 25$ GeV for Run IIa: the mean value of η ($< \eta >$), statistical uncertainty [$\Delta A(N_{\rm data}$], uncertainty from electroweak background [$\Delta A(N_{\rm EW})$], uncertainty from multijet background [$\Delta A(N_{\rm MJ})$], uncertainty from charge misidentification [$\Delta A(g)$], uncertainty from ratio of positive and negative muon efficiencies [$\Delta A(k)$], uncertainty from solenoid weighting [ΔA(scl)], uncertainty from smearing correction [$\Delta A(a)$], and total uncertainty of the corrected CP-folded asymmetry [$\Delta A^{*}_{\rm CP}$]. All uncertainties have been multiplied by 100.

$< \eta >$	$\Delta A(N_{\rm data})$	$\Delta A(N_{\rm EW})$	$\Delta A(N_{\rm MJ})$	$\Delta A(g)$	$\Delta A(k)$	ΔA(scl)	$\Delta A(a)$	$\Delta A^{*}_{\rm CP}$
0.10	0.6075	0.017	0.053	0.031	0.065	0.0043	0.094	0.621
0.30	0.6376	0.005	0.108	0.051	0.009	0.0107	0.195	0.677
0.50	0.6214	0.037	0.078	0.066	0.016	0.0131	0.138	0.646
0.71	0.6417	0.069	0.153	0.102	0.078	0.0157	0.301	0.740
0.89	0.6472	0.077	0.235	0.174	0.004	0.0280	0.228	0.750
1.11	0.5875	0.057	0.106	0.094	0.021	0.0113	0.212	0.643
1.30	0.5126	0.042	0.070	0.055	0.025	0.0065	0.396	0.656
1.49	0.6241	0.050	0.033	0.060	0.002	0.0301	0.474	0.789
1.69	1.1220	0.002	0.070	0.047	0.003	0.0573	0.469	1.221
1.88	1.7397	0.017	0.041	0.024	0.074	0.1072	0.844	1.939

Table 4.19: Corrected CP-folded asymmetry for $25 < p_T < 35$ GeV and $\not\!\!E_T > 25$ GeV for Run IIb: the mean value of η ($<\eta>$), number of weighted positive (negative) muons ($N^{\pm}_{\rm scl}$), number of positive and negative backgrounds ($N^{\pm}_{\rm BG}$), muon charge misID (g), ratio of positive and negative muon efficiencies (k), smearing correction (a), and the corrected CP-folded asymmetry ($A^{*}_{\rm CP}$).

$<\eta>$	$N^{+}_{\rm scl}$	$N^{-}_{\rm scl}$	$N^{+}_{\rm BG}$	$N^{-}_{\rm BG}$	g $\times 10^2$	k	a $\times 10^2$	$A^{*}_{\rm CP}$ $\times 10^2$
0.10	57063	54721	6726.4	6594.8	0.000	1.000	0.153	2.38
0.30	52412	46746	6225.9	5742.0	0.000	1.001	0.146	6.03
0.50	57327	47341	6555.1	6121.2	0.000	1.000	0.304	10.69
0.71	57008	44460	6602.0	6010.5	0.000	1.000	0.444	13.90
0.89	53858	40237	7155.7	6197.8	0.000	1.001	0.435	16.08
1.11	67556	49417	7383.3	6245.4	0.000	0.999	0.258	16.74
1.30	94985	71919	8593.6	7563.6	0.000	1.001	−0.218	14.36
1.48	68401	55475	5954.6	5292.1	0.000	1.001	−0.856	9.96

Table 4.20: Uncertainties of the corrected CP-folded asymmetry for $25 < p_T < 35$ GeV and $\not\!\!E_T > 25$ GeV for Run IIb: the mean value of η ($<\eta>$), statistical uncertainty [$\Delta A(N_{\rm data}$], uncertainty from electroweak background [$\Delta A(N_{\rm EW})$], uncertainty from multijet background [$\Delta A(N_{\rm MJ})$], uncertainty from charge misidentification [$\Delta A(g)$], uncertainty from ratio of positive and negative muon efficiencies [$\Delta A(k)$], uncertainty from solenoid weighting [ΔA(scl)], uncertainty from smearing correction [$\Delta A(a)$], and total uncertainty of the corrected CP-folded asymmetry [$\Delta A^{*}_{\rm CP}$]. All uncertainties have been multiplied by 100.

$<\eta>$	$\Delta A(N_{\rm data})$	$\Delta A(N_{\rm EW})$	$\Delta A(N_{\rm MJ})$	$\Delta A(g)$	$\Delta A(k)$	ΔA(scl)	$\Delta A(a)$	$\Delta A^{*}_{\rm CP}$
0.10	0.2992	0.006	0.029	0.008	0.003	0.0111	0.220	0.373
0.30	0.3171	0.011	0.036	0.020	0.008	0.0080	0.230	0.394
0.50	0.3077	0.057	0.058	0.026	0.010	0.0013	0.247	0.404
0.71	0.3115	0.072	0.081	0.037	0.005	0.0035	0.167	0.372
0.89	0.3226	0.067	0.155	0.058	0.017	0.0068	0.223	0.432
1.11	0.2889	0.058	0.092	0.034	0.002	0.0036	0.201	0.370
1.30	0.2424	0.057	0.037	0.020	0.010	0.0032	0.235	0.345
1.48	0.2825	0.040	0.008	0.019	0.020	0.0049	0.463	0.544

4.6.8 Results for $p_T > 35$ GeV, $\not\!\!E_T >$ 25 GeV

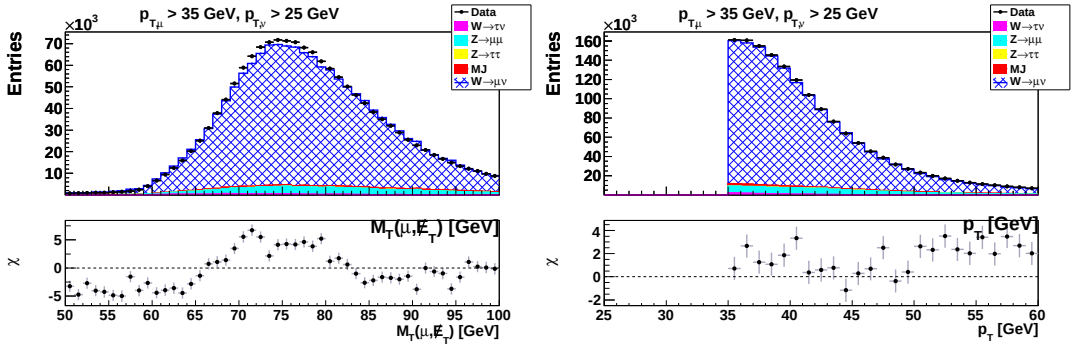

(a) Transverse mass distribution

(b) Muon transverse momentum

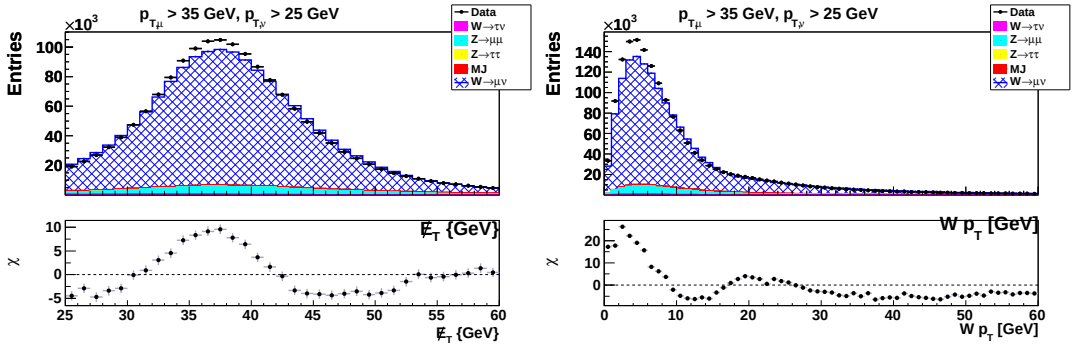

(c) Missing transverse energy

(d) W transverse momentum

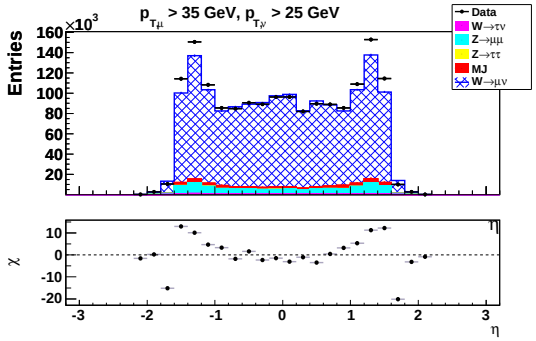

(e) physics η

Figure 4.39: Stacked distributions of M_T, p_T, $\not\!\!E_T$, W p_T, and physics η of data (black dots), multijet background (red), and electroweak backgrounds from Monte Carlo, $W \to \tau\nu$ (pink), $Z \to \mu\mu$ (cyan), $Z \to \tau\tau$ (yellow), and MC signal $W \to \mu\nu$ (hatched blue) for $p_T > 35$ GeV and $\not\!\!E_T > 25$ GeV. The bottom windows display the χ of data w.r.t the total MC, where $\chi = \frac{N_{\text{data}} - N_{\text{MC}}}{\sqrt{\Delta N^2_{\text{data}} + \Delta N^2_{\text{MC}}}}$.

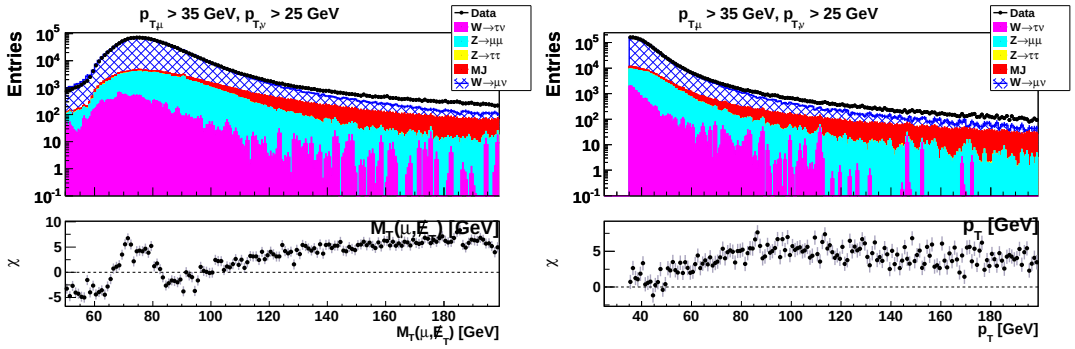

(a) Transverse mass distribution

(b) Muon transverse momentum

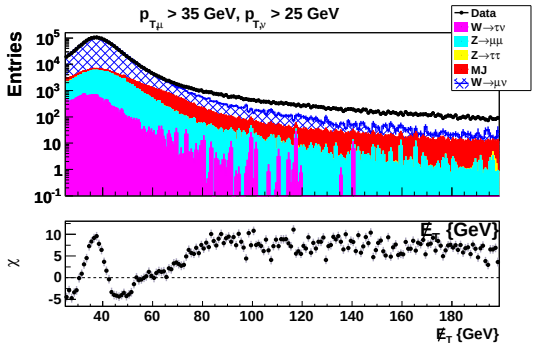

(c) Missing transverse energy

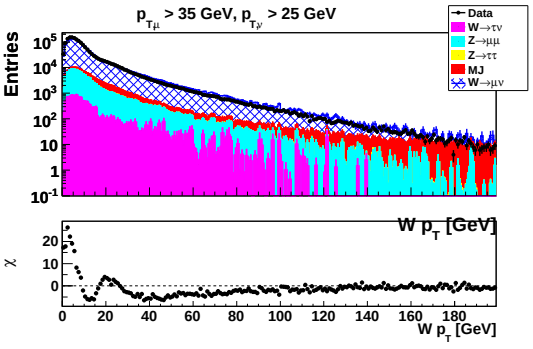

(d) W transverse momentum

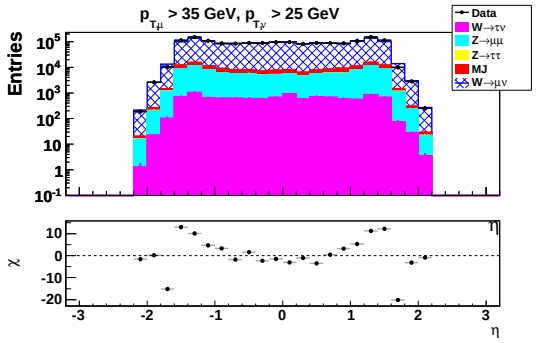

(e) physics η

Figure 4.40: Stacked distributions of M_T, p_T, $\not{E}_T$, W p_T, and physics η of data (black dots), multijet background (red), and electroweak backgrounds from Monte Carlo, $W \to \tau\nu$ (pink), $Z \to \mu\mu$ (cyan), $Z \to \tau\tau$ (yellow), and MC signal $W \to \mu\nu$ (hatched blue) for $p_T > 35$ GeV and $\not{E}_T > 25$ GeV. The bottom windows display the χ of data w.r.t. the total MC, where $\chi = \frac{N_{\text{data}} - N_{\text{MC}}}{\sqrt{\Delta N^2_{\text{data}} + \Delta N^2_{\text{MC}}}}$.

Table 4.21: Corrected CP-folded asymmetry for $p_T > 35$ GeV and $\not\!\!E_T > 25$ GeV for Run IIa: the mean value of η ($<\eta>$), number of weighted positive (negative) muons ($N^{\pm}_{\rm scl}$), number of positive and negative backgrounds ($N^{\pm}_{\rm BG}$), muon charge misID (g), ratio of positive and negative muon efficiencies (k), smearing correction (a), and the corrected CP-folded asymmetry ($A^{*}_{\rm CP}$).

$<\eta>$	$N^{+}_{\rm scl}$	$N^{-}_{\rm scl}$	$N^{+}_{\rm BG}$	$N^{-}_{\rm BG}$	g $\times 10^2$	k	a $\times 10^2$	$A^{*}_{\rm CP}$ $\times 10^2$
0.10	19344	18660	1569.2	1566.5	0.000	0.999	−0.054	1.94
0.30	17991	16465	1460.9	1392.5	0.104	1.000	−0.211	4.41
0.50	18942	16190	1560.5	1468.7	0.102	0.998	−0.173	8.23
0.71	18807	15065	1707.2	1551.4	0.067	1.003	−0.206	11.37
0.89	19061	15267	2016.9	1759.0	0.093	1.003	0.076	11.55
1.11	24196	18480	2422.8	2121.3	0.205	1.001	0.487	14.67
1.30	32192	24039	3051.2	2680.1	0.040	1.004	1.127	16.38
1.49	22693	16729	2153.6	1947.9	0.169	1.005	1.924	18.03
1.69	6818	5242	690.6	612.3	0.435	0.997	3.206	17.42
1.88	3015	2418	286.7	275.0	0.291	0.997	4.074	16.27

Table 4.22: Uncertainties of the corrected CP-folded asymmetry for $p_T > 35$ GeV and $\not\!\!E_T > 25$ GeV for Run IIa: the mean value of η ($<\eta>$), statistical uncertainty [$\Delta A(N_{\rm data}$], uncertainty from electroweak background [$\Delta A(N_{\rm EW})$], uncertainty from multijet background [$\Delta A(N_{\rm MJ})$], uncertainty from charge misidentification [$\Delta A(g)$], uncertainty from ratio of positive and negative muon efficiencies [$\Delta A(k)$], uncertainty from solenoid weighting [ΔA(scl)], uncertainty from smearing correction [$\Delta A(a)$], and total uncertainty of the corrected CP-folded asymmetry [$\Delta A^{*}_{\rm CP}$]. All uncertainties have been multiplied by 100.

$<\eta>$	$\Delta A(N_{\rm data})$	$\Delta A(N_{\rm EW})$	$\Delta A(N_{\rm MJ})$	$\Delta A(g)$	$\Delta A(k)$	ΔA(scl)	$\Delta A(a)$	$\Delta A^{*}_{\rm CP}$
0.10	0.5132	0.007	0.023	0.002	0.016	0.0170	0.114	0.527
0.30	0.5385	0.003	0.053	0.009	0.016	0.0185	0.110	0.553
0.50	0.5319	0.018	0.072	0.015	0.053	0.0017	0.251	0.596
0.71	0.5398	0.030	0.095	0.022	0.046	0.0164	0.106	0.562
0.89	0.5366	0.020	0.086	0.030	0.138	0.0127	0.205	0.598
1.11	0.4798	0.039	0.108	0.033	0.109	0.0068	0.322	0.600
1.30	0.4172	0.041	0.129	0.018	0.112	0.0031	0.253	0.519
1.49	0.4980	0.058	0.152	0.037	0.125	0.0116	0.308	0.621
1.69	0.9035	0.054	0.061	0.082	0.143	0.0357	0.315	0.975
1.88	1.3490	0.072	0.048	0.100	0.272	0.0378	0.816	1.606

Table 4.23: Corrected CP-folded asymmetry for $p_T > 35$ GeV and $\not\!\!E_T > 25$ GeV for Run IIb: the mean value of η ($<\eta>$), number of weighted positive (negative) muons ($N^{\pm}_{\rm scl}$), number of positive and negative backgrounds ($N^{\pm}_{\rm BG}$), muon charge misID (g), ratio of positive and negative muon efficiencies (k), smearing correction (a), and the corrected CP-folded asymmetry ($A^{*}_{\rm CP}$).

$<\eta>$	$N^{+}_{\rm scl}$	$N^{-}_{\rm scl}$	$N^{+}_{\rm BG}$	$N^{-}_{\rm BG}$	g $\times 10^2$	k	a $\times 10^2$	$A^{*}_{\rm CP}$ $\times 10^2$
0.10	78751	75991	6179.2	6108.2	0.056	1.000	−0.060	1.81
0.30	71858	64929	5575.5	5164.5	0.121	1.000	−0.138	5.06
0.50	78102	67011	6547.0	5893.3	0.051	1.001	−0.071	7.76
0.71	77494	62489	6797.8	6166.9	0.088	1.001	−0.131	11.14
0.89	76590	60162	7722.3	6754.1	0.000	1.000	0.204	12.82
1.11	100216	74412	9590.0	8258.0	0.054	1.002	0.420	15.93
1.30	143405	103712	13615.0	11714.0	0.014	1.001	1.251	18.23
1.49	109851	79312	10571.4	9196.4	0.089	1.005	1.854	18.87

Table 4.24: Uncertainties of the corrected CP-folded asymmetry for $p_T > 35$ GeV and $\not\!\!E_T > 25$ GeV for Run IIb: the mean value of η ($<\eta>$), statistical uncertainty [$\Delta A(N_{\rm data}$], uncertainty from electroweak background [$\Delta A(N_{\rm EW})$], uncertainty from multijet background [$\Delta A(N_{\rm MJ})$], uncertainty from charge misidentification [$\Delta A(g)$], uncertainty from ratio of positive and negative muon efficiencies [$\Delta A(k)$], uncertainty from solenoid weighting [ΔA(scl)], uncertainty from smearing correction [$\Delta A(a)$], and total uncertainty of the corrected CP-folded asymmetry [$\Delta A^{*}_{\rm CP}$]. All uncertainties have been multiplied by 100.

$<\eta>$	$\Delta A(N_{\rm data})$	$\Delta A(N_{\rm EW})$	$\Delta A(N_{\rm MJ})$	$\Delta A(g)$	$\Delta A(k)$	ΔA(scl)	$\Delta A(a)$	$\Delta A^{*}_{\rm CP}$
0.10	0.2542	0.007	0.004	0.001	0.009	0.0061	0.108	0.276
0.30	0.2701	0.003	0.021	0.005	0.016	0.0075	0.123	0.298
0.50	0.2617	0.013	0.031	0.005	0.049	0.0011	0.349	0.441
0.71	0.2658	0.038	0.039	0.011	0.080	0.0064	0.209	0.352
0.89	0.2685	0.041	0.042	0.008	0.094	0.0037	0.194	0.350
1.11	0.2367	0.053	0.059	0.011	0.086	0.0020	0.339	0.430
1.30	0.1985	0.063	0.062	0.007	0.072	0.0044	0.246	0.336
1.49	0.2268	0.071	0.068	0.015	0.116	0.0071	0.289	0.398

4.6.9 Results for $25 < p_T < 35$ GeV, $25 < \not\!\!E_T < 35$ GeV

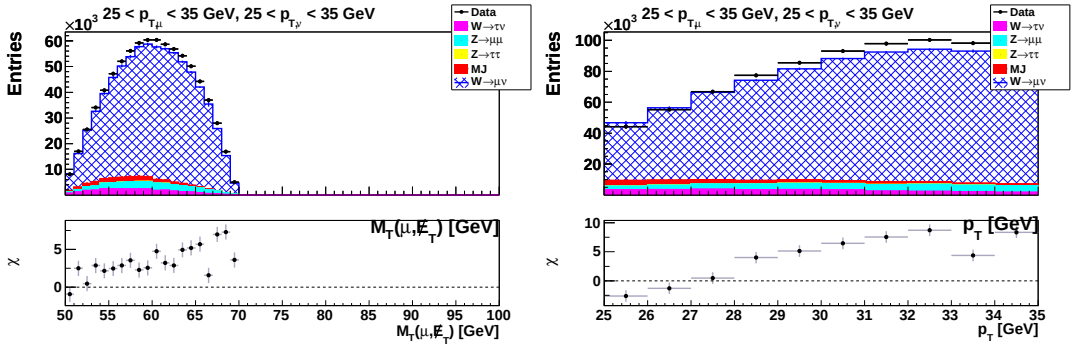

(a) Transverse mass distribution

(b) Muon transverse momentum

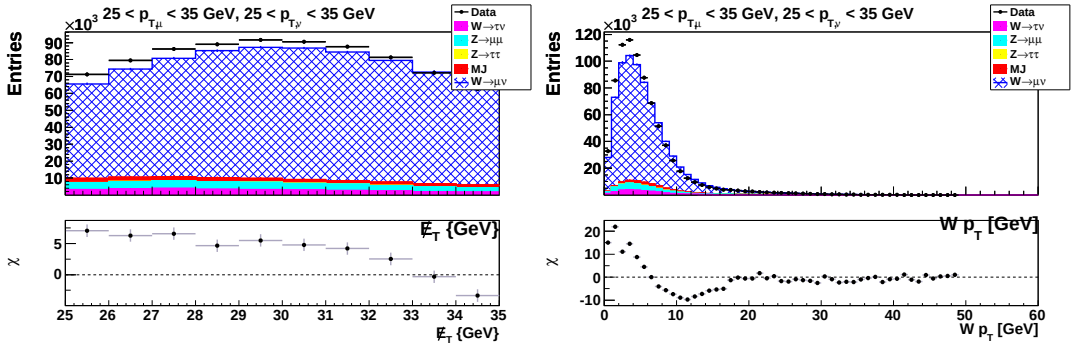

(c) Missing transverse energy

(d) W transverse momentum

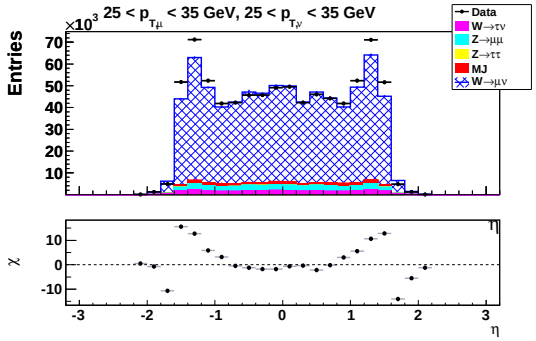

(e) physics η

Figure 4.41: Stacked distributions of M_T, p_T, $\not\!\!E_T$, W p_T, and physics η of data (black dots), multijet background (red), and electroweak backgrounds from Monte Carlo, $W \to \tau\nu$ (pink), $Z \to \mu\mu$ (cyan), $Z \to \tau\tau$ (yellow), and MC signal $W \to \mu\nu$ (hatched blue) for $25 < p_T < 35$ GeV and $25 < \not\!\!E_T < 35$ GeV. The bottom windows display the χ of data w.r.t the total MC, where $\chi = \frac{N_{\text{data}} - N_{\text{MC}}}{\sqrt{\Delta N^2_{\text{data}} + \Delta N^2_{\text{MC}}}}$.

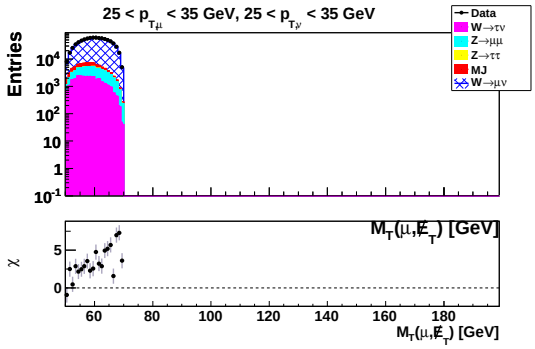

(a) Transverse mass distribution

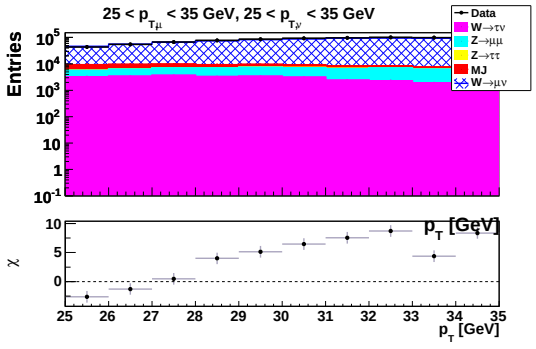

(b) Muon transverse momentum

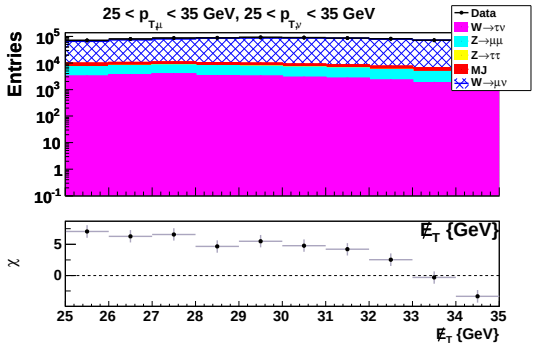

(c) Missing transverse energy

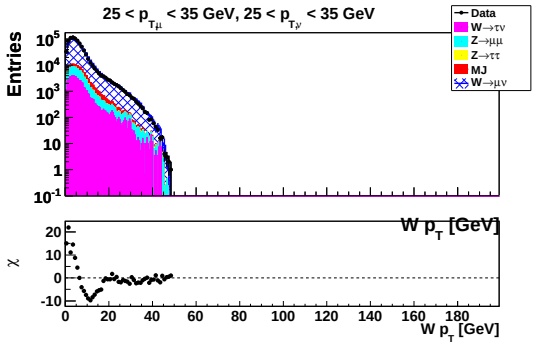

(d) W transverse momentum

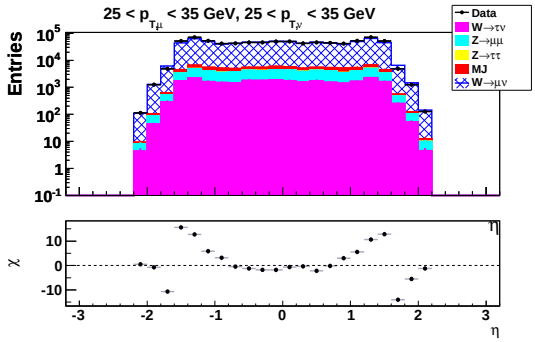

(e) physics η

Figure 4.42: Stacked distributions of M_T, p_T, $\not\!\!E_T$, W p_T, and physics η of data (black dots), multijet background (red), and electroweak backgrounds from Monte Carlo, $W \to \tau\nu$ (pink), $Z \to \mu\mu$ (cyan), $Z \to \tau\tau$ (yellow), and MC signal $W \to \mu\nu$ (hatched blue) for $25 < p_T < 35$ GeV and $25 < \not\!\!E_T < 35$ GeV. The bottom windows display the χ of data w.r.t. the total MC, where $\chi = \frac{N_{\text{data}} - N_{\text{MC}}}{\sqrt{\Delta N^2_{\text{data}} + \Delta N^2_{\text{MC}}}}$.

Table 4.25: Corrected CP-folded asymmetry for $25 < p_T < 35$ GeV and $25 < \not\!\!E_T < 35$ GeV for Run IIa: the mean value of η ($< \eta >$), number of weighted positive (negative) muons ($N^{\pm}_{\rm scl}$), number of positive and negative backgrounds ($N^{\pm}_{\rm BG}$), muon charge misID (g), ratio of positive and negative muon efficiencies (k), smearing correction (a), and the corrected CP-folded asymmetry ($A^{*}_{\rm CP}$).

$< \eta >$	$N^{+}_{\rm scl}$	$N^{-}_{\rm scl}$	$N^{+}_{\rm BG}$	$N^{-}_{\rm BG}$	g $\times 10^2$	k	a $\times 10^2$	$A^{*}_{\rm CP}$ $\times 10^2$
0.10	10629	10124	1233.3	1234.5	0.000	0.998	0.134	3.02
0.30	9827	8752	1127.6	1068.7	0.000	1.000	0.375	6.59
0.50	10558	8782	1156.6	1039.2	0.000	1.001	0.257	9.90
0.71	9951	7844	1113.0	1026.6	0.000	1.003	0.388	13.16
0.89	10175	7607	1121.3	1006.8	0.000	0.999	0.412	16.13
1.11	12454	9347	1176.7	1021.9	0.000	0.998	−0.295	14.87
1.30	15719	12464	1319.6	1157.7	0.000	1.001	−1.817	10.15
1.49	10247	8622	826.1	775.9	0.000	1.002	−3.517	5.52
1.68	3009	2961	255.0	234.7	0.000	0.992	−7.675	−6.77
1.88	1211	1311	116.0	108.7	0.000	1.002	−13.099	−17.89

Table 4.26: Uncertainties of the corrected CP-folded asymmetry for $25 < p_T < 35$ GeV and $25 < \not\!\!E_T < 35$ GeV for Run IIa: the mean value of η ($< \eta >$), statistical uncertainty [$\Delta A(N_{\rm data}$], uncertainty from electroweak background [$\Delta A(N_{\rm EW})$], uncertainty from multijet background [$\Delta A(N_{\rm MJ})$], uncertainty from charge misidentification [$\Delta A(g)$], uncertainty from ratio of positive and negative muon efficiencies [$\Delta A(k)$], uncertainty from solenoid weighting [ΔA(scl)], uncertainty from smearing correction [$\Delta A(a)$], and total uncertainty of the corrected CP-folded asymmetry [$\Delta A^{*}_{\rm CP}$]. All uncertainties have been multiplied by 100.

$< \eta >$	$\Delta A(N_{\rm data})$	$\Delta A(N_{\rm EW})$	$\Delta A(N_{\rm MJ})$	$\Delta A(g)$	$\Delta A(k)$	ΔA(scl)	$\Delta A(a)$	$\Delta A^{*}_{\rm CP}$
0.10	0.6939	0.019	0.036	0.029	0.057	0.0063	0.182	0.721
0.30	0.7323	0.012	0.088	0.066	0.016	0.0151	0.164	0.759
0.50	0.7160	0.031	0.043	0.079	0.017	0.0081	0.400	0.826
0.71	0.7447	0.071	0.076	0.120	0.130	0.0205	0.349	0.848
0.89	0.7427	0.075	0.110	0.205	0.011	0.0312	0.320	0.845
1.11	0.6702	0.055	0.051	0.113	0.020	0.0142	0.341	0.765
1.30	0.5917	0.028	0.040	0.060	0.024	0.0090	1.018	1.181
1.49	0.7261	0.038	0.018	0.060	0.005	0.0350	0.601	0.946
1.68	1.2960	0.015	0.041	0.006	0.028	0.0707	0.816	1.534
1.88	1.9931	0.060	0.012	0.142	0.042	0.1162	0.879	2.187

Table 4.27: Corrected CP-folded asymmetry for $25 < p_T < 35$ GeV and $25 < \not\!\!E_T < 35$ GeV for Run IIb: the mean value of η ($< \eta >$), number of weighted positive (negative) muons ($N^{\pm}_{\rm scl}$), number of positive and negative backgrounds ($N^{\pm}_{\rm BG}$), muon charge misID (g), ratio of positive and negative muon efficiencies (k), smearing correction (a), and the corrected CP-folded asymmetry ($A^{*}_{\rm CP}$).

$< \eta >$	$N^{+}_{\rm scl}$	$N^{-}_{\rm scl}$	$N^{+}_{\rm BG}$	$N^{-}_{\rm BG}$	g $\times 10^2$	k	a $\times 10^2$	$A^{*}_{\rm CP}$ $\times 10^2$
0.10	39926	38198	4712.1	4554.7	0.000	0.999	0.222	2.53
0.30	36627	32836	4354.7	3936.6	0.000	1.001	0.262	5.74
0.50	39517	32925	4589.7	4166.9	0.000	1.000	0.181	9.88
0.71	38305	30415	4246.5	3875.4	0.000	1.000	0.401	12.81
0.89	37521	28472	4302.0	3761.5	0.000	1.001	0.139	14.79
1.11	47330	35696	4588.5	4054.7	0.000	0.999	−0.352	14.60
1.30	63344	50884	5635.2	5019.4	0.000	1.002	−1.770	9.59
1.48	45110	39451	3865.2	3570.4	0.000	1.001	−3.441	3.45

Table 4.28: Uncertainties of the corrected CP-folded asymmetry for $25 < p_T < 35$ GeV and $25 < \not\!\!E_T < 35$ GeV for Run IIb: the mean value of η ($< \eta >$), statistical uncertainty [$\Delta A(N_{\rm data}$], uncertainty from electroweak background [$\Delta A(N_{\rm EW})$], uncertainty from multijet background [$\Delta A(N_{\rm MJ})$], uncertainty from charge misidentification [$\Delta A(g)$], uncertainty from ratio of positive and negative muon efficiencies [$\Delta A(k)$], uncertainty from solenoid weighting [ΔA(scl)], uncertainty from smearing correction [$\Delta A(a)$], and total uncertainty of the corrected CP-folded asymmetry [$\Delta A^{*}_{\rm CP}$]. All uncertainties have been multiplied by 100.

$< \eta >$	$\Delta A(N_{\rm data})$	$\Delta A(N_{\rm EW})$	$\Delta A(N_{\rm MJ})$	$\Delta A(g)$	$\Delta A(k)$	ΔA(scl)	$\Delta A(a)$	$\Delta A^{*}_{\rm CP}$
0.10	0.3580	0.000	0.029	0.011	0.008	0.0145	0.320	0.481
0.30	0.3791	0.000	0.022	0.023	0.005	0.0133	0.211	0.435
0.50	0.3701	0.040	0.044	0.028	0.001	0.0068	0.498	0.624
0.71	0.3790	0.065	0.055	0.038	0.001	0.0042	0.316	0.503
0.89	0.3858	0.064	0.084	0.063	0.014	0.0120	0.472	0.622
1.11	0.3438	0.064	0.055	0.036	0.008	0.0096	0.336	0.490
1.30	0.2941	0.039	0.023	0.018	0.017	0.0039	0.770	0.826
1.48	0.3430	0.024	0.005	0.014	0.018	0.0072	0.412	0.537

4.6.10 Results for $p_T > 35$ GeV, $\not\!\!E_T >$ 35 GeV

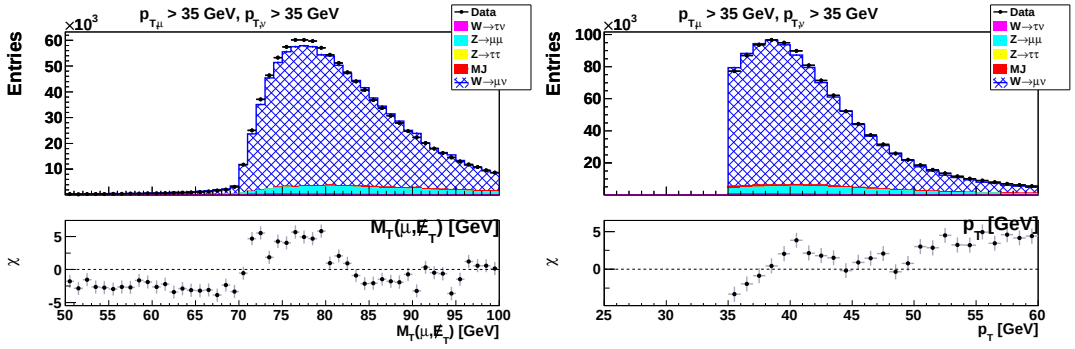

(a) Transverse mass distribution

(b) Muon transverse momentum

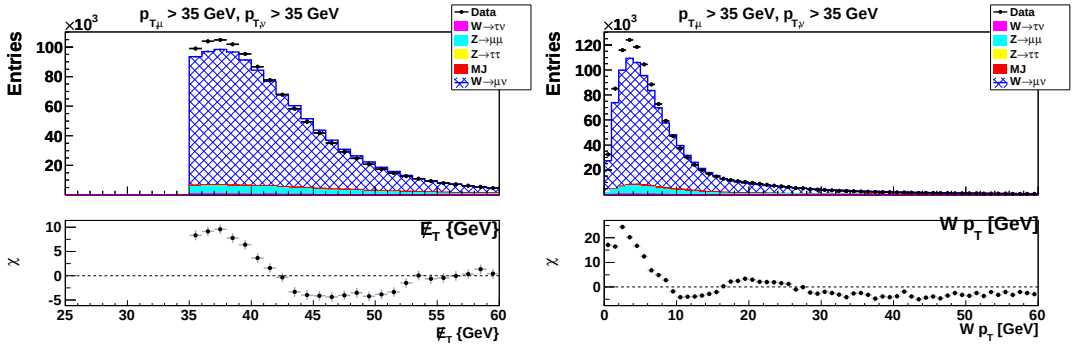

(c) Missing transverse energy

(d) W transverse momentum

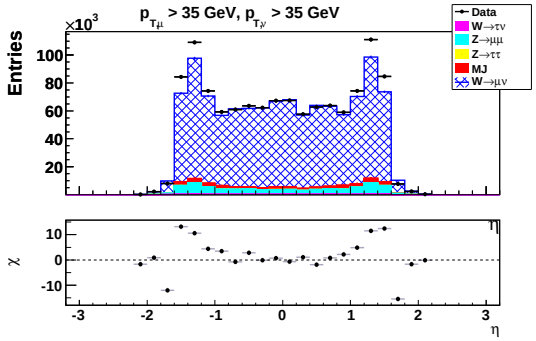

(e) physics η

Figure 4.43: Stacked distributions of M_T, p_T, $\not\!\!E_T$, W p_T, and physics η of data (black dots), multijet background (red), and electroweak backgrounds from Monte Carlo, $W \to \tau\nu$ (pink), $Z \to \mu\mu$ (cyan), $Z \to \tau\tau$ (yellow), and MC signal $W \to \mu\nu$ (hatched blue) for $p_T > 35$ GeV and $\not\!\!E_T > 35$ GeV. The bottom windows display the χ of data w.r.t the total MC, where $\chi = \frac{N_{\text{data}} - N_{\text{MC}}}{\sqrt{\Delta N^2_{\text{data}} + \Delta N^2_{\text{MC}}}}$.

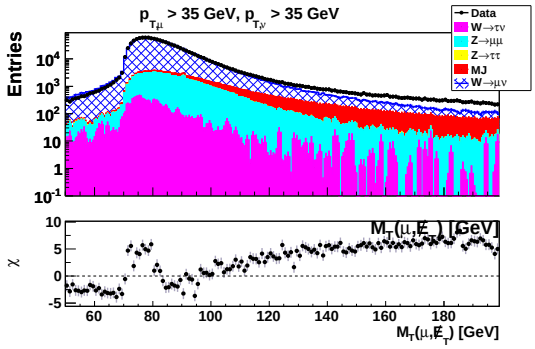

(a) Transverse mass distribution

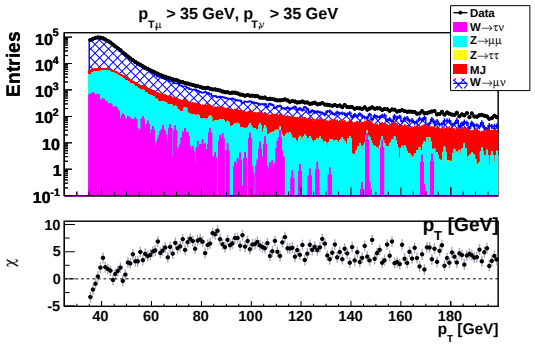

(b) Muon transverse momentum

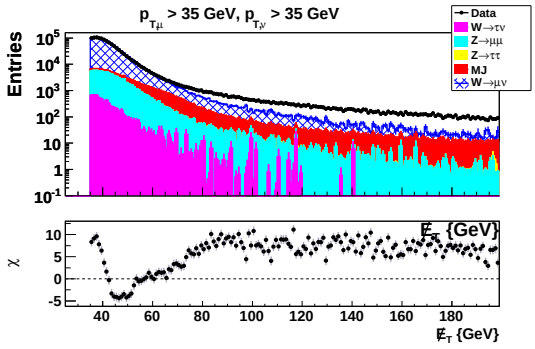

(c) Missing transverse energy

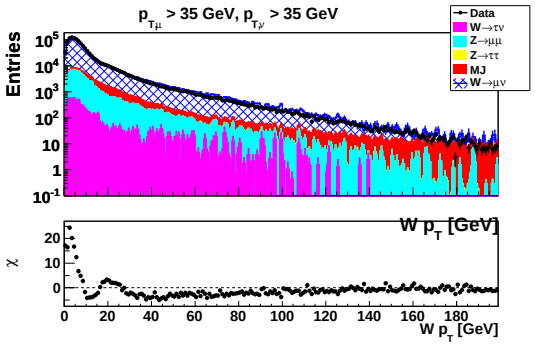

(d) W transverse momentum

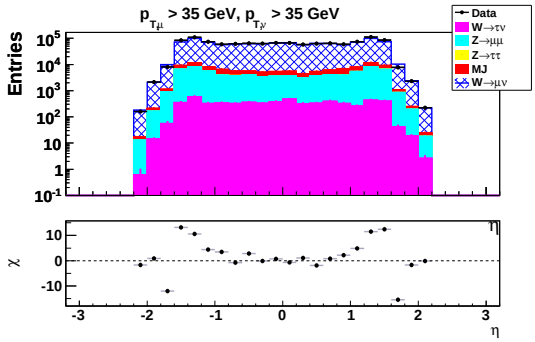

(e) physics η

Figure 4.44: Stacked distributions of M_T, p_T, $\not{E}_T$, W p_T, and physics η of data (black dots), multijet background (red), and electroweak backgrounds from Monte Carlo, $W \to \tau\nu$ (pink), $Z \to \mu\mu$ (cyan), $Z \to \tau\tau$ (yellow), and MC signal $W \to \mu\nu$ (hatched blue) for $p_T > 35$ GeV and $\not{E}_T > 35$ GeV. The bottom windows display the χ of data w.r.t. the total MC, where $\chi = \frac{N_{\text{data}} - N_{\text{MC}}}{\sqrt{\Delta N^2_{\text{data}} + \Delta N^2_{\text{MC}}}}$.

Table 4.29: Corrected CP-folded asymmetry for $p_T > 35$ GeV and $\not\!\!E_T > 35$ GeV for Run IIa: the mean value of η ($<\eta>$), number of weighted positive (negative) muons ($N^{\pm}_{\rm scl}$), number of positive and negative backgrounds ($N^{\pm}_{\rm BG}$), muon charge misID (g), ratio of positive and negative muon efficiencies (k), smearing correction (a), and the corrected CP-folded asymmetry ($A^{*}_{\rm CP}$).

$<\eta>$	$N^{+}_{\rm scl}$	$N^{-}_{\rm scl}$	$N^{+}_{\rm BG}$	$N^{-}_{\rm BG}$	g $\times 10^2$	k	a $\times 10^2$	$A^{*}_{\rm CP}$ $\times 10^2$
0.10	13723	13317	1122.5	1122.4	0.000	0.999	−0.089	1.60
0.30	12827	11754	1026.6	1007.4	0.073	1.000	−0.337	4.35
0.50	13474	11522	1092.1	1045.1	0.139	0.996	−0.333	8.22
0.71	13706	10933	1213.4	1124.8	0.090	1.004	−0.342	11.54
0.89	13408	10817	1476.6	1288.3	0.127	1.004	0.022	11.05
1.11	16879	12880	1767.8	1538.5	0.282	1.003	0.441	14.64
1.30	24085	17791	2343.1	2056.4	0.055	1.005	1.312	17.13
1.49	17501	12569	1698.0	1534.3	0.237	1.007	2.500	20.00
1.69	5447	4028	548.4	485.5	0.611	0.996	4.239	20.71
1.88	2535	1942	233.1	223.3	0.402	0.992	5.798	20.83

Table 4.30: Uncertainties of the corrected CP-folded asymmetry for $p_T > 35$ GeV and $\not\!\!E_T > 35$ GeV for Run IIa: the mean value of η ($<\eta>$), statistical uncertainty [$\Delta A(N_{\rm data}$], uncertainty from electroweak background [$\Delta A(N_{\rm EW})$], uncertainty from multijet background [$\Delta A(N_{\rm MJ})$], uncertainty from charge misidentification [$\Delta A(g)$], uncertainty from ratio of positive and negative muon efficiencies [$\Delta A(k)$], uncertainty from solenoid weighting [ΔA(scl)], uncertainty from smearing correction [$\Delta A(a)$], and total uncertainty of the corrected CP-folded asymmetry [$\Delta A^{*}_{\rm CP}$]. All uncertainties have been multiplied by 100.

$<\eta>$	$\Delta A(N_{\rm data})$	$\Delta A(N_{\rm EW})$	$\Delta A(N_{\rm MJ})$	$\Delta A(g)$	$\Delta A(k)$	ΔA(scl)	$\Delta A(a)$	$\Delta A^{*}_{\rm CP}$
0.10	0.6084	0.006	0.021	0.002	0.010	0.0208	0.169	0.632
0.30	0.6376	0.010	0.066	0.010	0.048	0.0224	0.219	0.680
0.50	0.6306	0.020	0.089	0.020	0.046	0.0080	0.388	0.748
0.71	0.6326	0.032	0.126	0.031	0.073	0.0222	0.228	0.690
0.89	0.6390	0.017	0.095	0.040	0.200	0.0165	0.311	0.746
1.11	0.5744	0.037	0.121	0.045	0.156	0.0019	0.638	0.883
1.30	0.4830	0.043	0.153	0.025	0.157	0.0096	0.415	0.675
1.49	0.5688	0.064	0.195	0.057	0.166	0.0111	0.504	0.807
1.69	1.0167	0.067	0.089	0.133	0.203	0.0436	0.534	1.180
1.88	1.4819	0.085	0.078	0.167	0.418	0.0411	1.408	2.097

Table 4.31: Corrected CP-folded asymmetry for $p_T > 35$ GeV and $\not\!\!E_T > 35$ GeV for Run IIb: the mean value of η ($<\eta>$), number of weighted positive (negative) muons ($N^{\pm}_{\rm scl}$), number of positive and negative backgrounds ($N^{\pm}_{\rm BG}$), muon charge misID (g), ratio of positive and negative muon efficiencies (k), smearing correction (a), and the corrected CP-folded asymmetry ($A^{*}_{\rm CP}$).

$<\eta>$	$N^{+}_{\rm scl}$	$N^{-}_{\rm scl}$	$N^{+}_{\rm BG}$	$N^{-}_{\rm BG}$	g $\times 10^2$	k	a $\times 10^2$	$A^{*}_{\rm CP}$ $\times 10^2$
0.10	55113	52740	4396.3	4271.5	0.060	1.000	-0.112	2.13
0.30	50136	45200	3868.9	3630.5	0.119	1.000	-0.212	5.15
0.50	54667	46871	4637.2	4108.1	0.069	1.001	-0.220	7.57
0.71	55484	44567	4823.4	4397.0	0.087	1.001	-0.227	11.27
0.89	52687	41495	5533.4	4791.4	0.000	1.001	0.090	12.52
1.11	68365	50566	6873.8	5813.7	0.048	1.003	0.373	16.02
1.30	104113	74217	10012.1	8793.8	0.019	1.002	1.362	19.25
1.49	81672	57221	8118.8	6975.6	0.049	1.006	2.397	20.96

Table 4.32: Uncertainties of the corrected CP-folded asymmetry for $p_T > 35$ GeV and $\not\!\!E_T > 35$ GeV for Run IIb: the mean value of η ($<\eta>$), statistical uncertainty [$\Delta A(N_{\rm data}$], uncertainty from electroweak background [$\Delta A(N_{\rm EW})$], uncertainty from multijet background [$\Delta A(N_{\rm MJ})$], uncertainty from charge misidentification [$\Delta A(g)$], uncertainty from ratio of positive and negative muon efficiencies [$\Delta A(k)$], uncertainty from solenoid weighting [ΔA(scl)], uncertainty from smearing correction [$\Delta A(a)$], and total uncertainty of the corrected CP-folded asymmetry [$\Delta A^{*}_{\rm CP}$]. All uncertainties have been multiplied by 100.

$<\eta>$	$\Delta A(N_{\rm data})$	$\Delta A(N_{\rm EW})$	$\Delta A(N_{\rm MJ})$	$\Delta A(g)$	$\Delta A(k)$	ΔA(scl)	$\Delta A(a)$	$\Delta A^{*}_{\rm CP}$
0.10	0.3045	0.003	0.007	0.002	0.012	0.0079	0.124	0.329
0.30	0.3235	0.007	0.027	0.006	0.024	0.0050	0.157	0.361
0.50	0.3129	0.006	0.032	0.007	0.057	0.0044	0.406	0.517
0.71	0.3144	0.041	0.039	0.013	0.088	0.0091	0.344	0.478
0.89	0.3237	0.035	0.053	0.010	0.105	0.0085	0.225	0.413
1.11	0.2868	0.046	0.073	0.013	0.083	0.0077	0.610	0.685
1.30	0.2334	0.079	0.082	0.010	0.094	0.0044	0.409	0.493
1.49	0.2640	0.077	0.097	0.016	0.145	0.0075	0.398	0.514

CHAPTER 5

RESULTS AND CONCLUSIONS

5.1 Combined results for Run IIa and Run IIb

In this section, we combine the measurement results of Run IIa and Run IIb. The corrected asymmetries for Run IIa and Run IIb are compared in Figures 5.1 and 5.2. The figures show that the Run IIa and Run IIb asymmetries are consistent with each other.

The combined asymmetry is the weighted average of the Run IIa and Run IIb asymmetries:

$$A^* = \frac{1}{w}\sum_{i=1}^{2}(w_i A_i^*) \tag{5.1}$$

$$\Delta A^* = \frac{1}{\sqrt{w}} \tag{5.2}$$

where $w_i = 1/\Delta A_i^{*2}$ and $w = \sum_{i=1}^{2} w_i$. $A_{1,2}^*$ and $\Delta A_{1,2}^*$ are the corrected asymmetries and their associated total uncertainties from Run IIa and Run IIb.

We compare the muon charge asymmetry to the theory prediction generated by RESBOS+PHOTOS NLO [50, 51] with CTEQ6.6. The RESBOS generator has gluon resummation at low W boson p_T and NLO perturbative QCD calculations at high W boson p_T. PHOTOS is used to correct for QED final state radiation. Theory predictions with newer PDFs, CT10 and MSTW2008, are generated by POWHEG+PYTHIA NLO [54, 46]. After being generated from POWHEG, the $W \to \mu\nu$ events are passed to PYTHIA 6.4 to generate the parton shower.

The uncertainty band of the CTEQ6.6 theory curve is calculated from the 44 eigenvectors as [52]:

$$\Delta A^{\pm} = \sqrt{\sum_{i=1}^{n}\left[A(a_i^{\pm}) - A_0\right]^2} \tag{5.3}$$

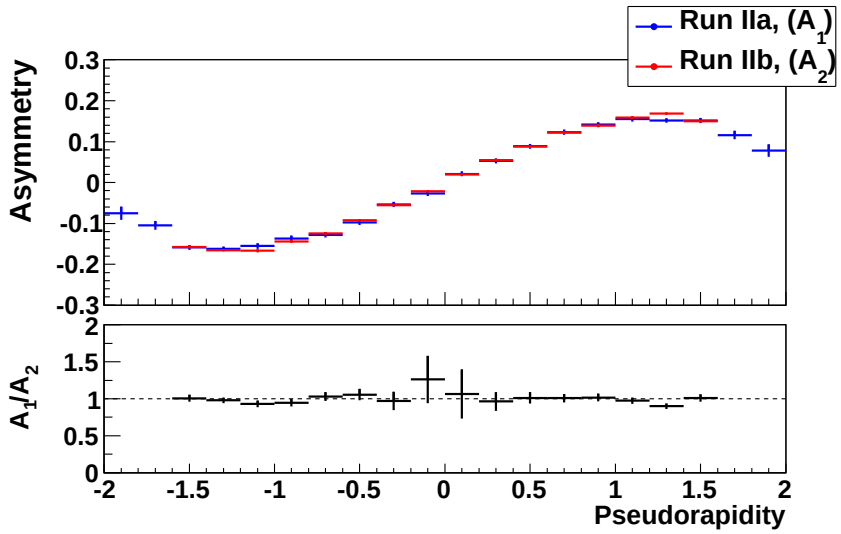

(a) $p_T > 25$ GeV, $\not\!\!E_T > 25$ GeV

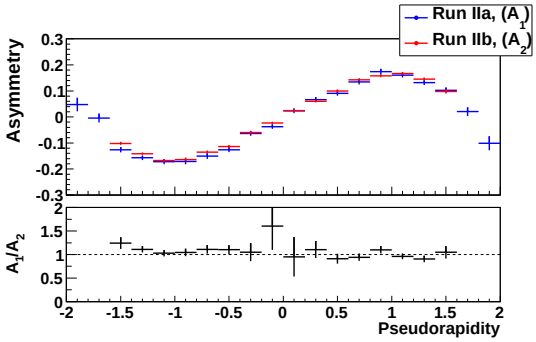

(b) $25 < p_T < 35$ GeV, $\not\!\!E_T > 25$ GeV

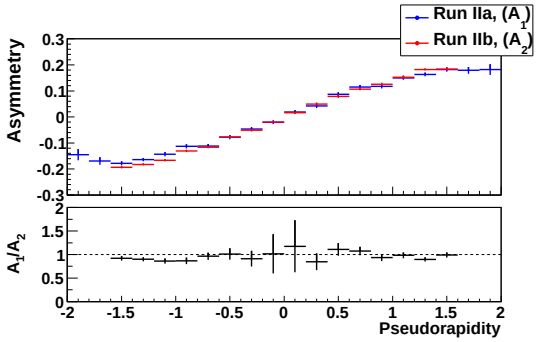

(c) $p_T > 35$ GeV, $\not\!\!E_T > 25$ GeV

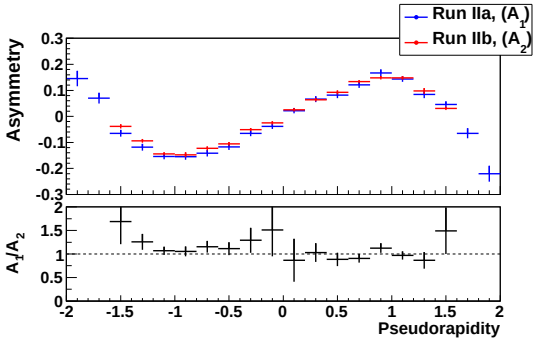

(d) $25 < p_T < 35$ GeV, $25 < \not\!\!E_T < 35$ GeV

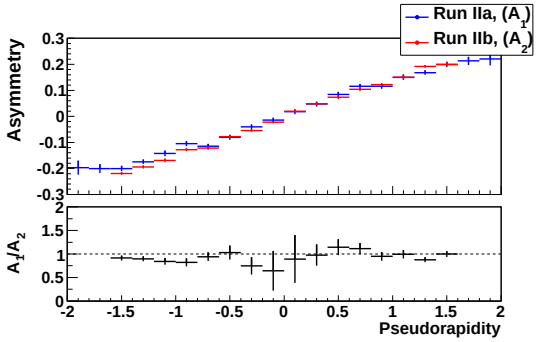

(e) $p_T > 35$ GeV, $\not\!\!E_T > 35$ GeV

Figure 5.1: Muon charge asymmetry as a function of pseudorapidity for Run IIa (blue) and Run IIb (red).

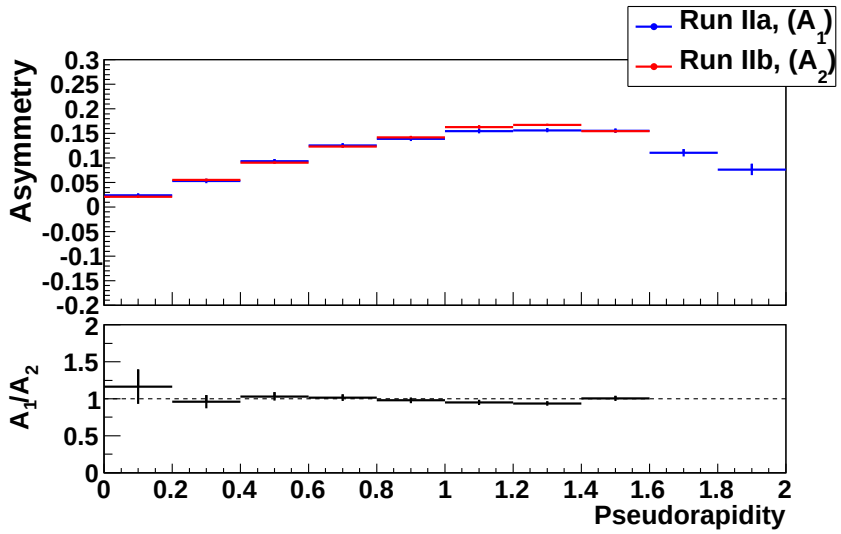

(a) $p_T > 25$ GeV, $\not\!\!E_T > 25$ GeV

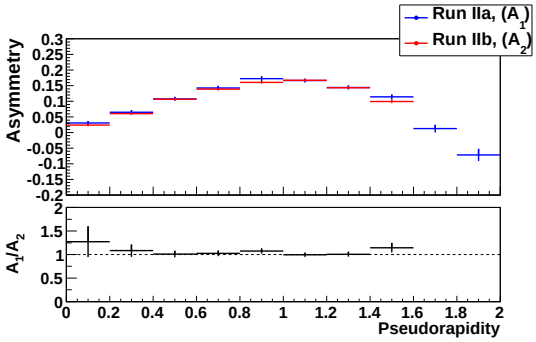

(b) $25 < p_T < 35$ GeV, $\not\!\!E_T > 25$ GeV

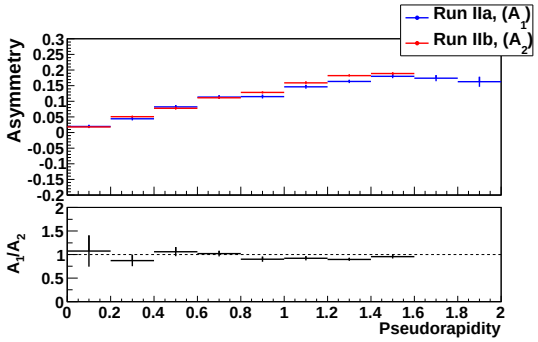

(c) $p_T > 35$ GeV, $\not\!\!E_T > 25$ GeV

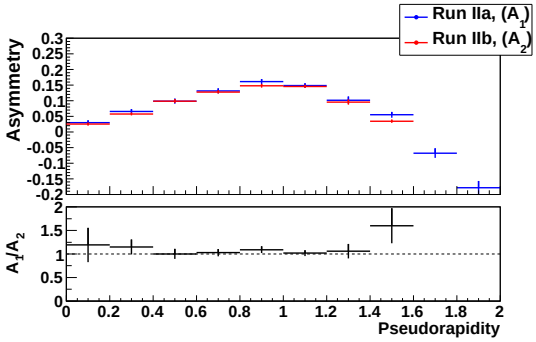

(d) $25 < p_T < 35$ GeV, $25 < \not\!\!E_T < 35$ GeV

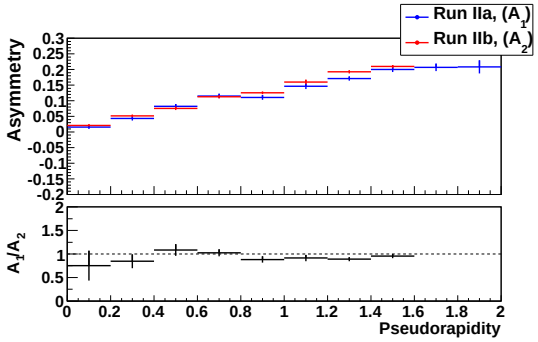

(e) $p_T > 35$ GeV, $\not\!\!E_T > 35$ GeV

Figure 5.2: CP folded asymmetry as a function of pseudorapidity for Run IIa (blue) and Run IIb (red).

where A_0 is the lepton charge asymmetry for the central PDF set, $A(a_i)$ is the asymmetry for the PDF set i, $n = 22$, a_i^+ and a_i^- are the displaced points where $A > A_0$ and $A < A_0$, respectively.

5.2 Conclusion

We have measured the muon charge asymmetry from $W \to \mu\nu$ decay using 7.3 fb^{-1} of data collected with the DØ detector. Figures 5.3, 5.5, and 5.7 show the comparison of the muon charge asymmetry (A_μ) to the electron charge asymmetry (A_e), the MC predictions using the CTEQ6.6, the CT10, and the MSTW2008 PDFs. Figures 5.4, 5.6, and 5.8 show the comparison for the CP-folded asymmetries. The values of the muon and electron asymmetries, as well as the theory predictions are displayed in Tables 5.2 to 5.4.

The electron charge asymmetry is consistent with the muon charge asymmetry. The χ^2/dof comparing the muon and electron charge asymmetries are 1.14, 0.87, and 1.03 for $p_T^\ell > 25$ GeV, $25 < p_T^\ell < 35$ GeV, and $p_T^\ell > 35$ GeV, respectively. Except for the highest muon $|\eta|$ bin, the uncertainty in the muon channel is smaller than the uncertainty in the electron channel.

The lepton asymmetries in the two channels are close to the central value of the CTEQ6.6 prediction in the inclusive p_T^ℓ bin. However, both are higher than the the theory prediction at low p_T^ℓ, and lower at high p_T^ℓ. It is important to notice that for the $25 < p_T^\ell < 35$ and $p_T^\ell > 35$ bins, the lepton charge asymmetry strongly depends on the momentum of the W boson.

To check effects from the disagreement between data and MC W p_T's, we reweight the MC to match W p_T distribution seen in the data at the reconstruction level (see Appendix D). The difference between the MC asymmetries before and after reweighting is smaller than the discrepancies between the muon charge asymmetry results and the theory predictions. Therefore, no action is taken to improve the W p_T modeling in the MC.

This is the lepton charge asymmetry measurement with smallest uncertainties from a $p\overline{p}$ collider. Except at the highest η bins where the muon channel has fewer events, the uncertainties in the muon channel are smaller than those of electron channel. In each η bin, the precision of the CP folded asymmetry varies from 0.2% to 1.2% for $p_T > 25$ GeV,

(0.4–2.0)% for $25 < p_T < 35$ GeV, and (0.3–1.7)% for $p_T > 35$ GeV. The good statistical precision of this measurement and the agreement between the two channels will be very useful in improving constraints for future PDFs fits.

Table 5.1: Combined muon charge asymmetry for $p_{T,\ell} > 25$ GeV and $\not\!\!E_T > 25$ GeV: the mean value of η ($< \eta >$), muon charge asymmetry [A_μ], electron charge asymmetry [A_e], and asymmetry with the CTEQ6.6 PDF sets [A(CTEQ6.6)]. All asymmetry values are multiplied by 100.

$< \eta >$	A_μ	A_e	A(CTEQ6.6)
-1.88	$-7.52 \pm 1.53 \pm 0.53$	$-6.90 \pm 0.90 \pm 0.60$	$-7.87^{+2.71}_{-2.54}$
-1.66	$-10.47 \pm 1.01 \pm 0.43$	$-10.80 \pm 0.70 \pm 0.60$	$-12.65^{+2.58}_{-2.24}$
-1.49	$-15.80 \pm 0.23 \pm 0.27$	$-13.20 \pm 0.90 \pm 0.70$	$-15.82^{+1.96}_{-1.96}$
-1.30	$-16.49 \pm 0.20 \pm 0.28$		$-16.72^{+1.84}_{-1.72}$
-1.11	$-16.47 \pm 0.23 \pm 0.39$	$-16.00 \pm 0.90 \pm 0.60$	$-16.30^{+1.88}_{-1.79}$
-0.89	$-14.30 \pm 0.26 \pm 0.28$	$-14.10 \pm 0.60 \pm 0.40$	$-14.74^{+1.48}_{-1.31}$
-0.71	$-12.50 \pm 0.26 \pm 0.22$	$-12.30 \pm 0.50 \pm 0.40$	$-12.25^{+1.26}_{-1.15}$
-0.50	$-9.36 \pm 0.25 \pm 0.20$	$-8.60 \pm 0.50 \pm 0.40$	$-9.26^{+0.84}_{-1.16}$
-0.30	$-5.49 \pm 0.26 \pm 0.21$	$-6.00 \pm 0.60 \pm 0.40$	$-5.66^{+0.77}_{-0.75}$
-0.10	$-2.26 \pm 0.25 \pm 0.14$	$-1.70 \pm 0.60 \pm 0.40$	$-1.96^{+0.31}_{-0.57}$
0.10	$2.00 \pm 0.25 \pm 0.14$	$1.70 \pm 0.60 \pm 0.40$	$1.99^{+0.37}_{-0.53}$
0.30	$5.42 \pm 0.27 \pm 0.17$	$5.20 \pm 0.60 \pm 0.40$	$5.69^{+0.72}_{-0.80}$
0.50	$8.79 \pm 0.25 \pm 0.19$	$8.00 \pm 0.50 \pm 0.40$	$9.22^{+1.04}_{-0.99}$
0.71	$12.25 \pm 0.25 \pm 0.24$	$13.10 \pm 0.50 \pm 0.40$	$12.21^{+1.44}_{-1.42}$
0.89	$13.97 \pm 0.26 \pm 0.21$	$14.40 \pm 0.60 \pm 0.50$	$14.78^{+1.40}_{-1.61}$
1.11	$15.81 \pm 0.23 \pm 0.29$	$14.40 \pm 0.90 \pm 0.70$	$16.29^{+1.78}_{-1.47}$
1.30	$16.52 \pm 0.20 \pm 0.32$	$15.40 \pm 0.80 \pm 0.70$	$16.80^{+1.64}_{-1.70}$
1.49	$15.03 \pm 0.23 \pm 0.29$		$15.73^{+1.95}_{-1.78}$
1.66	$11.62 \pm 0.98 \pm 0.30$	$10.00 \pm 0.70 \pm 0.60$	$12.86^{+2.05}_{-2.32}$
1.88	$7.83 \pm 1.49 \pm 0.42$	$5.80 \pm 0.80 \pm 0.60$	$7.79^{+2.87}_{-2.66}$

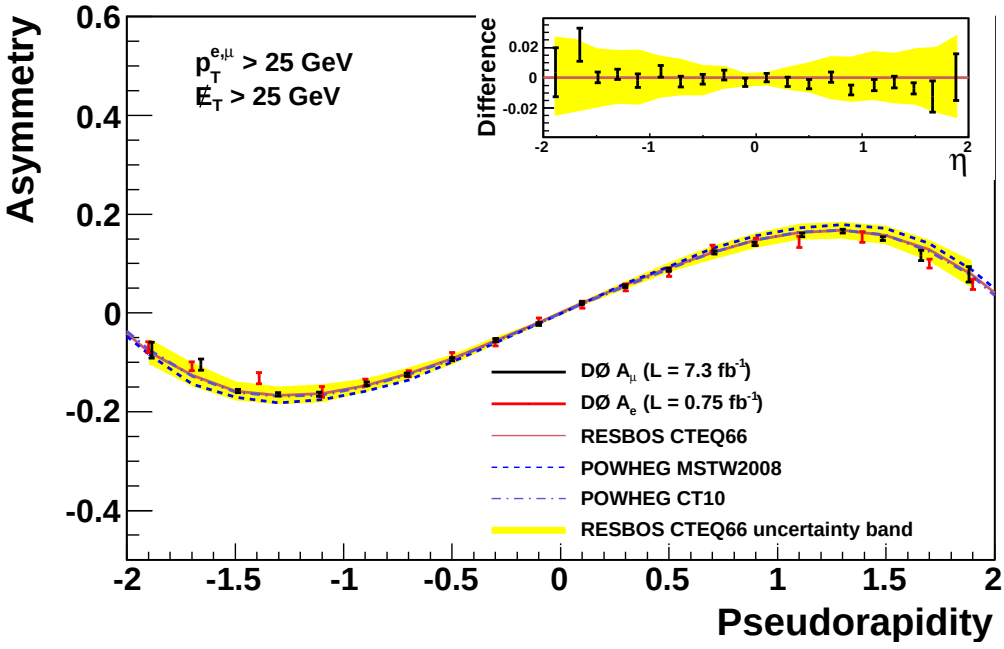

(a) Lepton charge asymmetry

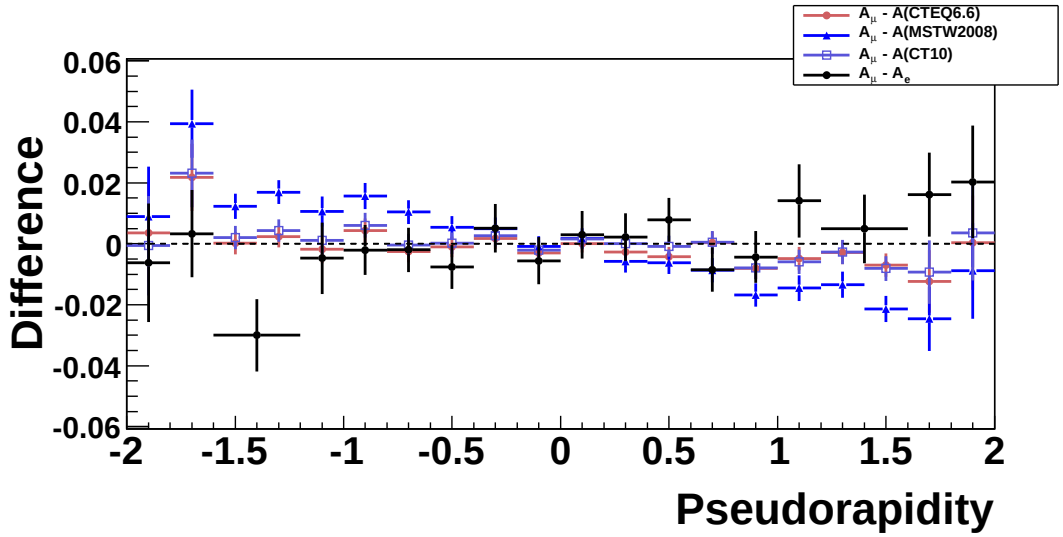

(b) Asymmetry difference

Figure 5.3: (a) Lepton charge asymmetry and (b) the difference between A_μ and the other asymmetries for $p_T^{e,\mu} > 25$ GeV and $\not\!\!E_T > 25$ GeV. In (a), the black points show the muon charge asymmetry with 7.3 fb^{-1} of data. The red points show the electron charge asymmetry with 0.75 fb^{-1} of data. The brown line and yellow band are the central value and uncertainty band of the RESBOS+CTEQ6.6 prediction. The blue dashed line is the POWHEG+MSTW2008 prediction, and the purple dashed-dot line is the POWHEG+CT10 prediction. The upper right window in (a) shows the difference between the muon charge asymmetry and the central value of CTEQ6.6.

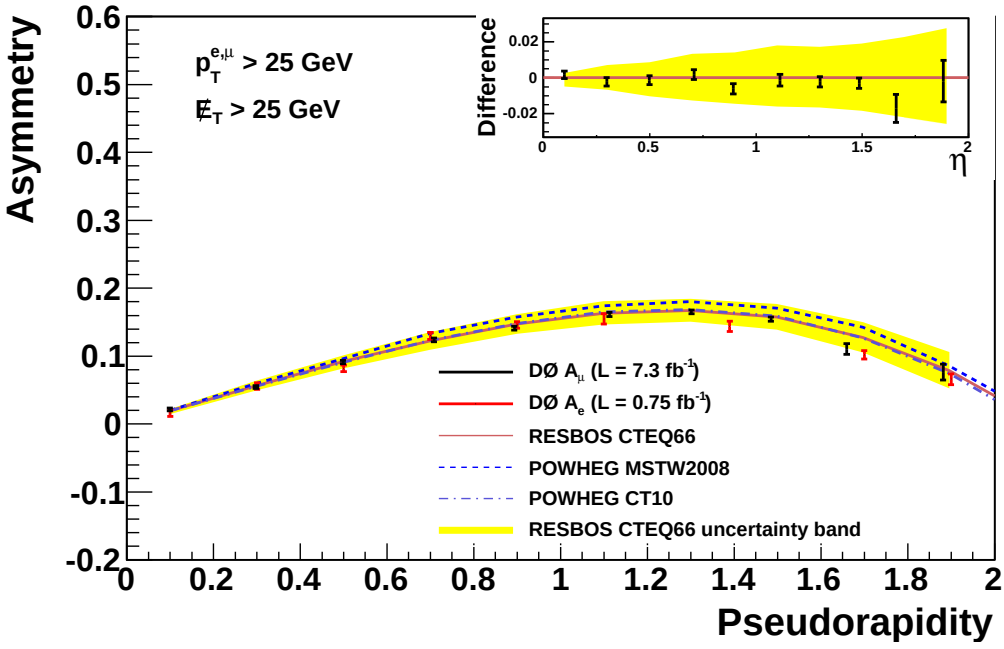

(a) CP folded asymmetry

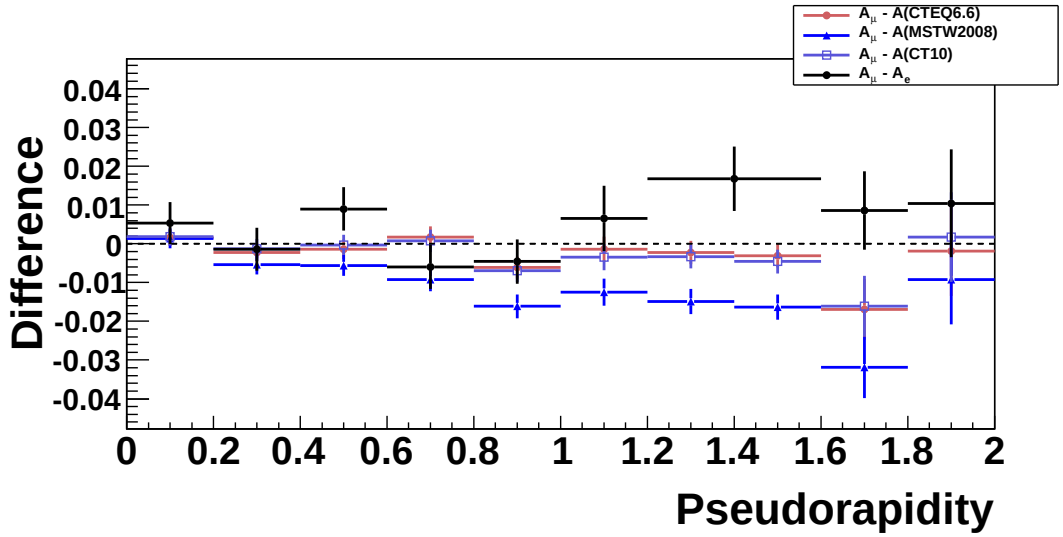

(b) Asymmetry difference

Figure 5.4: (a) CP folded asymmetry and (b) the difference between $A_{\mathrm{CP},\mu}$ and the other asymmetries for $p_T^{e,\mu} > 25$ GeV and $\not\!\!E_T > 25$ GeV. In (a), the black points show the muon charge asymmetry with 7.3 fb^{-1} of data. The red points show the electron charge asymmetry with 0.75 fb^{-1} of data. The brown line and yellow band are the central value and uncertainty band of the RESBOS+CTEQ6.6 prediction. The blue dashed line is the POWHEG+MSTW2008 prediction, and the purple dashed-dot line is the POWHEG+CT10 prediction. The upper right window in (a) shows the difference between the muon charge asymmetry and the central value of CTEQ6.6.

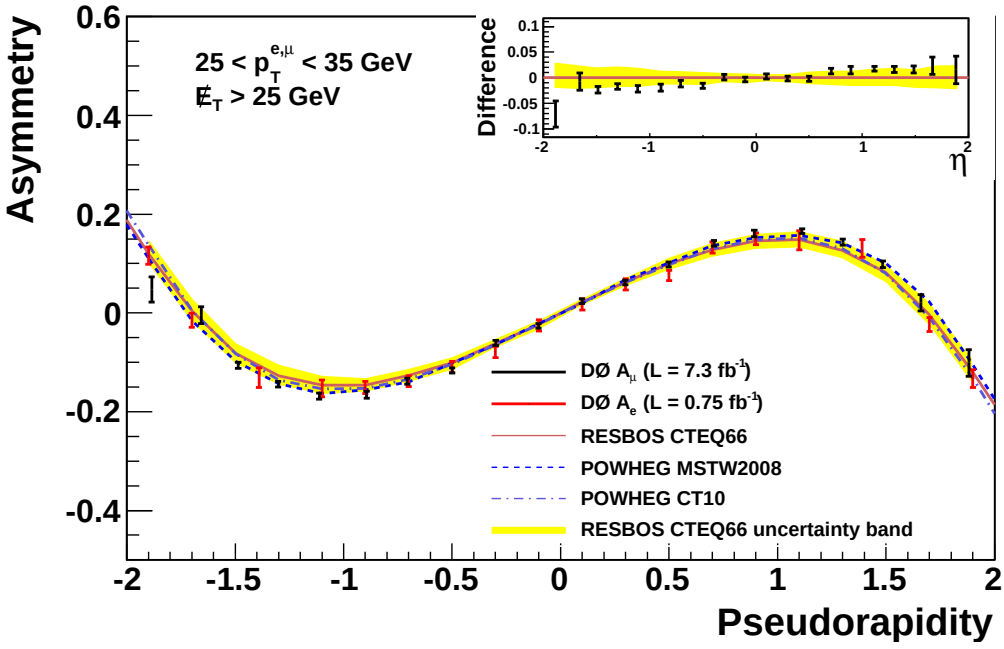

(a) Lepton charge asymmetry

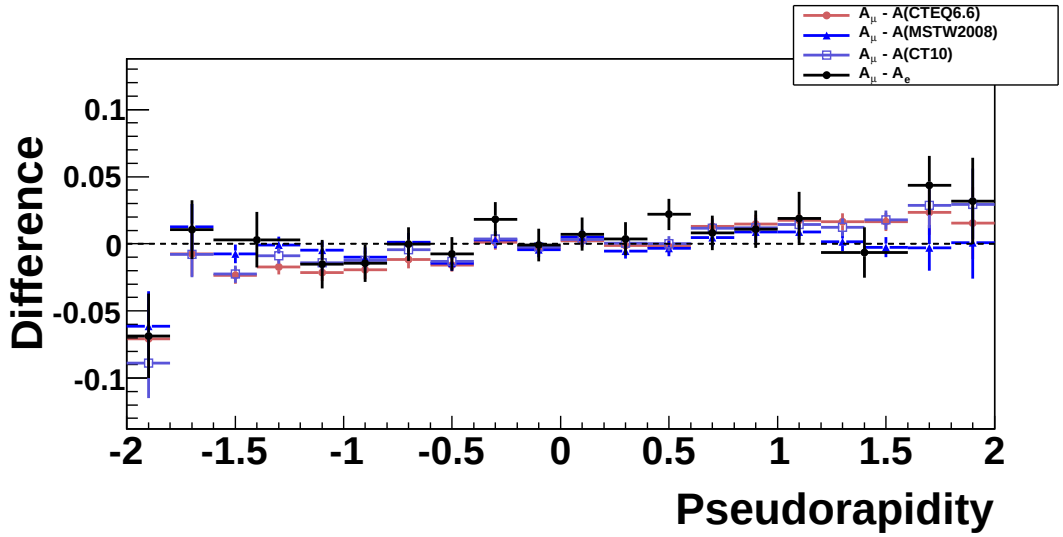

(b) Asymmetry difference

Figure 5.5: (a) Lepton charge asymmetry and (b) the difference between A_μ and the other asymmetries for $25 < p_T^{e,\mu} < 35$ GeV and $\not\!\!E_T > 25$ GeV. In (a), the black points show the muon charge asymmetry with 7.3 fb^{-1} of data. The red points show the electron charge asymmetry with 0.75 fb^{-1} of data. The brown line and yellow band are the central value and uncertainty band of the RESBOS+CTEQ6.6 prediction. The blue dashed line is the POWHEG+MSTW2008 prediction, and the purple dashed-dot line is the POWHEG+CT10 prediction. The upper right window in (a) shows the difference between the muon charge asymmetry and the central value of CTEQ6.6.

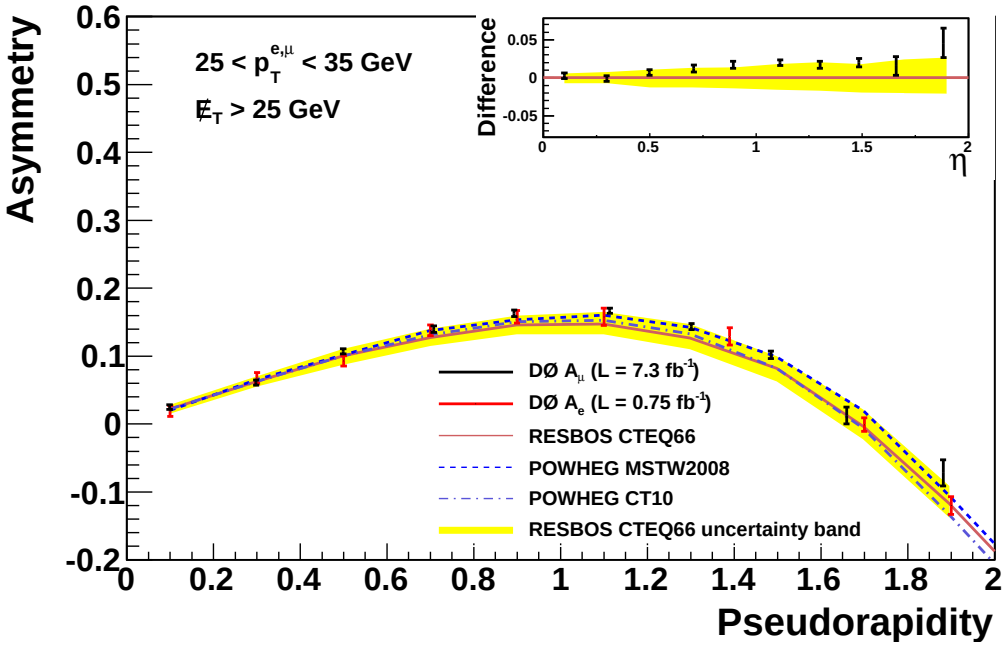

(a) CP folded asymmetry

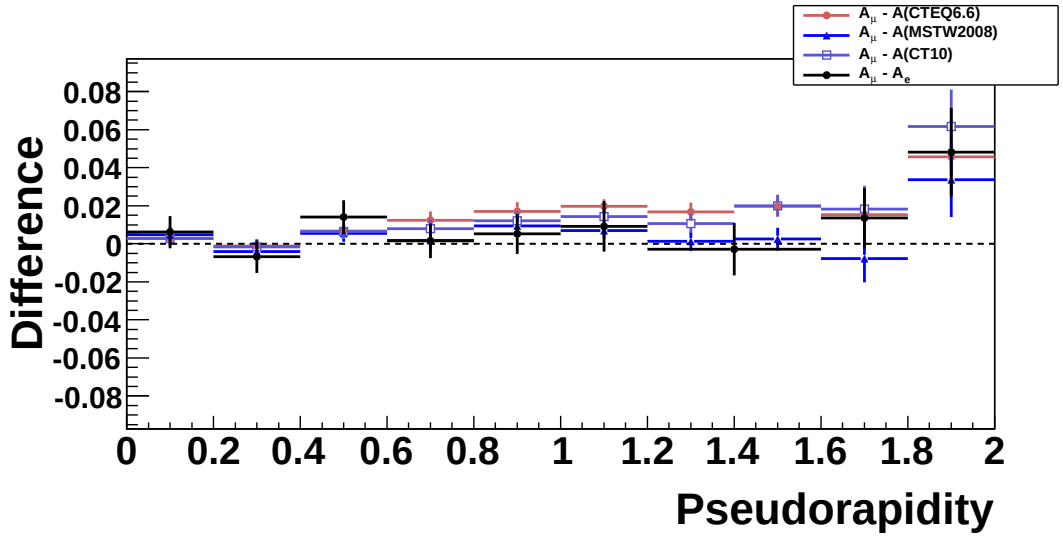

(b) Asymmetry difference

Figure 5.6: (a) CP folded asymmetry and (b) the difference between $A_{\mathrm{CP},\mu}$ and the other asymmetries for $25 < p_T^{e,\mu} < 35$ GeV and $\not\!\!E_T > 25$ GeV. In (a), the black points show the muon charge asymmetry with 7.3 fb^{-1} of data. The red points show the electron charge asymmetry with 0.75 fb^{-1} of data. The brown line and yellow band are the central value and uncertainty band of the RESBOS+CTEQ6.6 prediction. The blue dashed line is the POWHEG+MSTW2008 prediction, and the purple dashed-dot line is the POWHEG+CT10 prediction. The upper right window in (a) shows the difference between the muon charge asymmetry and the central value of CTEQ6.6.

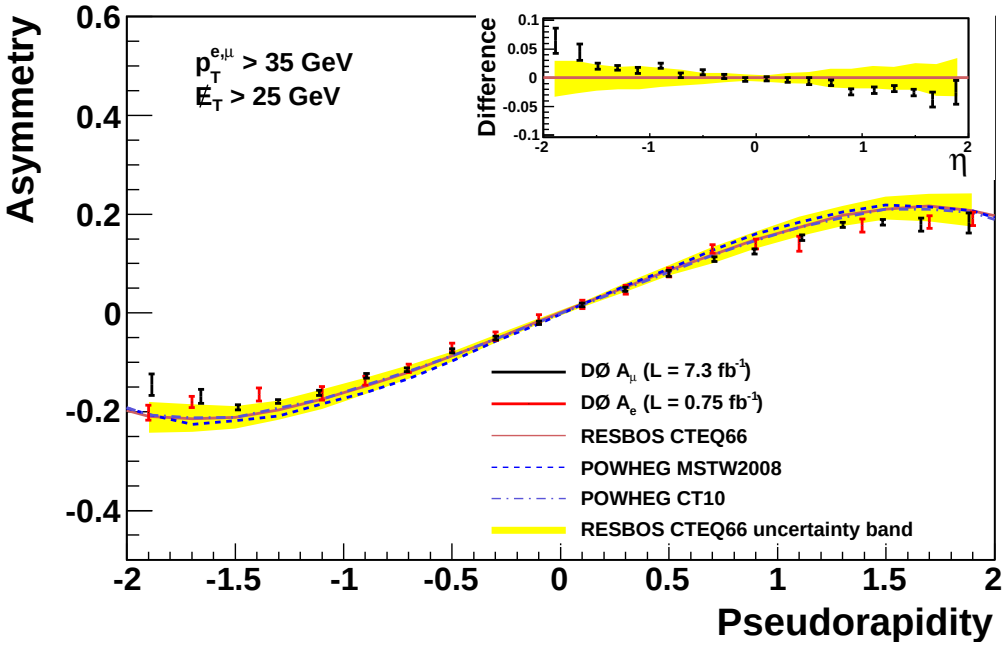

(a) Lepton charge asymmetry

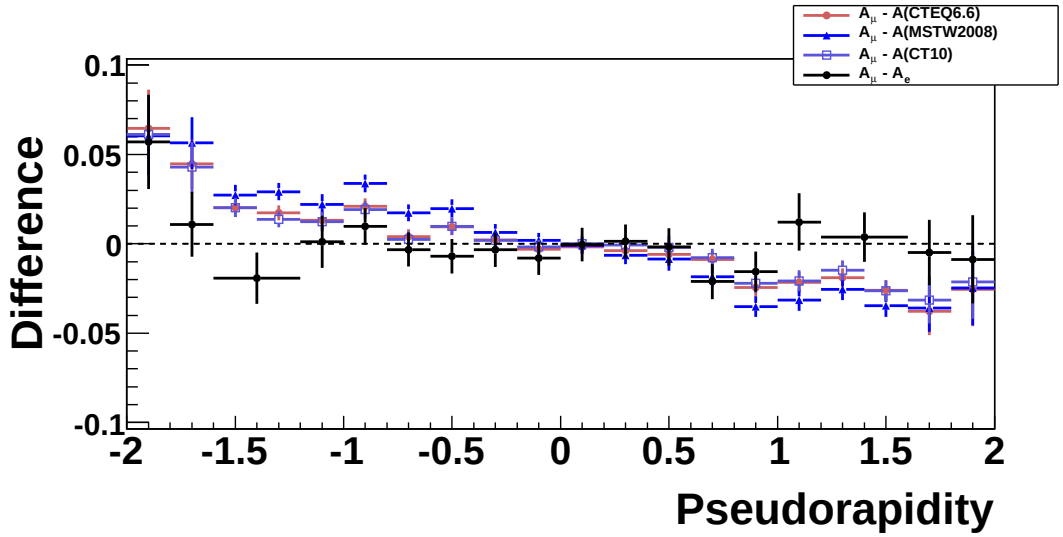

(b) Asymmetry difference

Figure 5.7: (a) Lepton charge asymmetry and (b) the difference between A_μ and the other asymmetries for $p_T^{e,\mu} > 35$ GeV and $\not\!\!E_T > 25$ GeV. In (a), the black points show the muon charge asymmetry with 7.3 fb^{-1} of data. The red points show the electron charge asymmetry with 0.75 fb^{-1} of data. The brown line and yellow band are the central value and uncertainty band of the RESBOS+CTEQ6.6 prediction. The blue dashed line is the POWHEG+MSTW2008 prediction, and the purple dashed-dot line is the POWHEG+CT10 prediction. The upper right window in (a) shows the difference between the muon charge asymmetry and the central value of CTEQ6.6.

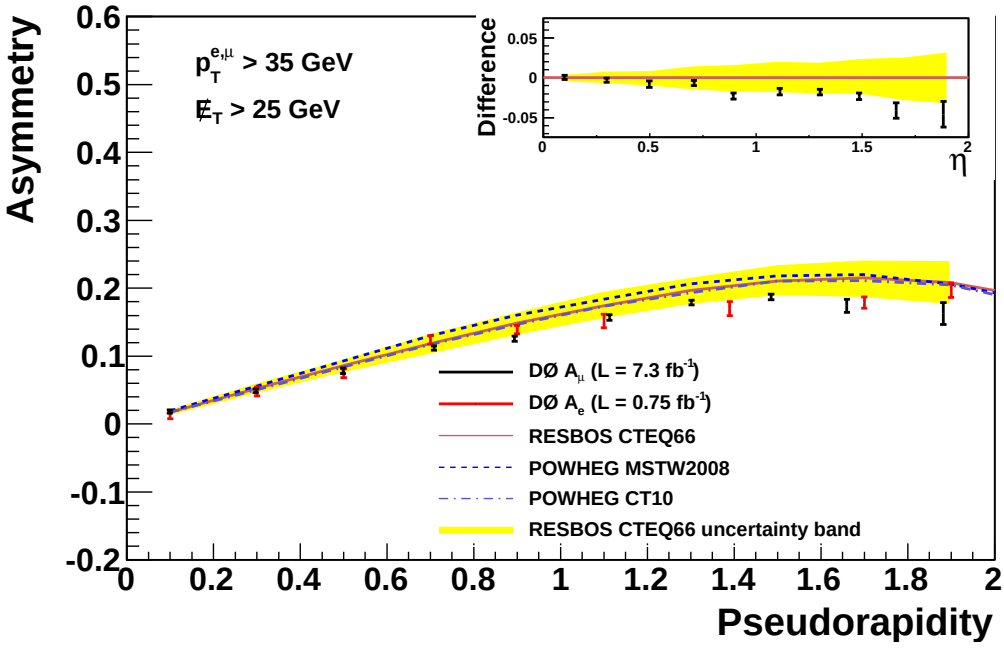

(a) CP folded asymmetry

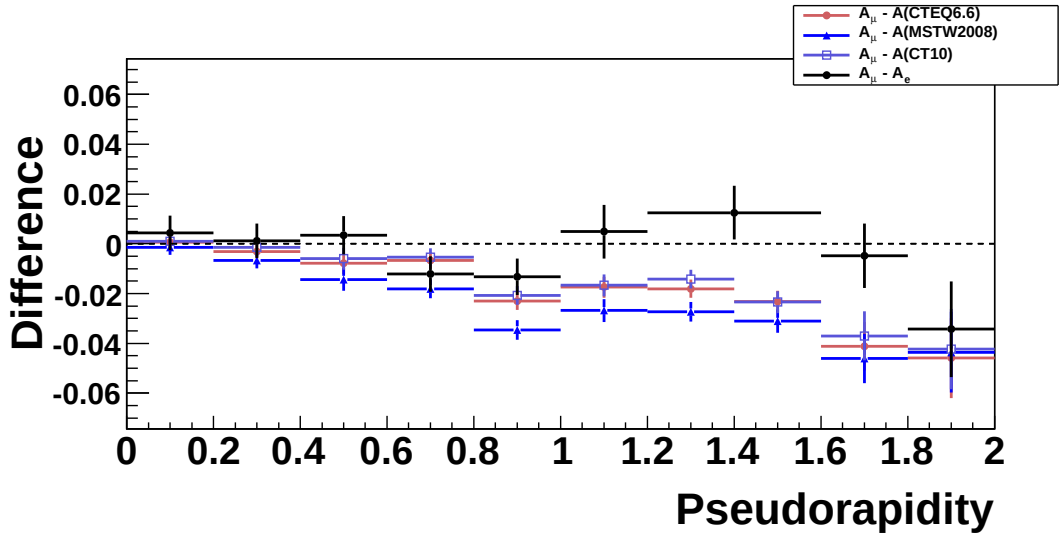

(b) Asymmetry difference

Figure 5.8: (a) CP folded asymmetry and (b) the difference between $A_{\mathrm{CP},\mu}$ and the other asymmetries for $p_T^{e,\mu} > 35$ GeV and $\not\!\!E_T > 25$ GeV. In (a), the black points show the muon charge asymmetry with 7.3 fb^{-1} of data. The red points show the electron charge asymmetry with 0.75 fb^{-1} of data. The brown line and yellow band are the central value and uncertainty band of the RESBOS+CTEQ6.6 prediction. The blue dashed line is the POWHEG+MSTW2008 prediction, and the purple dashed-dot line is the POWHEG+CT10 prediction. The upper right window in (a) shows the difference between the muon charge asymmetry and the central value of CTEQ6.6.

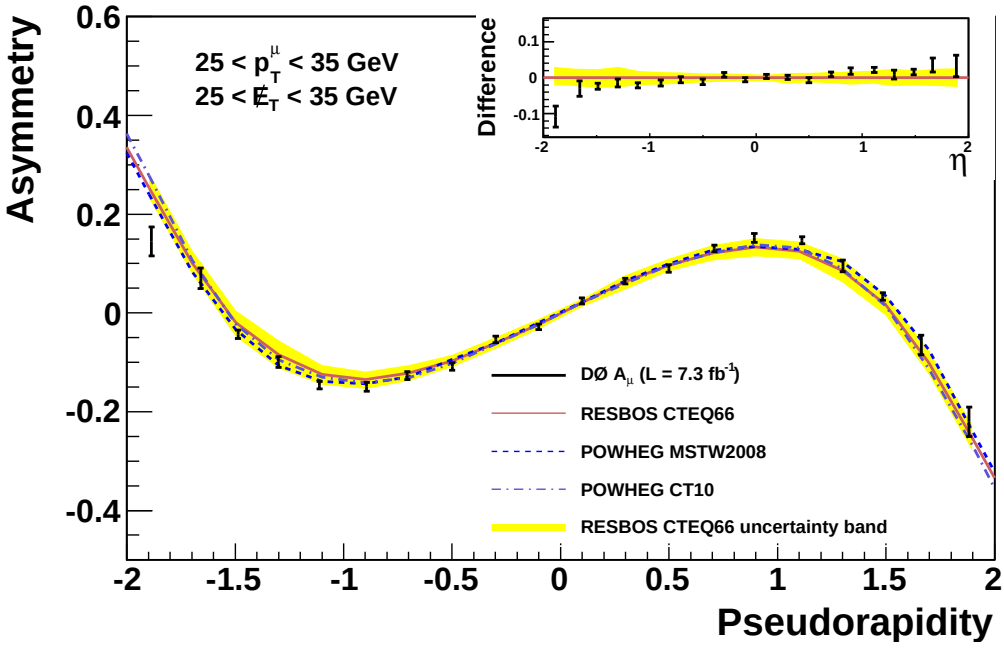

(a) Muon charge asymmetry

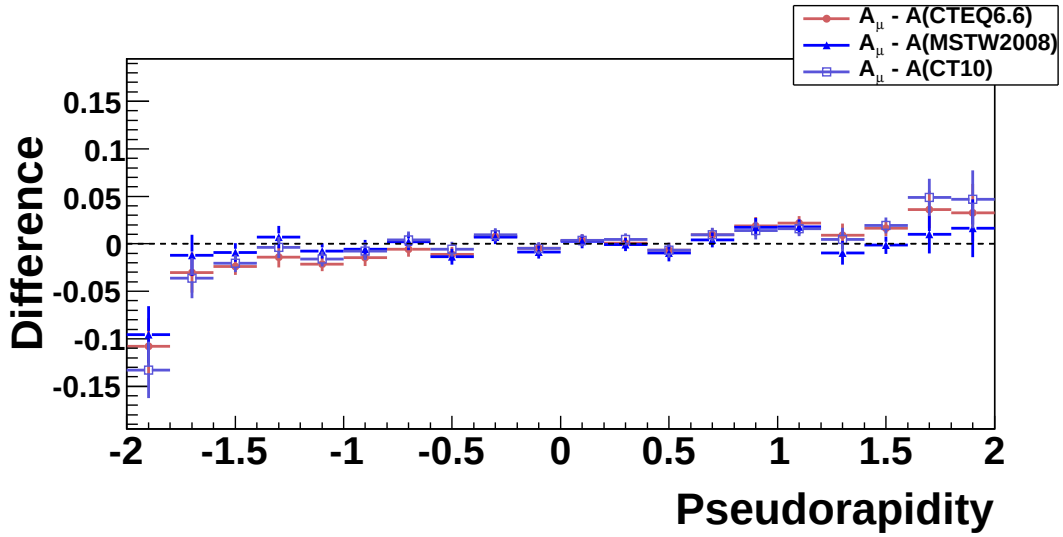

(b) Asymmetry difference

Figure 5.9: (a) Combined Run IIa and Run IIb muon charge asymmetry and (b) the difference between A_μ and the other asymmetries for $25 < p_T < 35$ GeV and $25 < \not\!\!E_T < 35$ GeV. In (a), the black points show the muon charge asymmetry with 7.3 fb^{-1} of data. The brown line and yellow band are the central value and uncertainty band of the RESBOS+CTEQ6.6 prediction. The blue dashed line is the POWHEG+MSTW2008 prediction, and the purple dashed-dot line is the POWHEG+CT10 prediction. The upper right window in (a) shows the difference between the muon charge asymmetry and the central value of the RESBOS+CTEQ6.6 prediction.

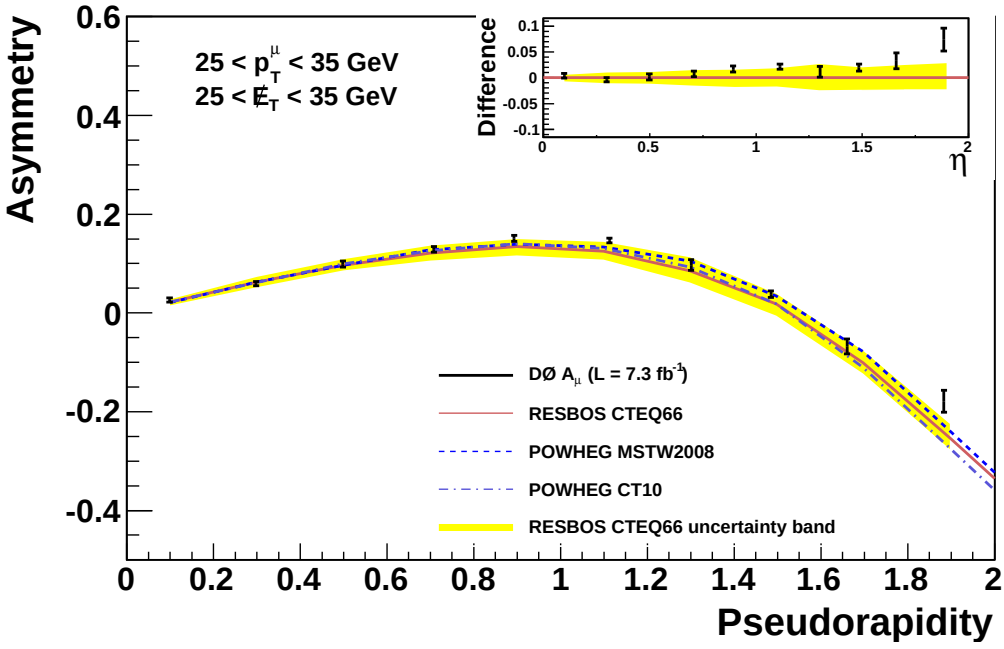

(a) CP folded asymmetry

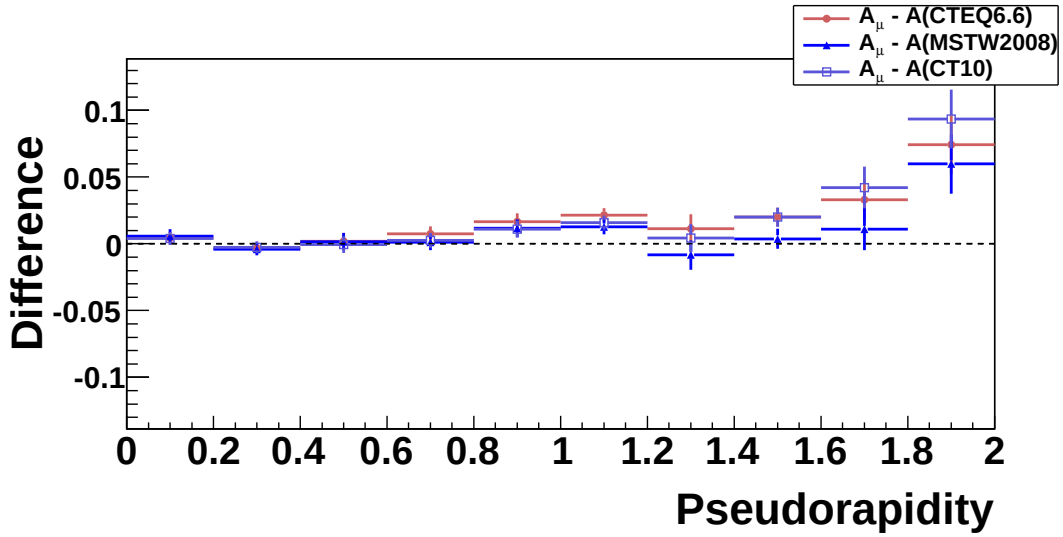

(b) Asymmetry difference

Figure 5.10: (a) CP folded asymmetry and (b) the difference between $A_{\mathrm{CP},\mu}$ and the other asymmetries for $25 < p_T < 35$ GeV and $25 < \not{E}_T < 35$ GeV. In (a), the black points show the muon charge asymmetry with 7.3 fb^{-1} of data. The brown line and yellow band are the central value and uncertainty band of the RESBOS+CTEQ6.6 prediction. The blue dashed line is the POWHEG+MSTW2008 prediction, and the purple dashed-dot line is the POWHEG+CT10 prediction. The upper right window in (a) shows the difference between the muon charge asymmetry and the central value of CTEQ6.6.

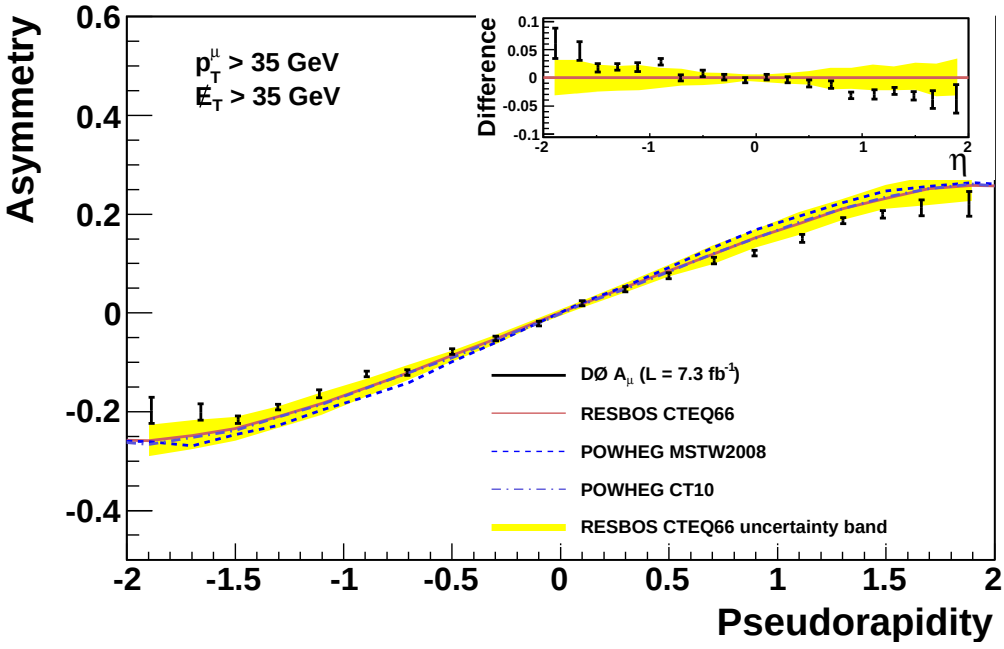

(a) Muon charge asymmetry

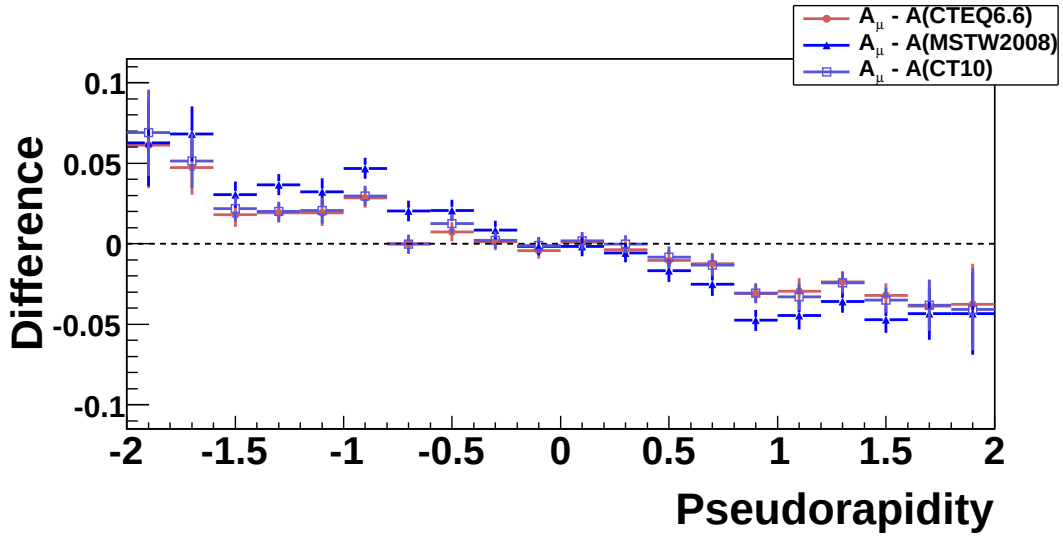

(b) Asymmetry difference

Figure 5.11: (a) Combined Run IIa and Run IIb muon charge asymmetry and (b) the difference between A_μ and the other asymmetries for $p_T > 35$ GeV and $\not{E}_T > 35$ GeV. In (a), the black points show the muon charge asymmetry with 7.3 fb^{-1} of data. The brown line and yellow band are the central value and uncertainty band of the RESBOS+CTEQ6.6 prediction. The blue dashed line is the POWHEG+MSTW2008 prediction, and the purple dashed-dot line is the POWHEG+CT10 prediction. The upper right window in (a) shows the difference between the muon charge asymmetry and the central value of CTEQ6.6.

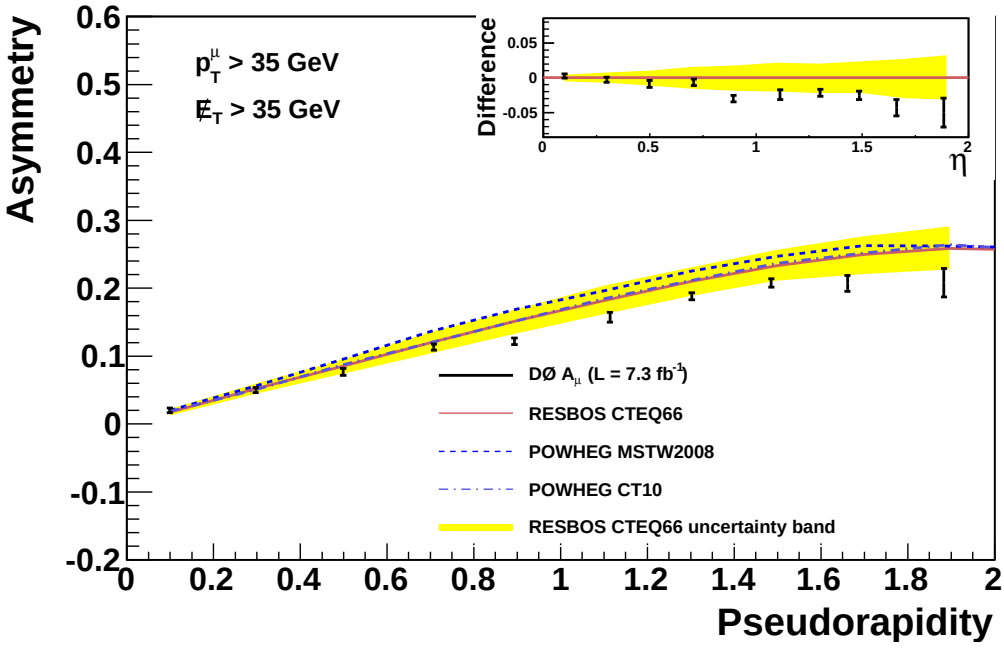

(a) CP folded asymmetry

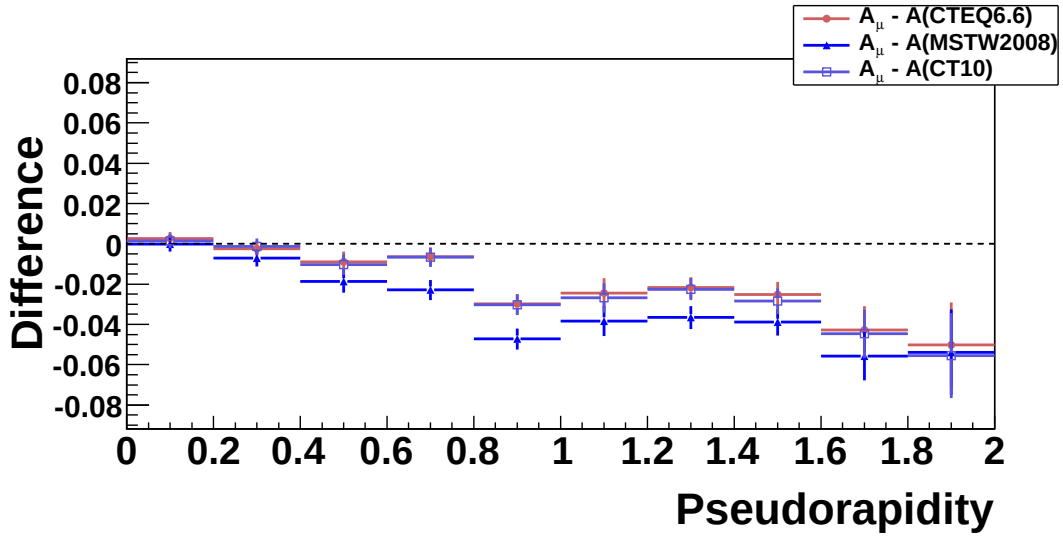

(b) Asymmetry difference

Figure 5.12: (a) CP folded asymmetry and (b) the difference between $A_{\mathrm{CP},\mu}$ and the other asymmetries for $p_T > 35$ GeV and $\not\!\!E_T > 35$ GeV. In (a), the black points show the muon charge asymmetry with 7.3 fb^{-1} of data. The brown line and yellow band are the central value and uncertainty band of the RESBOS+CTEQ6.6 prediction. The blue dashed line is the POWHEG+MSTW2008 prediction, and the purple dashed-dot line is the POWHEG+CT10 prediction. The upper right window in (a) shows the difference between the muon charge asymmetry and the central value of CTEQ6.6.

Table 5.2: Combined CP folded asymmetry for $p_{T,\ell} > 25$ GeV and $\not\!\!E_T > 25$ GeV: the mean value of η ($< \eta >$), muon charge asymmetry [$A_{\mathrm{CP},\mu}$], electron charge asymmetry [$A_{\mathrm{CP,e}}$], and asymmetry with the CTEQ6.6 PDF sets [A(CTEQ6.6)]. All asymmetry values are multiplied by 100.

$< \eta >$	$A_{\mathrm{CP},\mu}$	$A_{\mathrm{CP,e}}$	A(CTEQ6.6)
0.10	$2.13 \pm 0.17 \pm 0.12$	$1.60 \pm 0.40 \pm 0.30$	$1.97^{+0.28}_{-0.48}$
0.30	$5.46 \pm 0.18 \pm 0.14$	$5.60 \pm 0.40 \pm 0.30$	$5.68^{+0.71}_{-0.67}$
0.50	$9.10 \pm 0.18 \pm 0.16$	$8.20 \pm 0.40 \pm 0.30$	$9.24^{+0.86}_{-1.02}$
0.71	$12.41 \pm 0.18 \pm 0.20$	$13.00 \pm 0.40 \pm 0.30$	$12.23^{+1.33}_{-1.26}$
0.89	$14.14 \pm 0.18 \pm 0.21$	$14.60 \pm 0.40 \pm 0.30$	$14.76^{+1.42}_{-1.43}$
1.11	$16.15 \pm 0.16 \pm 0.28$	$15.50 \pm 0.60 \pm 0.50$	$16.29^{+1.81}_{-1.61}$
1.30	$16.53 \pm 0.14 \pm 0.26$	$14.40 \pm 0.60 \pm 0.50$	$16.76^{+1.71}_{-1.66}$
1.49	$15.47 \pm 0.16 \pm 0.24$		$15.78^{+1.90}_{-1.84}$
1.66	$11.06 \pm 0.70 \pm 0.33$	$10.20 \pm 0.50 \pm 0.40$	$12.75^{+2.26}_{-2.20}$
1.88	$7.64 \pm 1.07 \pm 0.42$	$6.60 \pm 0.60 \pm 0.50$	$7.83^{+2.75}_{-2.56}$

Table 5.3: Combined CP folded asymmetry for $25 < p_{T,\ell} < 35$ GeV and $\not\!\!E_T > 25$ GeV: the mean value of η ($< \eta >$), muon charge asymmetry [$A_{\mathrm{CP},\mu}$], electron charge asymmetry [$A_{\mathrm{CP,e}}$], and asymmetry with the CTEQ6.6 PDF sets [A(CTEQ6.6)]. All asymmetry values are multiplied by 100.

$< \eta >$	$A_{\mathrm{CP},\mu}$	$A_{\mathrm{CP,e}}$	A(CTEQ6.6)
0.10	$2.51 \pm 0.27 \pm 0.22$	$1.90 \pm 0.60 \pm 0.50$	$2.24^{+0.59}_{-0.71}$
0.30	$6.13 \pm 0.28 \pm 0.23$	$6.80 \pm 0.60 \pm 0.50$	$6.25^{+0.77}_{-0.71}$
0.50	$10.71 \pm 0.28 \pm 0.26$	$9.30 \pm 0.60 \pm 0.50$	$10.03^{+1.07}_{-1.27}$
0.71	$13.96 \pm 0.28 \pm 0.37$	$13.80 \pm 0.60 \pm 0.50$	$12.73^{+1.31}_{-1.26}$
0.89	$16.32 \pm 0.29 \pm 0.38$	$15.80 \pm 0.70 \pm 0.60$	$14.62^{+1.35}_{-1.42}$
1.11	$16.72 \pm 0.26 \pm 0.26$	$15.80 \pm 1.00 \pm 0.80$	$14.75^{+1.77}_{-1.56}$
1.30	$14.37 \pm 0.22 \pm 0.41$	$12.90 \pm 1.00 \pm 0.80$	$12.69^{+2.06}_{-1.68}$
1.48	$10.21 \pm 0.26 \pm 0.48$		$8.22^{+1.78}_{-1.92}$
1.66	$1.25 \pm 1.12 \pm 0.48$	$-0.10 \pm 0.80 \pm 0.60$	$-0.29^{+2.42}_{-1.99}$
1.88	$-7.18 \pm 1.74 \pm 0.86$	$-12.00 \pm 1.00 \pm 0.80$	$-11.75^{+2.67}_{-2.04}$

Table 5.4: Combined CP folded asymmetry for $p_{T,\ell} > 35$ GeV and $\not\!\!E_T > 25$ GeV: the mean value of η ($< \eta >$), muon charge asymmetry [$A_{\mathrm{CP},\mu}$], electron charge asymmetry [$A_{\mathrm{CP,e}}$], and asymmetry with the CTEQ6.6 PDF sets [A(CTEQ6.6)]. All asymmetry values are multiplied by 100.

$< \eta >$	$A_{\mathrm{CP},\mu}$	$A_{\mathrm{CP,e}}$	A(CTEQ6.6)
0.10	$1.84 \pm 0.23 \pm 0.12$	$1.40 \pm 0.50 \pm 0.40$	$1.77^{+0.36}_{-0.45}$
0.30	$4.93 \pm 0.24 \pm 0.13$	$4.80 \pm 0.50 \pm 0.40$	$5.24^{+0.78}_{-0.71}$
0.50	$7.85 \pm 0.23 \pm 0.35$	$7.50 \pm 0.50 \pm 0.40$	$8.64^{+0.85}_{-1.00}$
0.71	$11.19 \pm 0.24 \pm 0.23$	$12.40 \pm 0.50 \pm 0.40$	$11.85^{+1.44}_{-1.42}$
0.89	$12.57 \pm 0.24 \pm 0.26$	$13.90 \pm 0.50 \pm 0.40$	$14.86^{+1.62}_{-1.71}$
1.11	$15.69 \pm 0.21 \pm 0.36$	$15.20 \pm 0.80 \pm 0.60$	$17.43^{+2.03}_{-1.79}$
1.30	$17.89 \pm 0.18 \pm 0.31$	$17.00 \pm 0.80 \pm 0.60$	$19.70^{+1.86}_{-2.00}$
1.49	$18.73 \pm 0.21 \pm 0.37$		$21.05^{+2.34}_{-2.05}$
1.66	$17.42 \pm 0.90 \pm 0.37$	$17.90 \pm 0.60 \pm 0.60$	$21.54^{+2.55}_{-2.81}$
1.88	$16.27 \pm 1.35 \pm 0.87$	$19.70 \pm 0.80 \pm 0.70$	$20.86^{+3.15}_{-3.20}$

Table 5.5: Combined CP folded asymmetry for $25 < p_T < 35$ GeV and $25 < \not\!\!E_T < 35$ GeV: the mean value of η ($< \eta >$), Run IIa asymmetry [A^*_{CP}(Run IIa)], Run IIb asymmetry [A^*_{CP}(Run IIb)], combined asymmetry [A^*_{CP}], and symmetry with the CTEQ6.6 PDF sets [A(CTEQ6.6)]. All values have been multiplied by 100

$< \eta >$	A^*_{CP}(Run IIa)	A^*_{CP}(Run IIb)	A^*_{CP}	A(CTEQ6.6)
0.10	$3.02 \pm 0.69 \pm 0.20$	$2.53 \pm 0.36 \pm 0.32$	$2.63 \pm 0.32 \pm 0.32$	$2.20^{+0.61}_{-0.66}$
0.30	$6.59 \pm 0.73 \pm 0.20$	$5.74 \pm 0.38 \pm 0.21$	$5.92 \pm 0.34 \pm 0.21$	$6.26^{+1.01}_{-1.07}$
0.50	$9.90 \pm 0.72 \pm 0.41$	$9.88 \pm 0.37 \pm 0.50$	$9.88 \pm 0.33 \pm 0.50$	$9.69^{+1.16}_{-1.10}$
0.71	$13.16 \pm 0.74 \pm 0.41$	$12.81 \pm 0.38 \pm 0.33$	$12.88 \pm 0.34 \pm 0.41$	$12.13^{+1.49}_{-1.48}$
0.89	$16.13 \pm 0.74 \pm 0.40$	$14.79 \pm 0.39 \pm 0.49$	$15.08 \pm 0.34 \pm 0.49$	$13.41^{+1.55}_{-1.78}$
1.11	$14.87 \pm 0.67 \pm 0.37$	$14.60 \pm 0.34 \pm 0.35$	$14.66 \pm 0.31 \pm 0.37$	$12.50^{+1.87}_{-1.73}$
1.30	$10.15 \pm 0.59 \pm 1.02$	$9.59 \pm 0.29 \pm 0.77$	$9.70 \pm 0.26 \pm 1.02$	$8.55^{+2.68}_{-2.38}$
1.48	$5.52 \pm 0.73 \pm 0.61$	$3.45 \pm 0.34 \pm 0.41$	$3.83 \pm 0.31 \pm 0.61$	$1.82^{+2.05}_{-2.37}$
1.66	$-6.77 \pm 1.30 \pm 0.82$	–	$-6.77 \pm 1.30 \pm 0.82$	$-10.06^{+2.45}_{-2.20}$
1.88	$-17.89 \pm 1.99 \pm 0.90$	–	$-17.89 \pm 1.99 \pm 0.90$	$-25.31^{+2.81}_{-2.24}$

Table 5.6: Combined CP folded asymmetry for $p_T > 35$ GeV and $\not\!\!E_T > 35$ GeV: the mean value of η ($< \eta >$), Run IIa asymmetry [$A^*_{\rm CP}$(Run IIa)], Run IIb asymmetry [$A^*_{\rm CP}$(Run IIb)], combined asymmetry [$A^*_{\rm CP}$], and symmetry with the CTEQ6.6 PDF sets [A(CTEQ6.6)]. All values have been multiplied by 100

$< \eta >$	$A^*_{\rm CP}$(Run IIa)	$A^*_{\rm CP}$(Run IIb)	$A^*_{\rm CP}$	A(CTEQ6.6)
0.10	$1.60 \pm 0.61 \pm 0.17$	$2.13 \pm 0.30 \pm 0.12$	$2.03 \pm 0.27 \pm 0.17$	$1.77^{+0.46}_{-0.53}$
0.30	$4.35 \pm 0.64 \pm 0.24$	$5.15 \pm 0.32 \pm 0.16$	$4.99 \pm 0.29 \pm 0.24$	$5.23^{+0.79}_{-0.74}$
0.50	$8.22 \pm 0.63 \pm 0.40$	$7.57 \pm 0.31 \pm 0.41$	$7.69 \pm 0.28 \pm 0.41$	$8.58^{+1.02}_{-1.11}$
0.71	$11.54 \pm 0.63 \pm 0.28$	$11.27 \pm 0.31 \pm 0.36$	$11.33 \pm 0.28 \pm 0.36$	$11.96^{+1.57}_{-1.58}$
0.89	$11.05 \pm 0.64 \pm 0.39$	$12.52 \pm 0.32 \pm 0.26$	$12.22 \pm 0.29 \pm 0.39$	$15.20^{+1.75}_{-1.85}$
1.11	$14.64 \pm 0.57 \pm 0.67$	$16.02 \pm 0.29 \pm 0.62$	$15.75 \pm 0.26 \pm 0.67$	$18.18^{+2.19}_{-2.00}$
1.30	$17.13 \pm 0.48 \pm 0.47$	$19.25 \pm 0.23 \pm 0.43$	$18.85 \pm 0.21 \pm 0.47$	$21.02^{+2.04}_{-2.20}$
1.49	$20.00 \pm 0.57 \pm 0.57$	$20.96 \pm 0.26 \pm 0.44$	$20.79 \pm 0.24 \pm 0.57$	$23.30^{+2.37}_{-2.17}$
1.66	$20.71 \pm 1.02 \pm 0.60$	–	$20.71 \pm 1.02 \pm 0.60$	$24.99^{+2.68}_{-2.90}$
1.88	$20.83 \pm 1.48 \pm 1.48$	–	$20.83 \pm 1.48 \pm 1.48$	$25.85^{+3.27}_{-3.11}$

Table 5.7: Summary of CP folded asymmetry results: the mean value of η ($< \eta >$), the asymmetries for $p_T > 25$ GeV and $\not\!\!E_T > 25$ GeV (bin 0), $25 < p_T < 35$ GeV and $\not\!\!E_T > 25$ GeV (bin 1), $p_T > 35$ GeV and $\not\!\!E_T > 25$ GeV (bin 2), $25 < p_T < 35$ GeV and $25 < \not\!\!E_T < 35$ GeV (bin 3), $p_T > 35$ GeV and $\not\!\!E_T > 35$ GeV (bin 4). All asymmetry values are multiplied by 100.

$< \eta >$	bin 0	bin 1	bin 2	bin 3	bin 4
0.10	2.1 ± 0.2	2.5 ± 0.3	1.8 ± 0.3	2.6 ± 0.5	2.0 ± 0.3
0.30	5.5 ± 0.2	6.1 ± 0.4	4.9 ± 0.3	5.9 ± 0.4	5.0 ± 0.4
0.50	9.1 ± 0.2	10.7 ± 0.4	7.8 ± 0.4	9.9 ± 0.6	7.7 ± 0.5
0.71	12.4 ± 0.3	14.0 ± 0.5	11.2 ± 0.3	12.9 ± 0.5	11.3 ± 0.5
0.89	14.1 ± 0.3	16.3 ± 0.5	12.6 ± 0.4	15.1 ± 0.6	12.2 ± 0.5
1.11	16.2 ± 0.3	16.7 ± 0.4	15.7 ± 0.4	14.7 ± 0.5	15.7 ± 0.7
1.30	16.5 ± 0.3	14.4 ± 0.5	17.9 ± 0.4	9.7 ± 1.1	18.9 ± 0.5
1.49	15.5 ± 0.3	10.2 ± 0.5	18.7 ± 0.4	3.8 ± 0.7	20.8 ± 0.6
1.66	11.1 ± 0.8	1.3 ± 1.2	17.4 ± 1.0	-6.8 ± 1.5	20.7 ± 1.2
1.88	7.6 ± 1.1	-7.2 ± 1.9	16.3 ± 1.6	-17.9 ± 2.2	20.8 ± 2.1

APPENDIX A

SINGLE MUON TRIGGERS

Tables A.2 and A.2 list all single muon triggers for Run IIa and Run IIb. The trigger names carry information about the requirements at the three muon trigger levels. Trigger names usually join level 1 and 2 terms to level 3 terms. The name conversions for the trigger levels are described below for Run IIa and Run IIb [69].

Level 1 and 2 names (in bold) and requirements:

MU_W_L2MX (X = 5, 0, 3)

Level 1: $\eta_{\rm det} < 1.6$, single muon trigger based on muon scintillator only.

Level 2: at least one muon found with $p_T >$ X (X = 0, 3, 5 GeV) meeting medium quality requirements.

MUW_W_L2M5

Level 1: $\eta_{\rm det} < 1.6$, single muon trigger with tight scintillator and loose wire requirements.

Level 2: at least one muon found with $p_T > 5$ GeV meeting medium quality requirements.

MUW_A_L2M3

Level 1: $\eta_{\rm det} < 2$, single muon trigger with tight scintillator and loose wire requirements.

Level 2: at least one muon found with $p_T > 3$ GeV meeting medium quality requirements.

MUH1

Level 1: $\eta_{\rm det} < 1.6$, single muon trigger based on tight scintillator and also requiring one track with $p_T > 10$ GeV.

Level 2: unrestricted trigger at Level 2

MUH2

Level 1: $\eta_{\rm det} < 2$, single muon trigger based on muon scintillator and wire chambers and a track with $p_T > 10$ GeV.

Table A.1: The single muon triggers for Run IIa.

Trigger name	Versions
$\lvert\eta_{\rm det}\rvert < 1.6$	
MU_W_L2M5_TRK10	8.00–10.03
MU_W_L2M0_TRK3	8.10–9.50
MU_W_L2M0_TRK10	9.30–9.50
MUW_W_L2M5_TRK10	10.00–10.03
MUW_W_L2M3_TRK10	10.30–12.37
MU_W_L2M3_TRK10	10.30–12.37
MUH1_TK12_TLM12	13.20–14.93
MUH1_TK12	13.10–13.11
MUH1_LM15	13.03–13.90
MUH1_TK10	13.03–13.62
MUH1_ILM15	14.00–14.93
MUH1_ITLM10	14.00–14.93
MUH4_LM15	13.03–13.11
MUH4_TK10	13.03–13.11
MUH6_TK12_TLM12	13.20–14.90
MUH6_LM15	13.03–14.90
MUH6_TK10	13.03–13.11
MUH7_TK10	13.03–13.11
MUH7_TK12	13.20–14.93
MUH7_LM15	13.03–14.90
MUH8_TK12_TLM12	14.60–14.93
MUH8_ILM15	14.60–14.93
MUH8_ITLM10	14.60–14.93
$\lvert\eta_{\rm det}\rvert < 2$	
MUW_A_L2M3_TRK10	10.30–11.04
MUH2_LM3_TK12	13.03–13.11
MUH2_LM6_TK12	13.20–13.23
MUH2_LM10_TK12	13.30–13.90
MUH2_LM15	13.03–13.23
MUH3_LM3_TK10	13.03–13.11
MUH3_LM6_TK12	13.20–13.23
MUH3_LM10_TK12	13.50–13.90
MUH3_LM15	13.03–13.23

Table A.2: The single muon triggers for Run IIb data.

Trigger name	Versions
$\lvert\eta_{\rm det}\rvert < 1.6$	
MUHI1_ITLM10	15.00–16.99
MUHI1_TK12_TLM12	15.00–16.99
MUHI1_ILM15	15.00–16.99
MUHI1_TLM12	16.00–16.99
MUHI1_ILM10	16.00–16.99
MUHI1_MM10	16.00–16.99
MUHI1_TMM10	16.00–16.99
MUHI2_ITLM10	15.00–16.99
MUHI2_TK12_TLM12	15.00–16.99
MUHI2_ILM15	15.00–16.99
MUHI2_ILM10	16.00–16.99
MUHI2_TLM12	16.00–16.99
MUHI2_MM10	16.00–16.99
MUHI2_TMM10	16.00–16.99
MUHI3_ITLM10	15.20–15.99
MUHI3_TK12_TLM12	15.20–15.96
MUHI3_ILM15	15.20–15.96
MUHI3_TMM10	16.50–16.99
MUHI3_MM10	16.50–16.99
MUHI3_ILM10	16.50–16.99
MUHI3_TLM12	16.50–16.99
MUHI4_TMM10	16.50–16.99
MUHI4_MM10	16.50–16.99
MUHI4_ILM10	16.50–16.99
MUHI4_TLM12	16.50–16.99
MUHI4_ITLM10	16.50–16.99
MUHI5_TMM10	16.50–16.99
MUHI5_MM10	16.50–16.99
MUHI5_ILM10	16.50–16.99
MUHI5_TLM12	16.50–16.99
MUHI5_ITLM10	16.50–16.99
MUHI6_TMM10	16.50–16.99
MUHI6_MM10	16.50–16.99
MUHI6_ILM10	16.50–16.99
MUHI6_TLM12	16.50–16.99
MUHI6_ITLM10	16.50–16.99

Level 2: at least one muon found with $p_T > 3$ GeV meeting medium quality requirements.

MUH3

Level 1: $\eta_{\rm det} < 2$, single muon trigger based on muon scintillator and one isolated CFT track with $p_T > 10$ GeV.

Level 2: at least one muon found meeting medium quality requirements but no p_T requirement.

MUH4

Level 1: $\eta_{\rm det} < 1.6$, single muon trigger with tight scintillator and tight wire requirements.

Level 2: at least one muon found with $p_T > 5$ GeV meeting medium quality requirements.

MUH6

Level 1: $\eta_{\rm det} < 1.6$, single muon trigger based on loose scintillator and loose wire requirements and also requiring one track with $p_T > 10$ GeV.

Level 2: unrestricted trigger at Level 2.

MUH7

Level 1: $\eta_{\rm det} < 1.6$, single muon trigger with tight scintillator and loose wire requirements.

Level 2: at least one muon found with $p_T > 5$ GeV meeting medium quality requirements.

MUH8

Level 1: $\eta_{\rm det} < 1.6$, single muon meeting tight scintillator and loose wire requirements. The muon must have $p_T > 10$ GeV and also requiring one track with $p_T > 10$ GeV.

Level 2: unrestricted trigger at Level 2.

MUHI1

Level 1: $\eta_{\rm det} < 1.6$, single muon trigger with tight scintillator and tight wire requirements matched to a CTT track with $p_T > 8$ GeV. In addition requires one isolated track with $p_T > 10$ GeV (the track is expected to be the track matched to the muon).

Level 2: one muon passing medium quality requirements and tight scintillator timing cuts and having $p_T > 3$ GeV, or one track found by the STT (good fit quality) and $p_T > 20$ GeV.

MUHI2

Level 1: $\eta_{\rm det} < 1.6$, single muon trigger with tight scintillator and tight wire requirements matched to a CTT track with $p_T > 8$ GeV. In addition requires one isolated track with

$p_T > 10$ GeV.

Level 2: one muon passing medium quality requirements and tight scintillator timing cuts and having $p_T > 3$ GeV, or one track found by the STT (good fit quality) and $p_T > 20$ GeV.

MUHI3

Level 1: $\eta_{\rm det} < 1.6$, single muon trigger with tight scintillator and tight wire requirements matched to a CTT track with $p_T > 13$ GeV.

Level 2: one muon passing medium quality requirements and tight scintillator timing cuts and having $p_T > 3$ GeV, or one track found by the STT (good fit quality) and $p_T > 20$ GeV.

MUHI4

Level 1: $\eta_{\rm det} < 1.6$, single muon trigger with tight scintillator and tight wire requirements matched to a CTT track with $p_T > 13$ GeV.

Level 2: one muon passing medium quality and tight scintillator cuts matched to an STT/CTT track of $p_T > 8$ GeV. Phi separation cut is $2\pi/80$.

MUHI5

Level 1: $\eta_{\rm det} < 1.6$, single muon trigger with tight scintillator and loose wire requirements matched to an isolated CTT track with $p_T > 13$ GeV.

Level 2: one muon passing medium quality and tight scintillator cuts matched to an STT/CTT track of $p_T > 8$ GeV. Phi separation cut is $2\pi/80$.

MUHI6

Level 1: $\eta_{\rm det} < 1.6$, single muon trigger with tight scintillator and tight wire requirements matched to a CTT track with $p_T > 13$ GeV. In addition requires one isolated track with $p_T > 10$ GeV.

Level 2: one muon passing medium quality and tight timing cuts matched to an STT/CTT track of $p_T > 20$ GeV, or one muon passing medium quality and tight timing cuts matched to an STT track of $p_T > 8$ GeV.

Level 3 names and requirements:

TRKX or TKX (X = 3, 10, 12): at least one track is found by the global tracker tool

with $p_T > 3$ (or 10, 12) GeV.

TK10H: at least one track found using histogram tracking with $p_T > 10$ GeV (with 10 hits).

LMX (X = 3, 6, 10): one loose muon with local $p_T > 3$ (or 6, 10) GeV.

TLM12: a loose central track matched local muon candidate with 12 GeV p_T threshold.

LM15: at least one muon is found with $p_T > 15$ GeV.

ILM15: at least one muon with $p_T > 15$ GeV and an isolated local loose muon candidate with 15 GeV p_T threshold (Isolation is determined with respect to calorimeter energy and other tracks).

ITLM10: a loose central track (found using SMT and CFT tracking) matched isolated local muon candidate with 10 GeV p_T threshold.

MM10: at least one medium local muon with $p_T > 10$ GeV.

TMM10: at least one medium local muon with $p_T > 10$ GeV matched a global track (found using SMT and CFT tracking) with a $p_T > 10$ GeV.

APPENDIX B

DATA-MC COMPARISION FOR $Z \to \mu\mu$ EVENTS

PYTHIA MC is not well matched to data in η and $W p_T$. To make sure that the disagreement is not due to mismeasured efficiencies, we compare data and MC for $Z \to \mu\mu$ events in Figure B.1. The data and MC match reasonably well in η_{det} and muon ϕ. Therefore, the disagreement for the $W \to \mu\nu$ events is primarily due to mismodeling of the W p_T in the MC samples.

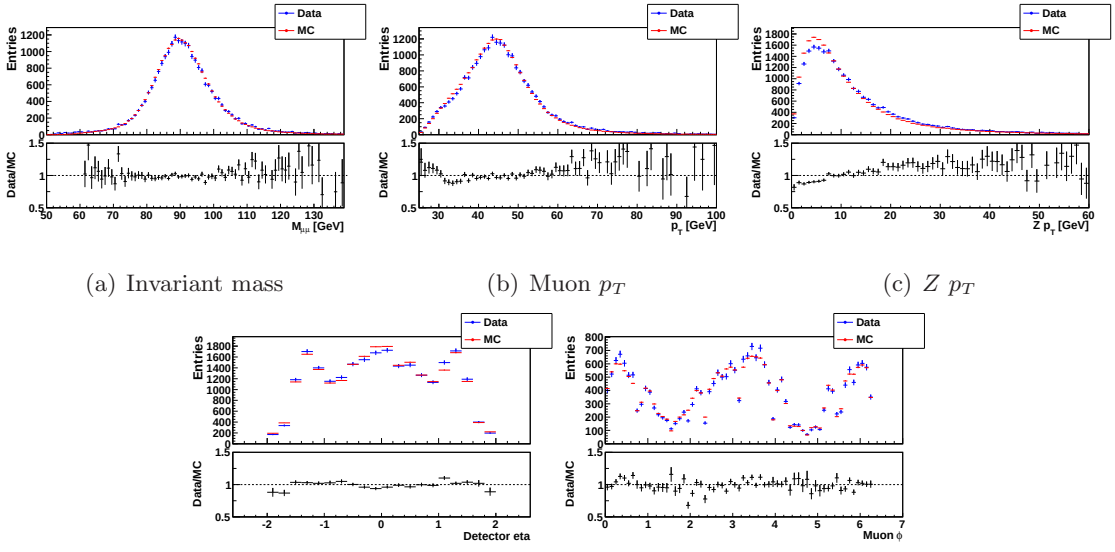

(a) Invariant mass (b) Muon p_T (c) Z p_T

(d) Muon η_{det} (e) Muon ϕ

Figure B.1: Data-MC comparison for $Z \to \mu\mu$ events.

APPENDIX C

ASYMMETRY SYSTEMATIC UNCERTAINTY CALCULATION

The systematic uncertainty on the muon charge asymmetry is the quadrature sum of the partial uncertainties from N_{EW}, N_{MJ}, g, and k. For the electroweak and multijet backgrounds, the systematic uncertainties dominate the statistical uncertainties. Therefore, the uncertainties due to the positive and negative signs of the backgrounds are mostly correlated and largely canceled out in the ratio A.

For the EW background, the variants of the $N^{\pm}_{\mathrm{EW}}$ can be expressed as $(1 \pm \Delta\alpha)N^{\pm}_{\mathrm{EW}}$, where $\Delta\alpha = \Delta N^{\pm}_{\mathrm{EW}}/N^{\pm}_{\mathrm{EW}}$. Eq. 4.13 could be written as

$$A = \frac{[(1-g+kg)(N^{+}_{\mathrm{data}} - N^{+}_{\mathrm{MJ}}) - (k-kg+g)(N^{-}_{\mathrm{data}} - N^{-}_{\mathrm{MJ}})] - \alpha[(1-g+kg)N^{+}_{\mathrm{EW}} - (k-kg+g)N^{-}_{\mathrm{EW}}]}{[(1-g-kg)(N^{+}_{\mathrm{data}} - N^{+}_{\mathrm{MJ}}) - (k-kg-g)(N^{-}_{\mathrm{data}} - N^{-}_{\mathrm{MJ}})] - \alpha[(1-g-kg)N^{+}_{\mathrm{EW}} - (k-kg-g)N^{-}_{\mathrm{EW}}]} \tag{C.1}$$

The partial derivative $\partial A/\partial\alpha$ is

$$\frac{\partial A}{\partial \alpha} = \frac{2k(1-2g)[(N^{+}_{\mathrm{data}} - N^{+}_{\mathrm{MJ}})N^{-}_{\mathrm{EW}} - (N^{-}_{\mathrm{data}} - N^{-}_{\mathrm{MJ}})N^{+}_{\mathrm{EW}}]}{[(1-g-kg)(N^{+}_{\mathrm{data}} - N^{+}_{\mathrm{EW}} - N^{+}_{\mathrm{MJ}}) + (k-kg-g)(N^{-}_{\mathrm{data}} - N^{-}_{\mathrm{EW}} - N^{-}_{\mathrm{MJ}})]^2} \tag{C.2}$$

Then the uncertainty on the asymmetry from the EW background is

$$\Delta A(N_{\mathrm{EW}}) = \Delta N_{\mathrm{EW}} \frac{2k(1-2g)[(N^{+}_{\mathrm{data}} - N^{+}_{\mathrm{MJ}})N^{-}_{\mathrm{EW}} - (N^{-}_{\mathrm{data}} - N^{-}_{\mathrm{MJ}})N^{+}_{\mathrm{EW}}]}{[(1-g-kg)(N^{+}_{\mathrm{data}} - N^{+}_{\mathrm{EW}} - N^{+}_{\mathrm{MJ}}) + (k-kg-g)(N^{-}_{\mathrm{data}} - N^{-}_{\mathrm{EW}} - N^{-}_{\mathrm{MJ}})]^2 N_{\mathrm{EW}}} \tag{C.3}$$

Similarly, the uncertainty on the asymmetry due to the multijet background could be obtained using the same method,

$$\Delta A(N_{\mathrm{MJ}}) = \Delta N_{\mathrm{MJ}} \frac{2k(1-2g)[(N^{+}_{\mathrm{data}} - N^{+}_{\mathrm{EW}})N^{-}_{\mathrm{MJ}} - (N^{-}_{\mathrm{data}} - N^{-}_{\mathrm{EW}})N^{+}_{\mathrm{MJ}}]}{[(1-g-kg)(N^{+}_{\mathrm{data}} - N^{+}_{\mathrm{EW}} - N^{+}_{\mathrm{MJ}}) + (k-kg-g)(N^{-}_{\mathrm{data}} - N^{-}_{\mathrm{EW}} - N^{-}_{\mathrm{MJ}})]^2 N_{\mathrm{MJ}}} \tag{C.4}$$

And the uncertainties on A from g and k, Eqs. (4.16, 4.17), are calculated from the partial derivative of A with respect to g and k.

APPENDIX D

W p_T REWEIGHTING

There is a disagreement between data and MC in W p_T. We learned that while the disagreement for W $p_T < 15$ GeV is primarily because of the MC mismodeling, the disagreement for W p_T about 20 GeV is due to the isolation requirements in the Level 1 and Level 3 trigger terms.

In this section, we check effects from the data-MC disagreement in W boson p_T by reweighting PYTHIA MC W p_T to data. The PYTHIA MC samples have all corrections applied as described in Section 4.5.1. Figure D.1 shows the MC W boson p_T before and after reweighting. The differences in the asymmetries are shown in Figure D.2. The change in the MC asymmetry from the reweighting is in blue. The discrepancy between the muon charge asymmetry results and the central values of the POWHEG CT10 prediction is in pink. The red line is the total uncertainty on the muon charge asymmetry. In all kinematic bins, the change from the reweighting is smaller than the disagreement between the experiment results and the theory prediction. Therefore, no action is taken to improve the MC simulation in W p_T.

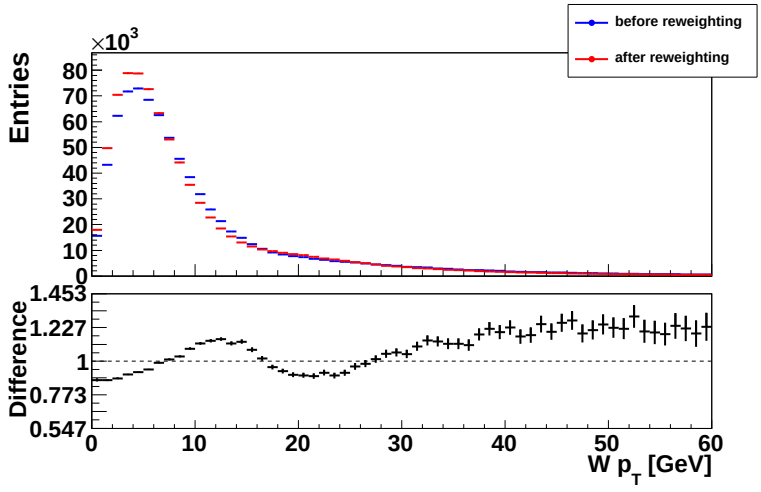

(a) $p_{T,\mu} > 25$ GeV, $\not{E}_T > 25$ GeV

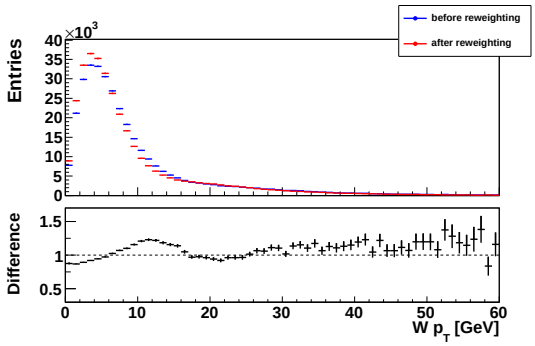

(b) $25 < p_{T,\mu} < 35$ GeV, $\not{E}_T > 25$ GeV

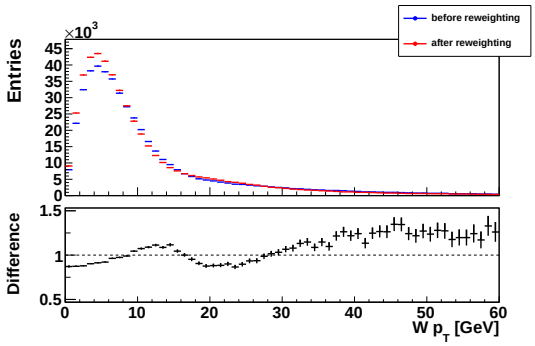

(c) $p_{T,\mu} > 35$ GeV, $\not{E}_T > 25$ GeV

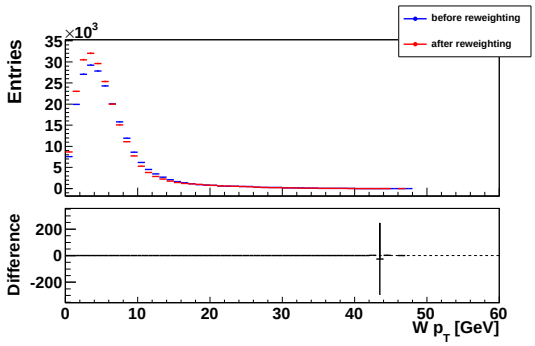

(d) $25 < p_{T,\mu} < 35$ GeV, $25 < \not{E}_T < 35$ GeV

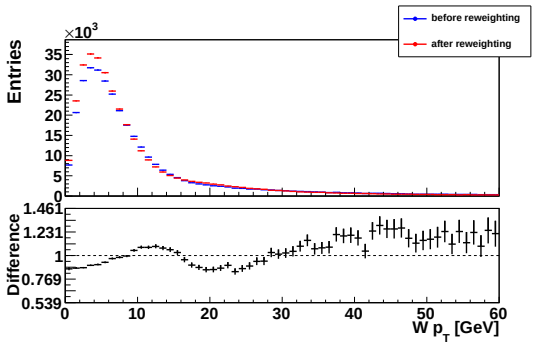

(e) $p_{T,\mu} > 35$ GeV, $\not{E}_T > 35$ GeV

Figure D.1: PYTHIA W boson p_T distributions before and after reweighting to data.

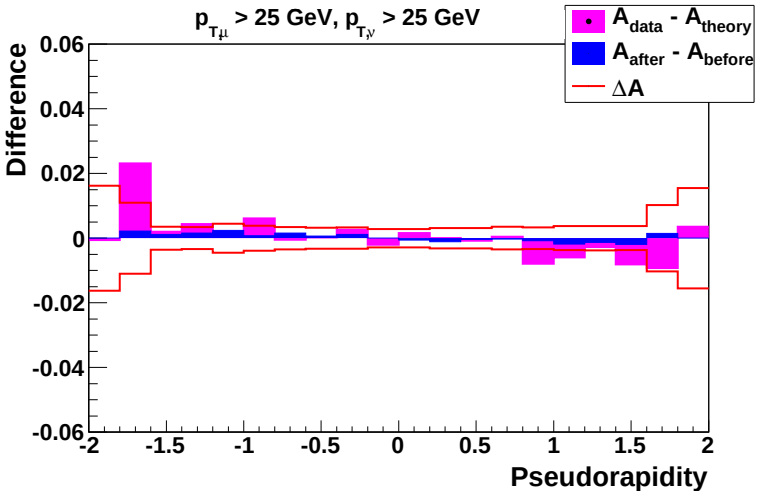

(a) $p_{T,\mu} > 25$ GeV, $\not{E}_T > 25$ GeV

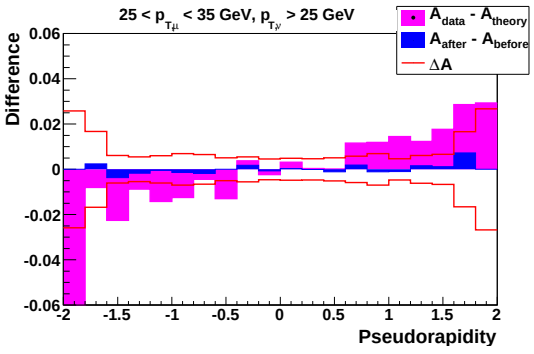

(b) $25 < p_{T,\mu} < 35$ GeV, $\not{E}_T > 25$ GeV

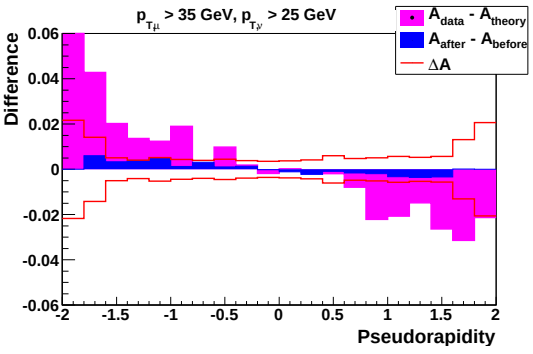

(c) $p_{T,\mu} > 35$ GeV, $\not{E}_T > 25$ GeV

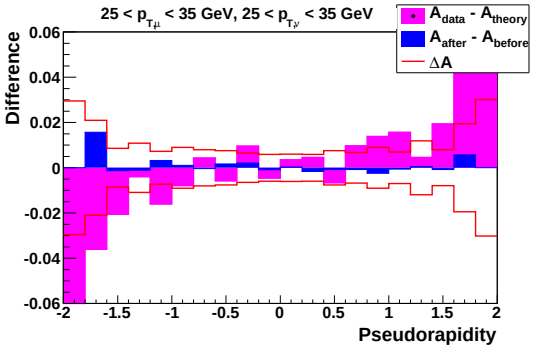

(d) $25 < p_{T,\mu}, 35$ GeV, $25 < \not{E}_T < 35$ GeV

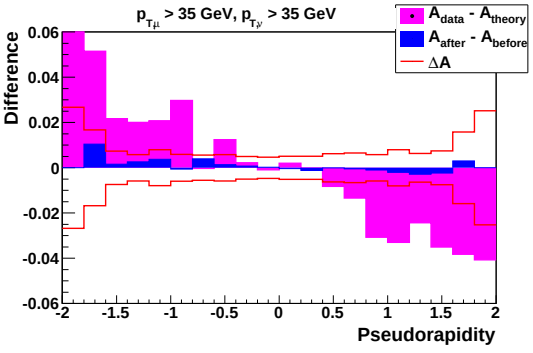

(e) $p_{T,\mu} > 35$ GeV, $\not{E}_T > 35$ GeV

Figure D.2: Difference between the PYTHIA asymmetries before and after reweighting (in blue). The pink region is the difference between the muon charge asymmetry and the central value of the POWHEG CT10 prediction. The red line is the total uncertainty on the muon charge asymmetry.

BIBLIOGRAPHY

[1] F. Abe *et al.* (CDF Collaboration), Phys. Rev. Lett. **74**, 2626 (1995).

[2] S. Abachi *et al.* (D0 Collaboration), Phys. Rev. Lett. **74**, 2632 (1995).

[3] F. Abe *et al.* (CDF Collaboration), Phys. Rev. Lett. **81**, 2432 (1998).

[4] K. Kodama *et al.* (DONUT Collaboration). Phys. Lett. B **504**, 218 (2001).

[5] V. M. Abazov *et al.* (D0 Collaboration), Phys. Rev. Lett. **103**, 092001 (2009).

[6] V. M. Abazov *et al.* (D0 Collaboration), Phys. Rev. Lett. **108**, 151804 (2012).

[7] Donald H. Perkins, "Introduction to High Energy Physics," Cambridge University Press, 4th edition (2000).

[8] Ringaile Placakyte, for the H1 and ZEUS Collaborations, "Parton Distribution Functions," arXiv:1111.5452 (2011).

[9] Hung-Liang Lai *et al.*, "New parton distributions for collider physics," arXiv:1007.2241 (2010).

[10] A. D. Martin, W. J. Stirling, R. S. Thorne, and G. Watt, Eur. Phys. J. C **63**, 189 (2009).

[11] P. M. Nadolsky *et al.*, Phys. Rev. D **78**, 013004 (2008).

[12] Richard D. Ball *et al.*, Nucl. Phys. B **809**, 1 (2009).

[13] F. Aaron *et al.* (H1 and ZEUS Collaborations), J. High Energy Phys. **01**, 109 (2010).

[14] S. Alekhin, J. Blümlein, S. Klein, and S. moch, Phys. Rev. D **81**, 014032 (2010).

[15] M. Glück, P. Jimenez-Delgado, and E. Reya, Eur. Phys. J. C **53**, 355 (2008).

[16] Sasha Glazov, for the H1 Collaboration, Braz. J. Phys. **37**, 2 (2007).

[17] V. D. Barger and R. J. N. Phillips, "Collider Physics," Addison Wesley, updated edition (1996).

[18] E. L. Berger, F. Halzen, C. S. Kim, and S. Willenbrock, Phys. Rev. D **40**, 83 (1989).

[19] R. K. Ellis, W. J. Stirling, and B. R. Webber, "QCD and Collider Physics," Cambridge University Press, 1st edition (1996).

[20] J. F. Owens *et al.*, "Global fits for PDFs," AIP Conf. Proc. **1369**, 13 (2011).

[21] F. Abe *et al.* (CDF Collaboration), Phys. Rev. Lett. **74**, 850 (1995).

[22] F. Abe *et al.* (CDF Collaboration), Phys. Rev. Lett. **81**, 5754 (1998).

[23] D. Acosta *et al.* (CDF Collaboration), Phys. Rev. D **71**, 051104 (2005).

[24] V. M. Abazov *et al.* (D0 Collaboration), Phys. Rev. D **77**, 011106 (2008).

[25] V. M. Abazov *et al.* (D0 Collaboration), Phys. Rev. Lett. **101**, 211801 (2008).

[26] T. Aaltonen *et al.* (CDF Collaboration), Phys. Rev. Lett. **102**, 181801 (2009).

[27] G. Aad *et al.* (ATLAS Collaboration), Phys. Lett. B **701**, 31 (2011).

[28] S. Chatrchyan *et al.* (CMS Collaboration), J. High Energy Phys. **04**, 050 (2011).

[29] J. Thompson, "Introduction to Colliding Beams at Fermilab," FERMILAB-TM-1909, (1994).

[30] Fermilab Beam Division, "Fermilab's Chain of Accelerators," `http://www-bd.fnal.gov/public/chain.html`.

[31] V. M. Abazov *et al.* (DØ Collaboration), "The upgraded DØ detector," Nucl. Instrum. Methods Phys. Res. A **565**, 463 (2006).

[32] V. M. Abazov *et al.* (DØ Collaboration), "The muon system of the Run II DØ detector," Nucl. Instrum. Methods Phys. Res. A **552**, 372 (2005).

[33] DØ algorithm group, "How to run RECO," `http://www-d0.fnal.gov/computing/algorithms/howto/howtoreco.html`.

[34] G. Borissov, "Ordering a Chaos or ... Technical Detail of AA Tracking", `http://www-d0.fnal.gov/global_tracking/talks/20030228/talk-adm-030228.ps`.

[35] A. Khanov, "HTF: histograming method for finding tracks. The algorithm description," DØ Note 3778.

[36] Hough, P.V.C., "Machine Analysis of Bubble Chamber Pictures, Proc. Int. Conf. High Energy Accelerators and Instrumentation (1959).

[37] H. Greenlee, "The D0 Kalman Track Fit," DØ Note 4303.

[38] A. Schartman and M. Narain, "Primary Vertex Selection," DØ Note 3906.

[39] O. Peters, "Muon Segment Reconstruction: A Linked List Algorithm," DØ Note 3901.

[40] P. Calfayan *et al.*, "Muon Identification Certification for p17 Data," DØ Note 5157.

[41] Oleg Brandt *et al.*, "Muon Identification Certification for the Summer 2009 Extended Data Set (Run IIb-1 and -2)," DØ Note 6025.

[42] E. Busato and B. Andrieu, "Jet Algorithms in the DØ RunII Software: Description and User's Guide," DØ Note 4457.

[43] Dmitry Bandurin *et al.*, "Jet energy scale determination for DØ Run IIb," DØ Note 6327.

[44] Julie M. Hogan, "Missing E_T and Primary Vertex Position in Different Run Periods," DØ Note 6242.

[45] Ken Herner, "Well MET: Understanding Missing ET at D0," `http://www-d0.hef.ru.nl//askArchive.php?base=agenda&categ=a111734&id=a111734s1t1/transparencies`.

[46] T. Sjostrand *et al.*, "Pythia 6.4 physics and manual," J. High Energy Phys. **05**, 026 (2006).

[47] S. Agostinelli *et al.*, Nucl. Inst. Meth. in Phys. Res. A **506**, (2003).

[48] Yuri Fisyak and John Womersley, "DØ GEANT simulation of the Total Apparatus Response," DØ Note 3191.

[49] MC simulation group, "D0SIM User Manual," DØ Note 407.

[50] C. Balazs and C.P. Yuan, Phys. Rev. D **56**, 5558 (1997).

[51] E. Barberio and Z. Was, Cumput. Phys. Commun. **79**, 291 (1994). We use PHOTOS version 2.0.

[52] D. Stump *et al.*, J. High Energy Phys. **10**, 046 (2003).

[53] M.R. Whalley *et al.*, hep-ph/0508110.

[54] S. Alioli *et al.*,"NLO vector-boson production matched with shower in POWHEG," J. High Energy Phys. **0807**, 060 (2008).

[55] Richard D. Ball *et al.*, arXiv:1012.0836v3.

[56] S. Sengupta, "The W boson production charge asymmetry in the muon channel at $\sqrt{s} = 1.96$ TeV," Ph.D. dissertation (2006).

[57] V. M. Abazov *et al.* (DØ Collaboration), Phys. Rev. Lett. **103**, 141801 (2009).

[58] Philippe Calfayan, "Combination of Single Muon Triggers in p17 data by using an inclusive OR," DØ Note 5329.

[59] A. Harel, "Jet ID optimization," DØ Note 4919.

[60] Frabrice Couderc *et al.*, "MC normalization with common tools," `http://www-d0.hef.kun.nl//askArchive.php?base=agenda&categ=a091522&id=a091522s6t4/transparencies`.

[61] T. Nunnemannn, "NNLO normalization for inclusive Z , W and Drell-Yan MC samples," http://www-d0.hef.ru.nl//askArchive.php?base=agenda&categ=a11118&id=a11118s1t15/transparencies.

[62] W. Verkerke and D. Kirkby, RooFit Users Manual v2.91, ftp://root.cern.ch/root/doc/RooFit_Users_Manual_2.91-33.pdf.

[63] F. James and M. Roos (CERN), Comput. Phys. Commun. **10**, 343 (1975).

[64] T. Andeen *et al.*, "The DØ Experiment's Integrated Luminosity for Tevatron Run IIa," DØ Note 5398.

[65] M. Arthaud *et al.*, "Muon Momentum Oversmearing for p17 Data," DØ Note 5444.

[66] M. Arthaud *et al.*, "Muon Momentum Oversmearing for p20 Data," DØ Note 5449.

[67] O. Brandt *et al.*, "Muon Momentum Oversmearing Update for Run IIa, Run IIb2 and Run IIb3 Data Taking Epochs and Monte Carlo p17 and p20," DØ Note 6190.

[68] A. Askew, S. Blessing, and T. Hoang, "Measurement of the muon charge asymmetry in $p\overline{p} \rightarrow W + X \rightarrow \mu\nu + X$ events using the DØ detector," DØ Note 6239.

[69] Trigger group, "Global Trigger Lists Description," http://www-d0.fnal.gov/trigger_meister/private/www/tl_desc/global.html.

BIOGRAPHICAL SKETCH

Trang T. Hoang was born in Ho Chi Minh City, Vietnam. In 1998, she finished her Bachelors degree in Physics at the Natural Science University. In 2001, she spent five months at Fermi National Accelerator Laboratory (Fermilab) as a visitor, when she became interested in high energy physics and wanted to pursue higher education in the field.

In 2002, Trang received her Masters degree in Nuclear Physics at the Natural Science University. In 2004, she won a scholarship of the MEXT nuclear researcher exchanging program and spent six months at the Tokai Research Establishment, in Japan, studying nuclear structure with gamma-ray spectroscopy. During the program, she gained more experiences in working with experimental instruments and learned the C++ programming language.

In 2005, Trang moved to Tallahassee to start her Ph.D. program in physics at the Florida State University. In 2006, she joined the High Energy Physics group and moved to Batavia, Illinois to do her research in experimental high energy physics at the Fermilab Tevatron Collider. Under the direction of Prof. Susan Blessing, she wrote her dissertation "Measurement of the muon charge asymmetry in $p\overline{p} \rightarrow W + X \rightarrow \mu\nu + X$ events using the DØ detector." In addition, she served as a calorimeter expert to help maintain the DØ calorimeter.

In Fall 2012, Trang successfully defended her dissertation. She is currently preparing a publication on the muon charge asymmetry. She plans to continue her research in particle physics at the Large Hadron Collider.